RADIANCE IN THE OCEAN: EFFECTS OF WAVE SLOPE AND RAMAN SCATTERING NEAR THE SURFACE AND AT DEPTHS THROUGH THE ASYMPTOTIC REGION

A Thesis

by

JULIE MARIE SLANKER

Submitted to the Office of Graduate Studies of
Texas A&M University
in partial fulfillment of the requirements for the degree of

MASTER OF SCIENCE

December 2007

Major Subject: Physics

RADIANCE IN THE OCEAN: EFFECTS OF WAVE SLOPE AND RAMAN SCATTERING NEAR THE SURFACE AND AT DEPTHS THROUGH THE ASYMPTOTIC REGION

A Thesis

by

JULIE MARIE SLANKER

Submitted to the Office of Graduate Studies of
Texas A&M University
in partial fulfillment of the requirements for the degree of

MASTER OF SCIENCE

Approved by:

Chair of Committee,	George W. Kattawar
Committee Members,	Wayne M. Saslow
	Ping Yang
Head of Department,	Edward S. Fry

December 2007

Major Subject: Physics

ABSTRACT

Radiance in the Ocean: Effects of Wave Slope and Raman Scattering Near the Surface and at Depths through the Asymptotic Region. (December 2007)

Julie Marie Slanker, B.S.; B.S., Florida Institute of Technology

Chair of Advisory Committee: Dr. George Kattawar

Three investigations were conducted on the nature of the radiance field in clear ocean water. It is important to understand the sunlight intensity below the sea surface because this leads to an understanding of how ocean creatures navigate in shallow and deep water. The nature of the radiance field is also gives an understanding of the living environment for ocean animals. Hydrolight 4.1, a simulation software developed by Curtis D. Mobley, was used to calculate the spectral radiance in clear ocean water for multiple wavelengths from the surface down through the asymptotic region. The first study found, as expected, that Raman scattering has little effect on wavelengths of light that are less than 500 nm. The effect of Raman scattering increases with increasing wavelength, and with increasing depth. The second study found the region of the water column where the radiance field is asymptotic. The third investigation found the effect of changing the mean square slope, or variance of the water-wave slope distribution. This effect is greatest near the surface and for a more truncated mean square slope integral. There are three peaks in percent difference to the ideal case, near the surface, one in the solar beam and the others near the critical angle of water.

To the Slankers:

Mom,

Dad,

David,

Jeff,

Susie,

Nicki,

Jaxson, and

Grant

And, to Josh

(of course)

ACKNOWLEDGEMENTS

I would like to thank Dr. Kattawar for allowing me to join his research group, and helping me to complete this degree so quickly. I would not have been able to achieve my goals so easily without his guidance.

TABLE OF CONTENTS

		Page
ABSTRACT		iii
DEDICATION		iv
ACKNOWLEDGEMENTS		v
TABLE OF CONTENTS		vi
LIST OF FIGURES		viii
LIST OF TABLES		xiv
CHAPTER		
I	INTRODUCTION: THE IMPORTANCE OF AN ACCURATE WATER MODEL	1
II	THE HYDROLIGHT 4.1 MODELS	2
	2.1 Introduction	2
	2.2 ABCONST	2
	2.3 ABCASE1	3
	2.4 Principal Plane	4
III	THE EFFECT OF RAMAN SCATTERING	6
	3.1 Introduction	6
	3.2 Simulation Results	9
	3.3 Conclusions	15
IV	THE ASYMPTOTIC REGION	16
	4.1 Introduction	16
	4.2 One Component, Homogeneous Water Model	16
	4.3 Historical Case 1 Water Model	21
	4.4 Conclusions	26
V	THE EFFECT OF CHANGING THE MEAN SQUARE SLOPE	27
	5.1 Introduction	27
	5.2 One Component, Homogeneous Water Model	29

CHAPTER Page

5.3 Historical Case 1 Water Model ……..... 37
5.4 Conclusions …… 69

VI CONCLUSIONS ……... 70

REFERENCES …….. 72

VITA ……. 74

LIST OF FIGURES

FIGURE		Page
1	Diagram of solar and detector positions in the Principal Plane ...	4
2	Raman wavelength redistribution function for select incident wavelengths …….	7
3	Logarithmic absorption coefficient versus wavelength for clear ocean waters…….	8
4	Logarithmic radiance versus polar angle for 460 nm light when Raman scattering is not included……..	9
5	Logarithmic radiance versus polar angle for 460 nm light when Raman scattering is included ……	10
6	Logarithmic radiance versus polar angle for 500 nm light when Raman scattering is not included …….	11
7	Logarithmic radiance versus polar angle for 500 nm light when Raman scattering is included ……...	11
8	Logarithmic radiance versus polar angle for 540 nm light when Raman scattering is not included …….	12
9	Logarithmic radiance versus polar angle for 540 nm light when Raman scattering is included ……...	13
10	Logarithmic radiance versus polar angle for 580 nm light when Raman scattering is not included ……	14
11	Logarithmic radiance versus polar angle for 580 nm light when Raman scattering is included ……..	14
12	Logarithmic radiance versus polar angle for single scattering Albedo, $\omega_o = 0.5$, extinction coefficient 0.032 m^{-1} …….	17
13	Logarithmic radiance versus polar angle for single scattering Albedo, $\omega_o = 0.25$, extinction coefficient 0.032 m^{-1} …….	18
14	Logarithmic radiance versus polar angle for single scattering Albedo, $\omega_o = 0.75$, extinction coefficient 0.032 m^{-1} …….	19
15	Logarithmic radiance versus polar angle for single scattering Albedo, $\omega_o = 0.90$, extinction coefficient 0.032 m^{-1} …….	21

FIGURE Page

16 Logarithmic radiance versus polar angle for 460 nm light when Raman scattering is included, expanded radiance scale…… 23

17 Logarithmic radiance versus polar angle for 520 nm light when Raman scattering is included …… 24

18 Logarithmic radiance versus polar angle for 580 nm light when Raman scattering is included, expanded radiance scale…… 25

19 Logarithmic radiance versus polar angle for one component water at multiple k_{max} values, just above the surface ……. 30

20 Percent difference versus polar angle for one component water, just above the surface …… 30

21 Logarithmic radiance versus polar angle for one component water at multiple k_{max} values, just below the surface ……. 31

22 Percent difference versus polar angle for one component water, just below sea the surface ...…… 32

23 Logarithmic radiance versus polar angle for one component water at multiple k_{max} values, at optical depth $\tau = 1$ …….. 33

24 Percent difference versus polar angle for one component water, at optical depth $\tau = 1$ ……. 33

25 Logarithmic radiance versus polar angle for one component water at multiple k_{max} values, at optical depth $\tau = 2$ …….. 34

26 Percent difference versus polar angle for one component water, at optical depth $\tau = 2$ ……. 35

27 Logarithmic radiance versus polar angle for one component water at multiple k_{max} values, at optical depth $\tau = 5$ …….. 35

28 Percent difference versus polar angle for one component water, at optical depth $\tau = 5$ ……. 36

29 Logarithmic radiance versus polar angle for one component water at multiple k_{max} values, at optical depth $\tau = 10$ …… 36

30 Percent difference versus polar angle for one component water, at optical depth $\tau = 10$ ……... 37

31 Logarithmic radiance versus polar angle for 460 nm light at multiple k_{max} values, geometric depth z = 0 m …….. 38

32 Percent difference versus polar angle for 460 nm light detectors at geometric depth z = 0 m …… 39

FIGURE Page

33 Logarithmic radiance versus polar angle for 460 nm light at multiple k_{max} values, geometric depth z = 10 m …… 39

34 Percent difference versus polar angle for 460 nm light detectors at geometric depth z = 10 m ……. 40

35 Logarithmic radiance versus polar angle for 460 nm light at multiple k_{max} values, geometric depth z = 30 m ……. 40

36 Percent difference versus polar angle for 460 nm light detectors at geometric depth z = 30 m …….. 41

37 Logarithmic radiance versus polar angle for 460 nm light at multiple k_{max} values, geometric depth z = 50 m ……. 41

38 Percent difference versus polar angle for 460 nm light detectors at geometric depth z = 50 m ...……. 42

39 Logarithmic radiance versus polar angle for 460 nm light at multiple k_{max} values, geometric depth z = 100 m …….. 43

40 Percent difference versus polar angle for 460 nm light detectors at geometric depth z = 100 m ……..……... 43

41 Logarithmic radiance versus polar angle for 460 nm light at multiple k_{max} values, geometric depth z = 400 m …….. 44

42 Percent difference versus polar angle for 460 nm light detectors at geometric depth z = 400 m ……..……... 44

43 Logarithmic radiance versus polar angle for 460 nm light at multiple k_{max} values, geometric depth z = 700 m …….. 45

44 Percent difference versus polar angle for 460 nm light at geometric depth z = 700 m ……... 45

45 Logarithmic radiance versus polar angle for 460 nm light at multiple k_{max} values, geometric depth z = 800 m …….. 46

46 Percent difference versus polar angle for 460 nm light detectors at geometric depth z = 800 m ……... 47

47 Logarithmic radiance versus polar angle for 460 nm light at multiple k_{max} values, geometric depth z = 900 m …….. 47

48 Percent difference versus polar angle for 460 nm light detectors at geometric depth z = 900 m ……..……... 48

FIGURE Page

49 Logarithmic radiance versus polar angle for 520 nm light at multiple k_{max} values, geometric depth z = 0 m …….. 49

50 Percent difference versus polar angle for 520 nm light detectors at geometric depth z = 0 m ……..... 49

51 Logarithmic radiance versus polar angle for 520 nm light at multiple k_{max} values, geometric depth z = 10 m …… 50

52 Percent difference versus polar angle for 520 nm light detectors at geometric depth z = 10 m ……..... 50

53 Logarithmic radiance versus polar angle for 520 nm light at multiple k_{max} values, geometric depth z = 30 m …… 51

54 Percent difference versus polar angle for 520 nm light at geometric depth z = 30 m ……..... 51

55 Logarithmic radiance versus polar angle for 520 nm light at multiple k_{max} values, geometric depth z = 50 m …… 52

56 Percent difference versus polar angle for 520 nm light detectors at geometric depth z = 50 m ……..... 52

57 Logarithmic radiance versus polar angle for 520 nm light at multiple k_{max} values, geometric depth z = 100 m …….. 53

58 Percent difference versus polar angle for 520 nm light detectors at geometric depth z = 100 m ……... 54

59 Logarithmic radiance versus polar angle for 520 nm light at multiple k_{max} values, geometric depth z = 300 m …….. 54

60 Percent difference versus polar angle for 520 nm light detectors at geometric depth z = 300 m ……... 55

61 Logarithmic radiance versus polar angle for 520 nm light at multiple k_{max} values, geometric depth z = 500 m …….. 56

62 Percent difference versus polar angle for 520 nm light detectors at geometric depth z = 500 m ……... 56

63 Logarithmic radiance versus polar angle for 520 nm light at multiple k_{max} values, geometric depth z = 700 m …….. 57

64 Percent difference versus polar angle for 520 nm light detectors at geometric depth z = 700 m ……... 57

FIGURE Page

65 Logarithmic radiance versus polar angle for 520 nm light at multiple k_{max} values, geometric depth z = 900 m …….. 58

66 Percent difference versus polar angle for 520 nm light at geometric depth z = 900 m ……... 59

67 Logarithmic radiance versus polar angle for 580 nm light at multiple k_{max} values, geometric depth z = 0 m …….. 60

68 Percent difference versus polar angle for 580 nm light detectors at geometric depth z = 0 m ……..……..... 60

69 Logarithmic radiance versus polar angle for 580 nm light at multiple k_{max} values, geometric depth z = 10 m …… 61

70 Percent difference versus polar angle for 580 nm light detectors at geometric depth z = 10 m ..……..... 61

71 Logarithmic radiance versus polar angle for 580 nm light at multiple k_{max} values, geometric depth z = 30 m …… 62

72 Percent difference versus polar angle for 580 nm light detectors at geometric depth z = 30 m …..……..... 62

73 Logarithmic radiance versus polar angle for 580 nm light at multiple k_{max} values, geometric depth z = 50 m …… 63

74 Percent difference versus polar angle for 580 nm light detectors at geometric depth z = 50 m …..……..... 63

75 Logarithmic radiance versus polar angle for 580 nm light at multiple k_{max} values, geometric depth z = 100 m …….. 64

76 Percent difference versus polar angle for 580 nm light detectors at geometric depth z = 100 m ……..……... 65

77 Logarithmic radiance versus polar angle for 580 nm light at multiple k_{max} values, geometric depth z = 300 m …….. 65

78 Percent difference versus polar angle for 580 nm light detectors at geometric depth z = 300 m ……..……... 66

79 Logarithmic radiance versus polar angle for 580 nm light at multiple k_{max} values, geometric depth z = 500 m …….. 67

80 Percent difference versus polar angle for 580 nm light detectors at geometric depth z = 500 m …..……... 67

FIGURE Page

81 Logarithmic radiance versus polar angle for 580 nm light at multiple k_{max} values, geometric depth z = 700 m …….. 68

82 Percent difference versus polar angle for 580 nm light detectors at geometric depth z = 700 m ……..... 69

LIST OF TABLES

TABLE		Page
1	Integrated mean square slope for wind speed 5 m/s up to the maximum wave number corresponding to each cut-off wavelength ……	28
2	Corresponding wind speed to each integrated mean square slope ……..	28

CHAPTER I
INTRODUCTION: THE IMPORTANCE OF AN ACCURATE WATER MODEL

In order to fully understand how ocean dwelling creatures navigate their environment, one must have a clear picture of the radiance field below the sea surface. As depth increases, there is a sharp decrease in scalar radiance, which is the sunlight intensity. So, scalar radiance is only useful to under sea organisms in shallow water. The animals are able to accurately detect the location of the sun, by the location of a strong peak in radiance, and use this information for navigation; this process is called photomenotaxis.[1] However, with increasing depth the peak begins to migrate toward the zenith, and information is lost. At further depth, the radiance field enters the asymptotic regime, defined as the range of depths over which the radiance field is independent of the sun's location, is vertically symmetric, and decays at a constant rate for all angles.[2] In this region, only phototaxis is available for navigation, i.e. toward or away from the surface.[1] Once the peak in radiance begins to shift, the animals must use alternate methods to find their way in the sea.

The radiance field below the sea surface can be modeled accurately using simulation software, such as Hydrolight 4.1. Some of the functions used in these applications can not be solved exactly, and must be truncated in a way that does not compromise the end result. In this investigation, the main objective is to measure the effect of changing the mean square slope on the radiance field simulated by the Hydrolight 4.1 software. Multiple wavelengths will be studied, where Raman scattering is negligible and also where it is important, and the effect will be measured throughout the entire water column, from the surface down through the asymptotic region.

This thesis follows the style of Applied Optics.

CHAPTER II
THE HYDROLIGHT 4.1 MODELS

2.1 Introduction

Hydrolight 4.1 is a simulation software, developed by Curtis D. Mobley, which calculates the underwater spectral radiance field from a set of inherent optical properties input by the user. The program solves the radiative transfer equation numerically by averaging over direction and wavelength. The set of all directions is defined by polar angle, θ, where $0 \le \theta < 180$ degrees, and azimuthal angle, ϕ, where $0 \le \phi < 360$ degrees. The Hydrolight model averages the radiance field into regions, called quads. Each quad has an equal "width" defined by a range of azimuthal angles and "height" defined by a range of polar angles. There are also two circular polar caps.[3] The default settings for Hydrolight 4.1 use a quad layout of 20 μ by 24 ϕ, where $\mu = \cos\theta$. In this study, the simulations were run with layouts of either 40 μ by 24 ϕ or 180 μ by 24 ϕ.

The Hydrolight 4.1 model provides the user with multiple routines which may be used to specify the inherent optical properties required for a given simulation. In this study, only two of the routines were used; namely, one where the absorption and scattering coefficients are independent of depth, the other where the absorption and scattering coefficients are taken from a historical Case 1 water model.

2.2 ABCONST

The first water model used was a one component, single wavelength, homogeneous water column. The total absorption coefficient, a, and total scattering coefficient, b, were both independent of depth. The total extinction coefficient was 0.032 m^{-1}. The Scattering Phase Function was Petzold Average Particle and the Wavelength used was 530 nm.

The other specified values, organized by input window, are given as follows:

The wind speed was entered in m/s with the last significant digit in the hundredths place, and then the values were updated in the boxes defining other systems of units. We used a semi-empirical sky model, which is based on RADTRAN. The cloud cover was always zero, giving a totally clear sky.

The atmospheric parameters that went along with the RADTRAN model were:
Sea-level pressure: 29.92 inches HG
24-hr Averaged Windspeed: our previous input
Average horizontal visibility: 15 km
Relative humidity: 80 %
Precipitable water content: 2.5 cm
Total Ozone: -99 Dobson units
Airmass type: 1 (to denote marine rather than continental)

The downwelling sky IRRADIANCE was specified by RADTRAN, which gave the direct (solar) and diffuse (sky) components of the irradiance. Both were calculated directly from the RADTRAN model. The ANGULAR PATTERN of the sky radiance distribution was obtained from a subroutine, in the maincode directory, named hcnrad.

An infinitely deep water column was used to avoid any interfering radiance reflected up from the bottom, and we took data at specific optical depths. By default, Hydrolight places a detector just above the ocean surface, to define the input, and just below the ocean surface.

2.3 ABCASE1

The second water model had two components specified in the inherent optical properties. The first component was pure water; the second was chlorophyll bearing particles. The absorption for component one was taken from Smith and Baker's[4] "clearest natural waters". The chlorophyll concentration used was 0.05 mg m^{-3} and the scattering phase function was the Petzold Average Particle. This two component model, allowed for multiple wavelengths to be calculated as part of a single data run, so it was possible to include Raman scattering, along with other inelastic scattering. The wavelengths used were 20 nm bands from 370 nm to 670 nm. The output specified the average radiance values, over the 20 nm width, at the median wavelength for each band. As with the first water model, wind speed and output depths had to be chosen by the user. However,

because this model uses multiple wavelengths, the output could only be generated for specific geometric depths, as opposed to the optical depths allowed by the first model. Again, an infinite water column was used to avoid reflection off of the sea floor.

2.4 Principal Plane

The Hydrolight 4.1 output gives a spectral radiance value for each of the predetermined quads, covering all possible directions. However, for the purposes of this study, it was only necessary to use the radiance calculated for the principal plane. The principal plane is defined by two vectors, one pointing toward the zenith, the other pointing toward the location of the sun. As shown below in Figure 1, azimuth angle $\phi = 0$ degrees points in the direction of the sun, and therefore this half-plane, along with the half-plane located at $\phi = 180$ degrees, make up the principal plane.

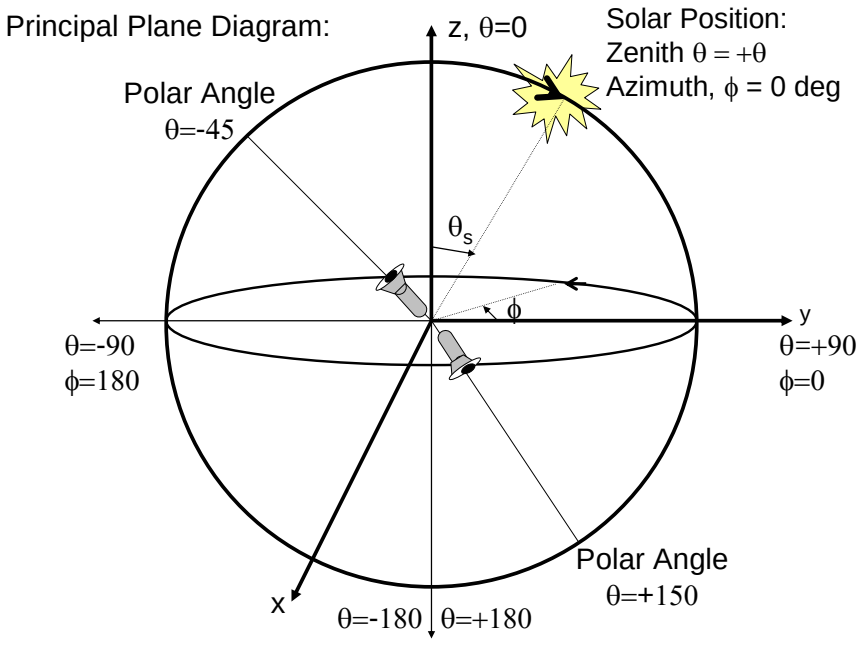

Figure 1 Diagram of solar and detector positions in the Principal Plane. The polar angles defined in this diagram were used to generate all of the graphs presented here.

In the figures presented in this study, the sign of the polar angle, θ, is used to define the two halves of the principal plane. Positive polar angles, $0 \le \theta < 180$, correspond to the

$\phi = 0$ half-plane, and negative polar angles, $-180 \leq \theta < 0$, correspond to the $\phi = 180$ half-plane, with the polar angle itself describing the direction the *simulated detector is pointing*.

CHAPTER III
THE EFFECT OF RAMAN SCATTERING

3.1 Introduction

In *Light and Water*, Curtis D. Mobley lays out a simplified explanation of Raman scattering.[5] This type of scattering is an inelastic process that occurs when an incident photon interacts with the electron cloud of a molecule. For this investigation, the molecule was water. Each molecule's electron cloud oscillates at an inherent vibrational frequency and each photon can be described as an electromagnetic wave with an oscillating electric field of a certain frequency. When the two interact, the electron cloud will begin to oscillate at the photon's frequency, in addition to its own inherent frequency. Elastic scattering occurs when the molecule reradiates a photon with the same energy as the incident photon. Raman scattering, on the other hand, occurs when the molecule reradiates at a frequency equal to either the sum or difference of the incident photon frequency and the inherent vibrational frequency of the molecule. Liquid water exists at a relatively low temperature, so it is unlikely for the emitted photon to have a higher frequency than the incident photon. Thus, it is valid to say that Raman scattering in water shifts the energy of an incident photon from higher to lower frequency, shorter to longer wavelengths. The residual energy, left with the molecule, usually takes the form of heat in such a small amount that it is imperceptible.

Figure 2 shows the wavelength redistribution due to Raman scattering for select incident wavelengths. The relative strength of Raman scattering can be taken from the total differential cross section. For incident wavelength λ = 488 nm, the total differential cross section of Raman scattering is[6] $(8.2 \pm 1) \times 10^{-30}$ cm^2 molicule^{-1} sr^{-1}. This value can be used to calculate the volume scattering coefficient for Raman scattering, b_r. In water[6] $b_r = 2.6 \times 10^{-4}$ m^{-1}. The volume scattering coefficient of pure salt water, at wavelength λ = 490 nm, is known to be[4] $b^{sw} = 3.1 \times 10^{-3}$ m^{-1}. Comparing the two

scattering coefficients, it shows that on average Raman scattering occurs in one out of every ten photon scatterings by water molecules.[5]

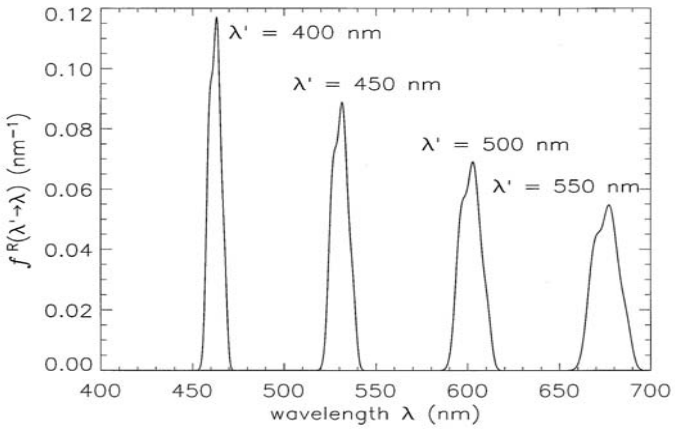

Figure 2 Raman wavelength redistribution function for select incident wavelengths[5]

When photons interact with water molecules, the incident photon's energy can also be fully absorbed. Some wavelengths of light are more likely to be absorbed by the water molecules than others, specifically wavelengths greater than 550 nm.[5] Figure 3 shows the absorption coefficient of water, a_w, taken from the experimental results of Smith and Baker[4] and Pope and Fry.[7]

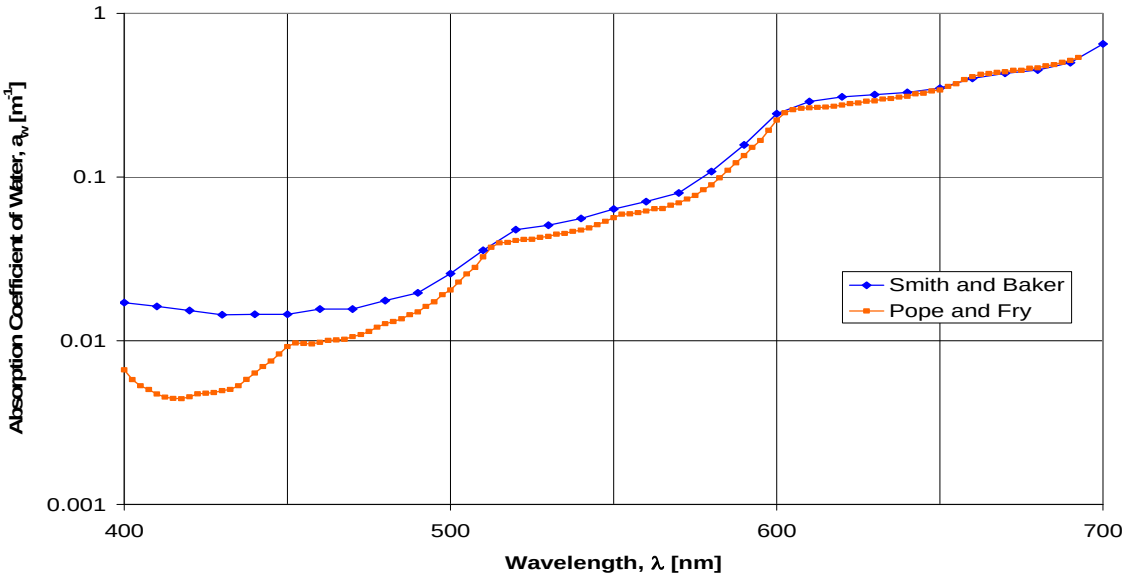

Figure 3 Logarithmic absorption coefficient versus wavelength for clear ocean waters. Experimental results published by Smith and Baker[4] and Pope and Fry.[7]

Both data sets are shown above because, although the result by Pope and Fry is considered more accurate,[7] the Smith and Baker absorption coefficients were used in this investigation. The absorption coefficient increases with increasing wavelength, so very little solar radiation at large wavelengths penetrates to great depths below the sea surface,[5] while wavelengths smaller than 550 nm can easily reach large depths. It is through Raman scattering that photons with wavelengths greater than 550 nm are detected at great depths in the ocean.

In order to determine the role that Raman scattering plays in creating the radiance field below the sea surface, two identical simulations were designed, both using the Case 1, two component water model, down through a geometric depth z = 1000 m. From a previous experiment,[8] Raman scattering is expected to have no effect on the radiance field for wavelengths smaller than 500 nm. The effect is then expected to increase with increasing wavelengths above 500 nm. In this investigation, four wavelengths were chosen: 460 nm, 500 nm, 540 nm, and 580 nm, to represent both sides of the 500 nm boundary, as well as the boundary itself. Recall that these are nominal wavelengths, and

represent the average values over a 20 nm band. For example, the radiance field at 460 nm is actually the average radiance in a band from 450 nm to 470 nm. The simulation parameters were identical for the two separate runs, except that the second run included the Raman scattering process in its calculations.

3.2 Simulation Results

3.2.1 460 nm

Incident solar radiation with a wavelength of 460 nm should have no trouble penetrating past 900 m below the ocean surface, since it is not absorbed as strongly as longer wavelengths by water molecules. Since Raman scattering occurs about once for every ten scatterings, it is expected that the solar radiance at 460 nm will greatly overpower the radiance of light Raman scattered to 460 nm from shorter wavelengths. Figure 4 and Figure 5 show a comparison between the radiance fields when Raman scattering is not included, and also when it is included.

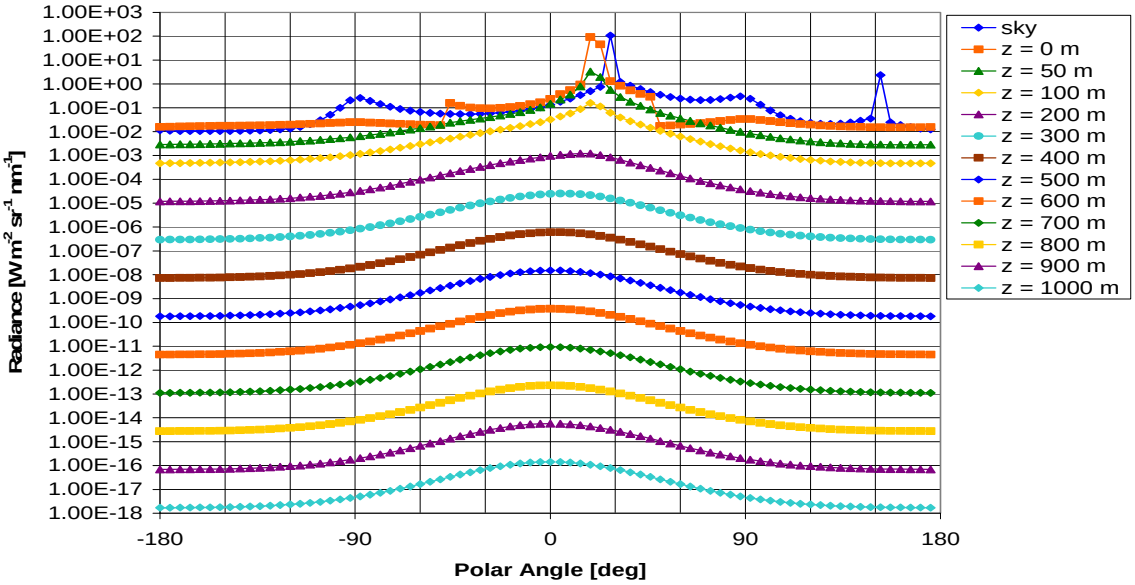

Figure 4 Logarithmic radiance versus polar angle for 460 nm light when Raman scattering is not included. Solar zenith angle 30 degrees. Wind speed, *w*, is 0 m/s. Chlorophyll Concentration 0.05 mg m^{-3}.

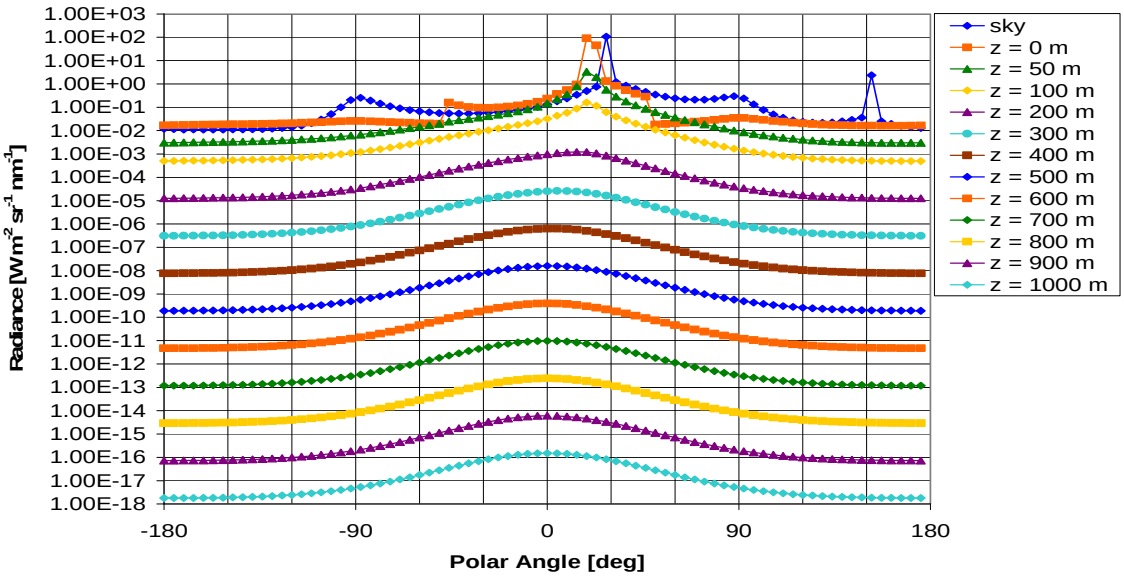

Figure 5 Logarithmic radiance versus polar angle for 460 nm light when Raman scattering is included. Solar zenith angle 30 degrees. Wind speed, *w*, is 0 m/s. Chlorophyll Concentration 0.05 mg m^{-3}.

The two plots above are identical. As expected, 460 nm light is not affected by Raman scattering.

3.2.2 500 nm

Since 500 nm is still below the 550 nm cut-off for incident solar radiation that reaches great depths in the ocean, it is expected that Raman scattering will only have a small effect on the radiance field. Figure 6 and Figure 7 show a comparison between the two radiance fields, with and without Raman scattering.

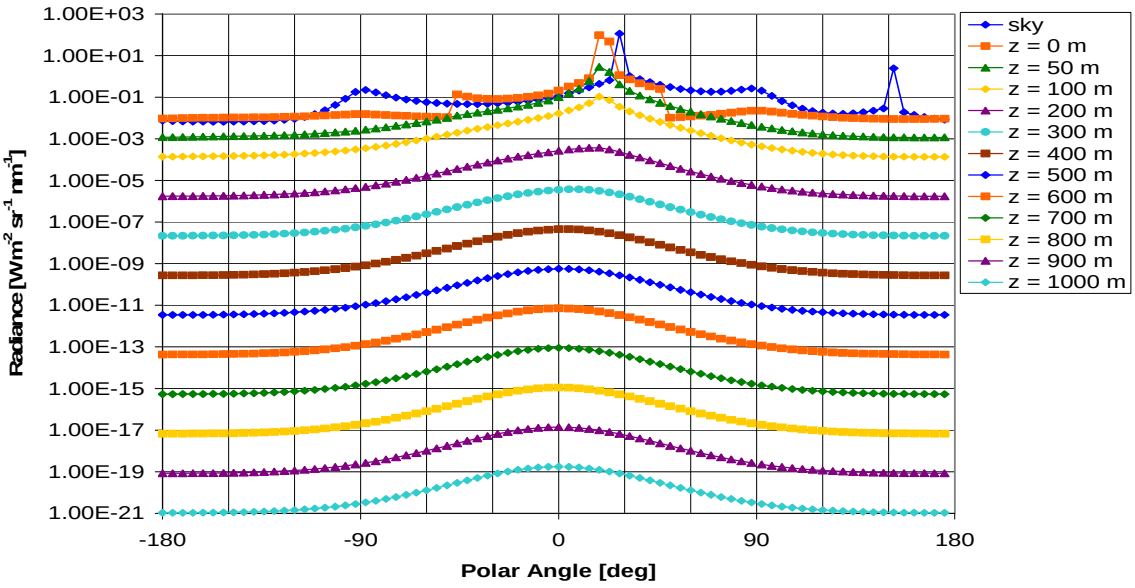

Figure 6 Logarithmic radiance versus polar angle for 500 nm light when Raman scattering is not included. Solar zenith angle 30 degrees. Wind speed, *w*, is 0 m/s. Chlorophyll Concentration 0.05 mg m^{-3}.

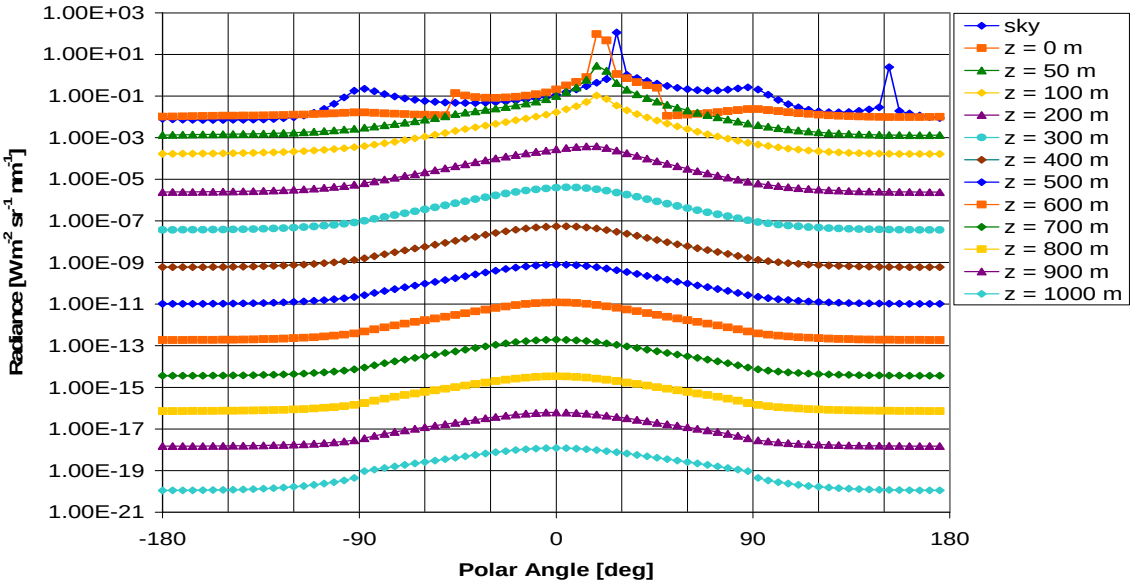

Figure 7 Logarithmic radiance versus polar angle for 500 nm light when Raman scattering is included. Solar zenith angle 30 degrees. Wind speed, *w*, is 0 m/s. Chlorophyll Concentration 0.05 mg m^{-3}.

Both Figure 6 and Figure 7 are plotted on the same radiance scale to highlight the differences between these two results. At the surface and in shallow water, down to 100 m, the results are identical. At depths below 100 m, however, the radiance field with Raman scattering included has an overall greater magnitude than the corresponding depths when Raman scattering is not included. The difference between the two results is only slight at 200 m. Then, as depth increases so does the discrepancy between the two simulated radiance fields. At and below 700 m, not only is the magnitude of the radiance field greater when Raman scattering is included, but the shape of the radiance field differs as well.

3.2.3 540 nm

For the radiance field with wavelength 540 nm, it is expected that that the effect of Raman scattering will be even greater than the effect seen for 500 nm. Figure 8 and Figure 9 show a comparison of the two simulations for wavelength 540 nm.

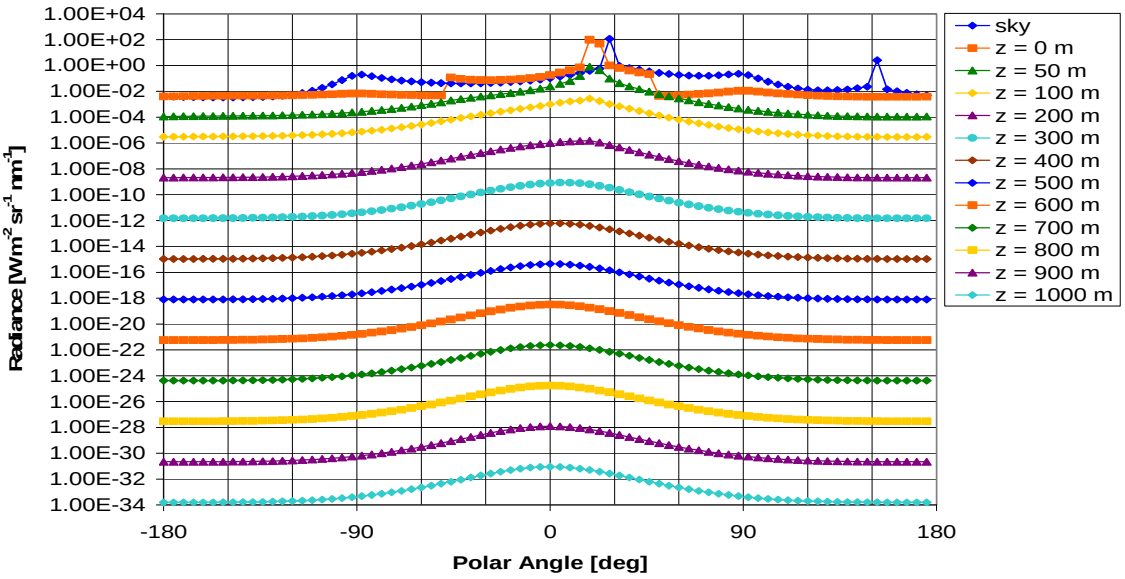

Figure 8 Logarithmic radiance versus polar angle for 540 nm light when Raman scattering is not included. Solar zenith angle 30 degrees. Wind speed, *w*, is 0 m/s. Chlorophyll Concentration 0.05 mg m^{-3}.

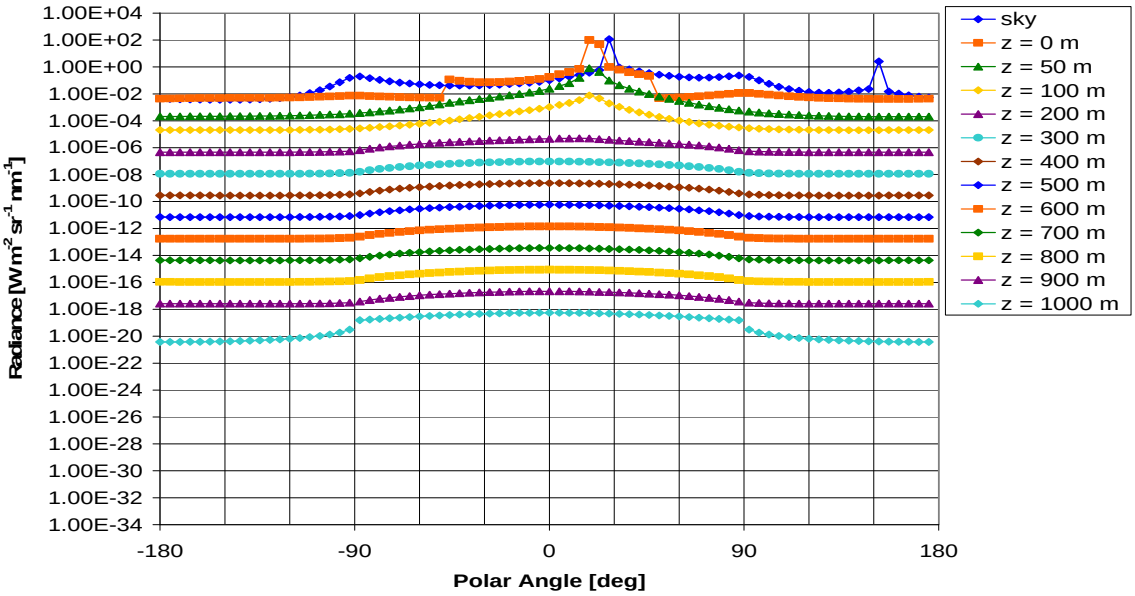

Figure 9 Logarithmic radiance versus polar angle for 540 nm light when Raman scattering is included. Solar zenith angle 30 degrees. Wind speed, *w*, is 0 m/s. Chlorophyll Concentration 0.05 mg m^{-3}.

Figure 8 and Figure 9 are both plotted onto the same radiance scale. It is clear that at 540 nm, Raman scattering has a large effect on the radiance field. There is an increase in magnitude of radiance when Raman scattering is included for all depths greater than 50 m. At 100 m, there is only a slight increase in magnitude. However, at 1000 m, the Raman scattered radiance field is more than 10 orders of magnitude greater than the solar incident, non-Raman, radiance. The shape of the radiance field is also different, between the two simulations, starting at a depth of 200 m.

3.2.4 580 nm

Taking the previous three results into account, it is expected that Raman scattering will have an even greater effect on the radiance field at 580 nm. Figure 10 and Figure 11 show a comparison of the two simulations, with and without Raman scattering, for that wavelength.

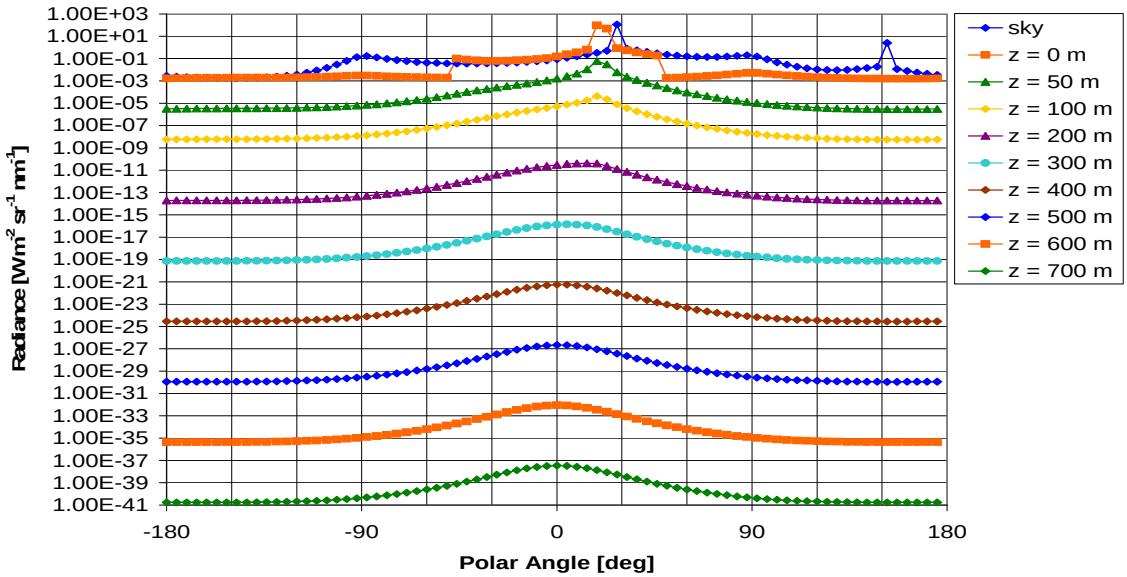

Figure 10 Logarithmic radiance versus polar angle for 580 nm light when Raman scattering is not included. Solar zenith angle 30 degrees. Wind speed, *w*, is 0 m/s. Chlorophyll Concentration 0.05 mg m^{-3}.

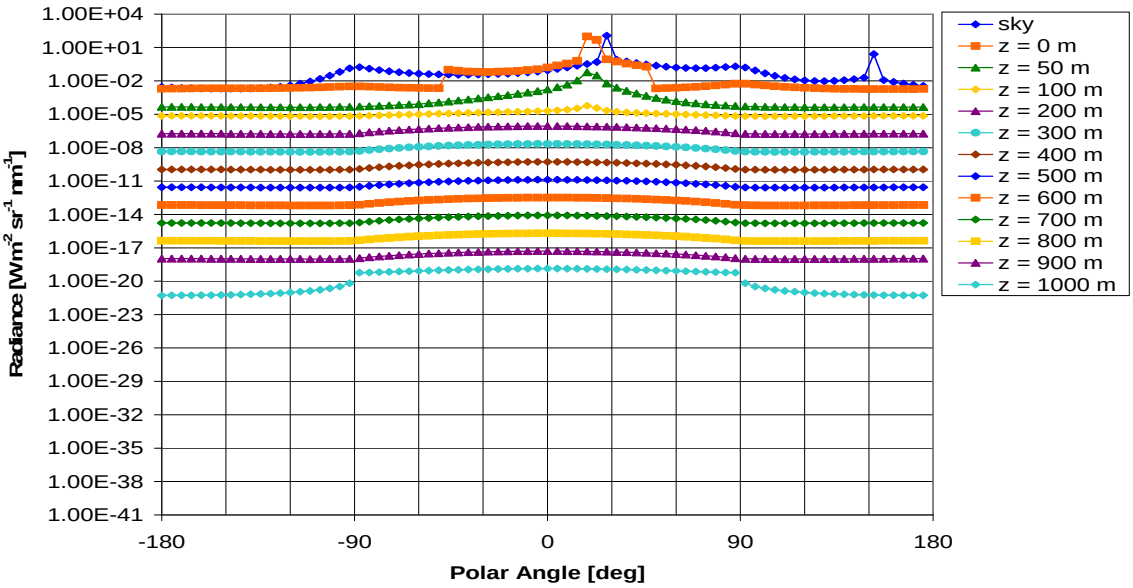

Figure 11 Logarithmic radiance versus polar angle for 580 nm light when Raman scattering is included. Solar zenith angle 30 degrees. Wind speed, *w*, is 0 m/s. Chlorophyll Concentration 0.05 mg m^{-3}.

Again, Figure 10 and Figure 11 are both plotted onto the same radiance scale. As expected, Raman scattering produces a large effect at this wavelength. In Figure 10, radiance data is only shown for depths down to 700 m because below that mark, the radiance at many of the points was identically zero. When Raman scattering is included, however, the radiance field at 700 m is more than 20 orders of magnitude greater than that of the solar incident field. Also, when Raman scattering is included, the radiance field at depths greater than 700 m has a large enough magnitude to be shown graphically.

3.3 Conclusions

As expected, Raman scattering must be included to accurately calculate the radiance field for wavelengths greater than, and including, 500 nm. Below that value, the magnitude of the incident solar radiation greatly overwhelms any photons that have been Raman scattered from even smaller wavelengths. However, at 500 nm, the photons Raman scattered from shorter wavelengths begin to outnumber the solar incident photons at large depths. For wavelengths greater than 550 nm, the estimated cut-off for solar incident light that is able to reach great depths in the ocean, the radiance field is dominated by photons which have been Raman scattered; These photons having been scattered from wavelengths that are able to penetrate deep into the ocean. Overall, the effect of Raman scattering begins to appear for light with wavelength 500 nm, and increases with increase in wavelength. Also, for a single wavelength of light, the effect of Raman scattering increases with increase in depth.

CHAPTER IV
THE ASYMPTOTIC REGION

4.1 Introduction

The asymptotic region is defined as the region of the water column within which the radiance field is independent of the sun's location, is vertically symmetric, and decays at a constant rate for all angles.[2] In order to determine the location of the asymptotic region, for both water models, Hydrolight 4.1 was run for many depths down to a large maximum depth. The radiance field in the principal plane was plotted, and the ratio of the radiance at consecutive depths was calculated. The asymptotic region was said to be achieved when the radiance field was symmetric about polar angle $\theta = 0$ degrees and the ratio of radiances was constant for all polar angle values.

4.2 One Component, Homogeneous Water Model

The one component, homogeneous water model was used for a single wavelength of light, namely 530 nm. The simulation calculated radiance data just above the sea surface, just below, and also for optical depths, τ = 2.5, 5, 7.5, 10, 15, 20, 25, 30, 35, 40, 45, 50, 55, and 60. The water model used a total extinction coefficient equal to 0.032 m^{-1}, so this set of optical depths corresponds to geometric depths, z = 78.125 m, 156.25 m, 234.375 m, 312.50 m, 468.75 m, 625.00 m, 781.25 m, 937.50 m, 1093.75 m, 1250.00 m, 1406.25 m, 1562.50 m, 1718.75 m, and 1875.00 m. The angular configuration used for this model was 180 μ by 24 ϕ were $\mu = \cos\theta$, θ is the polar angle, and ϕ is the azimuthal angle.

4.2.1 Single Scattering Albedo, $\omega_o = 0.5$

The initial investigation into the asymptotic region used single scattering albedo ω_o = 0.5. The single scattering albedo is defined as

$$\omega_o = \frac{b}{c} \tag{1}$$

where *b* is the total scattering coefficient and *c* is the total extinction coefficient. Figure 12 shows the radiance versus polar angle graph for this simulation.

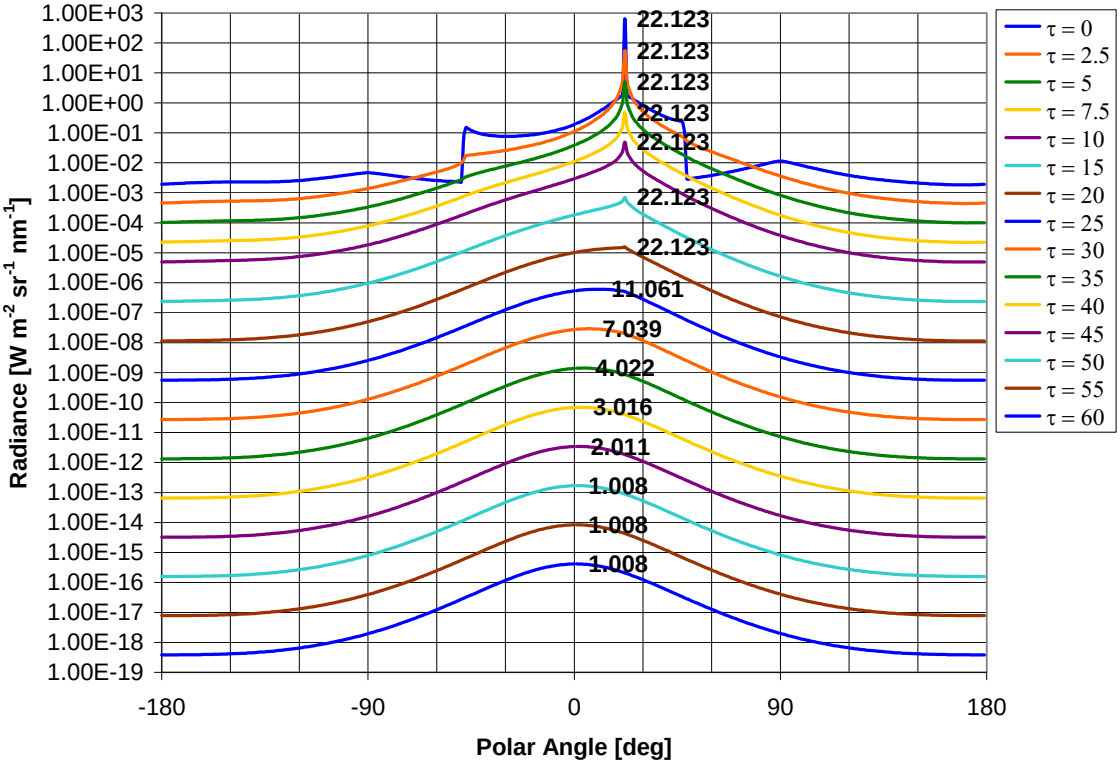

Figure 12 Logarithmic radiance versus polar angle for single scattering albedo, ω_o = 0. 5, extinction coefficient 0.032 m^{-1}. Solar zenith angle 30 degrees. Wind speed, *w*, is 0 m/s.

The numbers listed on the figure itself are the polar angle values of the radiance peak at each depth. For this water model, with a very high number of quads, and maximum depth of 1875.00 m, the asymptotic region is still not achieved. It is unnecessary to calculate the ratios of consecutive depths, because the radiance field is not symmetric about the vertical. This water model most accurately represents pure water, so this result leads to the conclusion that in ultra clear water, the asymptotic region may never be achieved.

4.2.2 Single Scattering Albedo, $\omega_o = 0.25$

Since the pure water model was not successful in generating an asymptotic region, the question was raised as to what the single scattering albedo must be in order to produce an asymptotic radiance field. Single Scattering Albedo, $\omega_o = 0.25$ was the next water model used. Figure 13 shows the radiance versus polar angle graph for this simulation.

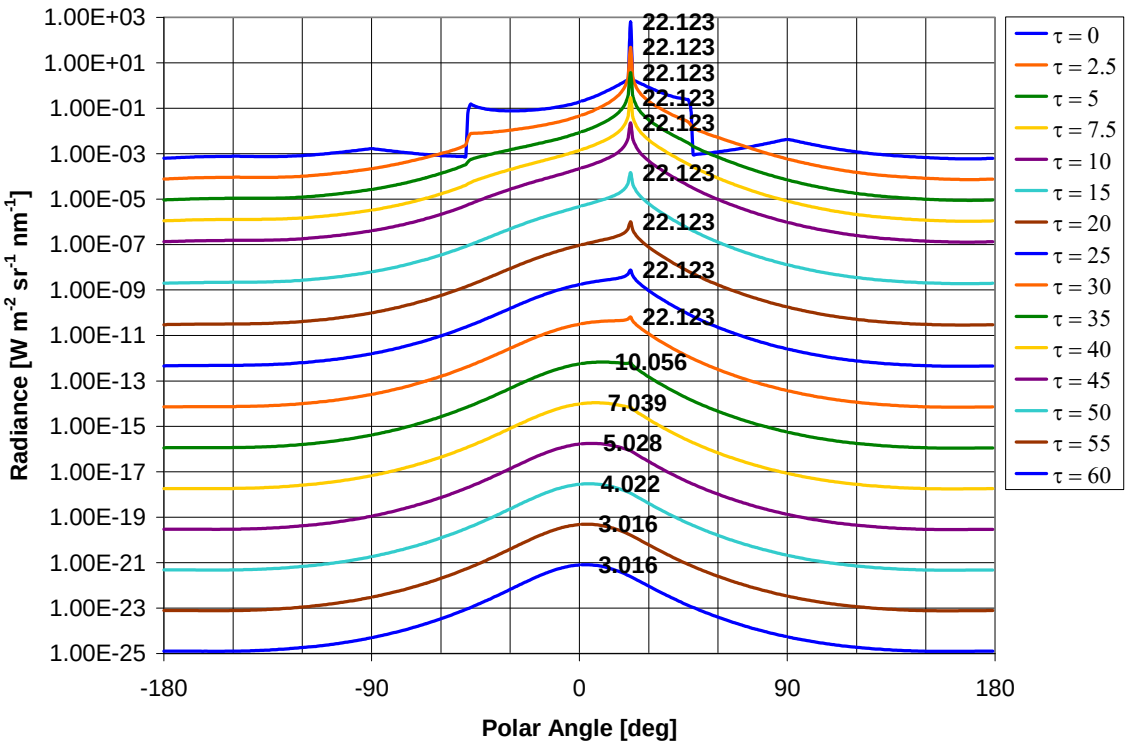

Figure 13 Logarithmic radiance versus polar angle for single scattering albedo, $\omega_o = 0.25$, extinction coefficient 0.032 m^{-1}. Solar zenith angle 30 degrees. Wind speed, *w*, is 0 m/s.

Again, the numbers listed on the plot itself are the polar angle values corresponding to the peak radiance at each depth. The single scattering albedo $\omega_o = 0.25$ means that for this simulation there was half as much scattering as in the previous simulation. Looking at the radiance plot, it is clear that the radiance field in this case is even further from the asymptotic region than the $\omega_o = 0.5$ radiance field.

4.2.3 Single Scattering Albedo, $\omega_o = 0.75$

Since decreasing the amount of scattering brought the radiance field further from the asymptotic region, it is expected that increasing the amount of scattering will generate the asymptotic region at some depth above 1875.00 m. The third simulation used single scattering albedo, $\omega_o = 0.75$. Figure 14 shows the radiance versus polar angle graph for this simulation.

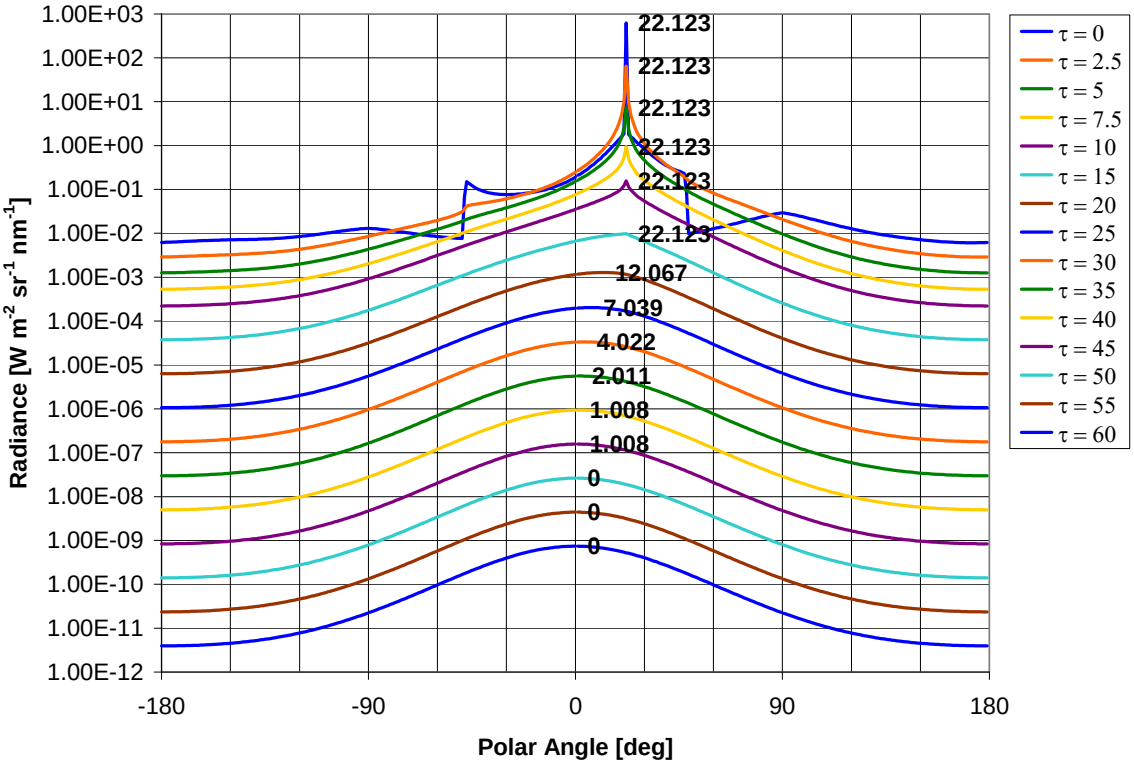

Figure 14 Logarithmic radiance versus polar angle for single scattering albedo, $\omega_o = 0.75$, extinction coefficient 0.032 m^{-1}. Solar zenith angle 30 degrees. Wind speed, *w*, is 0 m/s.

As shown by the polar angle values of the peak radiance at each depth, the radiance field is symmetric about the vertical for optical depths, $\tau = 50$, 55, and 60. This symmetry is

the first of two characteristics of the asymptotic region. If the asymptotic region begins at optical depth $\tau = 50$, it is expected that the ratio of the radiance at optical depth $\tau = 55$ to the radiance at optical depth $\tau = 50$ will be a constant for all polar angles. Likewise we expect constant ratios between the radiances at optical depth $\tau = 60$ and $\tau = 55$. However, when the calculation is performed, it is found that for nearly all polar angles, the ratio is a constant value, namely 1.68×10^{-1}. However, for a small number of polar angles the ratio is actually 1.67×10^{-1}. The ratio between the radiances at optical depths $\tau = 55$ and $\tau = 50$ also has a few polar angles with a ratio value of 1.69×10^{-1}. From this second check, it seems that although the radiance field is symmetric for those depths, it has not truly reached the asymptotic region.

4.2.4 Single Scattering Albedo, $\omega_o = 0.90$

After the simulation of the water model with single scattering albedo, $\omega_o = 0.75$ nearly achieved the asymptotic region before maximum depth 1875.00 m, it was expected that increasing the single scattering albedo even further would result in an asymptotic radiance field before the maximum simulated depth. Thus, the final one component water model had single scattering albedo $\omega_o = 0.90$. Figure 15 shows the radiance versus polar angle graph for this simulation.

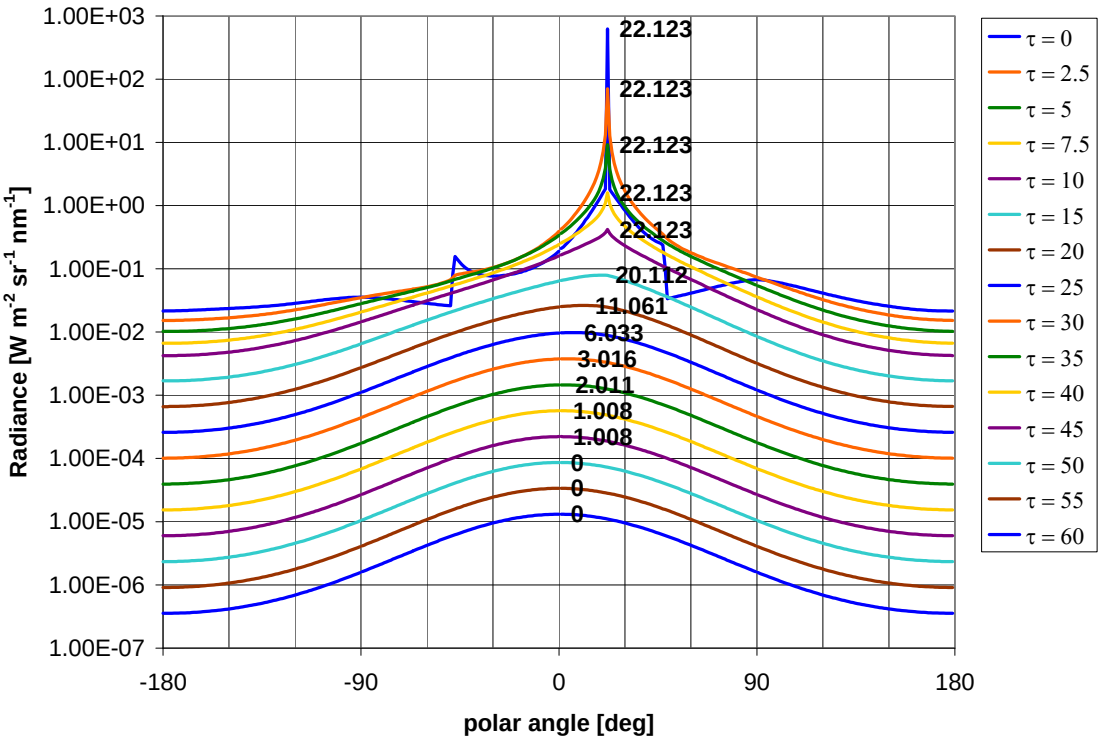

Figure 15 Logarithmic radiance versus polar angle for single scattering albedo, $\omega_o = 0.90$, extinction coefficient 0.032 m^{-1}. Solar zenith angle 30 degrees. Wind speed, *w*, is 0 m/s.

As with the single scattering albedo $\omega_o = 0.75$ case, the radiance field is symmetric about the vertical for optical depths, $\tau = 50$, 55, and 60. Again, the second step in determining if this is truly the asymptotic region is to calculate the ratio between the radiance at consecutive depths. Again, as in the case of $\omega_o = 0.75$, the ratio is nearly constant for all polar angle values. However, there is a small fraction of the ratios that differ from the overall constant. It seems, from the second analysis, that the one component homogeneous water model is not able to simulate the asymptotic region at reasonable depths, although the radiance field is very nearly asymptotic at depths below 1562.50 m.

4.3 Historical Case 1 Water Model

Initially, the investigation of the asymptotic region using the Case 1 water model with Raman scattering was conducted with chlorophyll concentration 0.0 mg m^{-3}. However,

the asymptotic radiance field could not be simulated, for any of the wavelengths, using this model. Therefore, a small amount of chlorophyll, concentration 0.05 mg m^{-3}, was included in the simulation. Raman scattering was also included. This second water model was able to generate asymptotic radiance fields for multiple wavelengths of light. Since different wavelengths were used, the radiance was calculated at geometric depths z = 0 m, 50 m, 100 m, 200 m, 300 m, 400 m, 500 m, 600 m, 700 m, 800 m, 900 m, 1000 m. Due to the number of calculations performed, over multiple wavelengths, it was necessary to reduce the angular configuration to 40 μ by 24 ϕ were $\mu = \cos\theta$, θ is the polar angle, and ϕ is the azimuthal angle.

4.3.1 460 nm

Although Raman scattering was included in this radiance field calculation, as shown in Chapter III, the effect of Raman scattering is negligible for wavelengths of light shorter than 500 nm. As such, for light with a wavelength of 460 nm, the shape of the radiance field within the asymptotic region should closely resemble the shape of the one component, homogeneous water model in that same region. Figure 16 shows the radiance versus polar angle graph for 460 nm light down to geometric depth 1000 m.

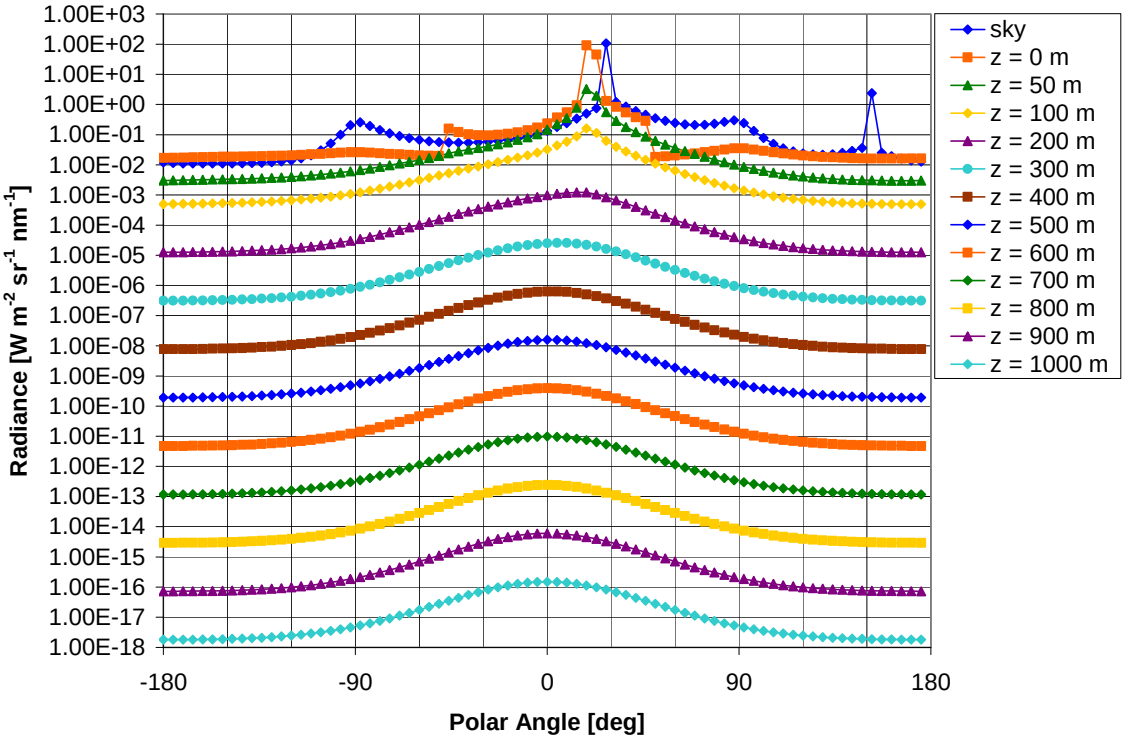

Figure 16 Logarithmic radiance versus polar angle for 460 nm light when Raman scattering is included, expanded radiance scale. Solar zenith angle 30 degrees. Wind speed, *w*, is 0 m/s. Chlorophyll concentration 0.05 mg m^{-3}.

The radiance field for wavelength 460 nm becomes symmetric about the vertical at or before geometric depth 500 m. However, the ratio of radiances at consecutive depths does not become constant for all angles until geometric depth 800 m. For the purposes of this study, the asymptotic region for 460 nm radiance field, is said to be between 800 m and 1000 m. The asymptotic region could very well continue will beyond 1000 m, but those depths were not a part of this investigation.

4.3.2 520 nm

As shown in Chapter III, the radiance field begins to show the effects of Raman scattering at wavelengths longer than 500 nm. For light with wavelength 520 nm, the effect of Raman scattering should be visible, but not large. So, it is interesting to note the location of the asymptotic region for this wavelength of light, and also to determine

the shape of the asymptotic radiance field. Figure 17 shows the radiance versus polar angle graph for 520 nm light down to geometric depth 1000 m.

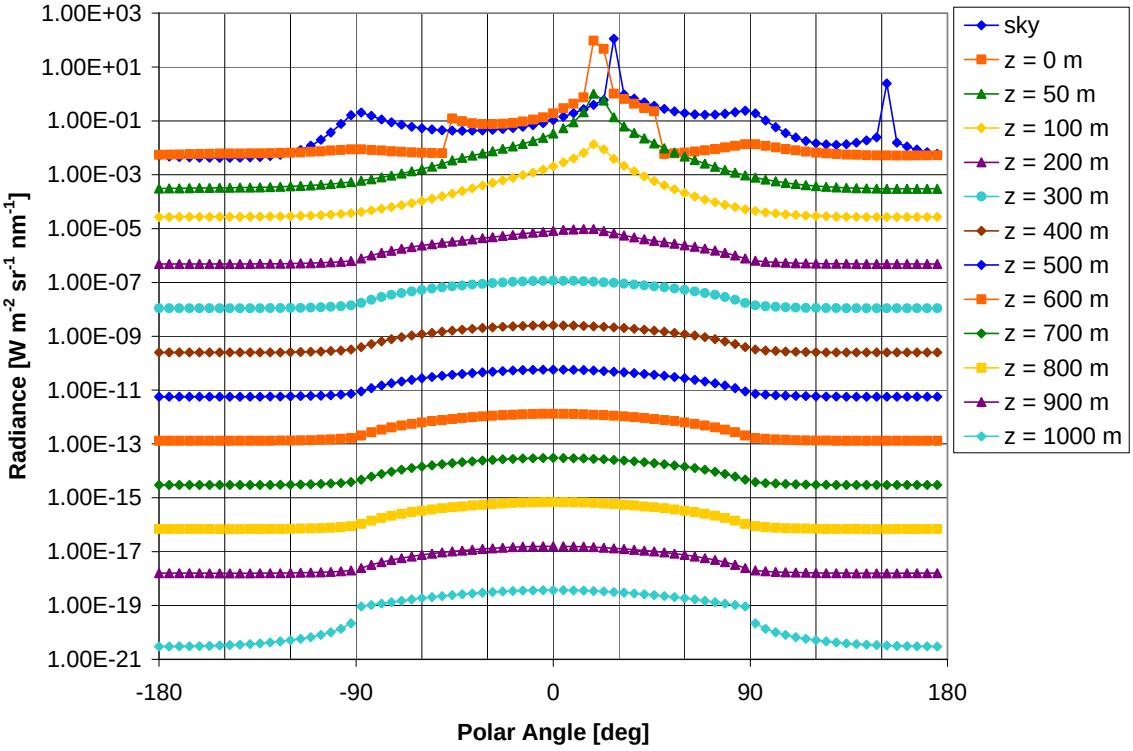

Figure 17 Logarithmic radiance versus polar angle for 520 nm light when Raman scattering is included. Solar zenith angle 30 degrees. Wind speed, *w*, is 0 m/s. Chlorophyll Concentration 0.05 mg m^{-3}.

The radiance field for 520 nm becomes symmetric about the vertical at or before geometric depth 400 m. The ratio between the radiance of consecutive depths becomes constant for all polar angles at 500 m and is no longer constant after 800 m. So, the asymptotic region for 520 nm light is said to be between 500 m and 800 m. The shape of the radiance field in this region is much flatter than in the asymptotic region for 460 nm. The photons that are Raman scattered to 520 nm, are originally solar incident photons wavelengths round 460 nm. So, although much of the radiance shown in Figure 17 came from photons that were a part of the radiance field in Figure 16, there is no correlation between the locations of the asymptotic region in both plots. The 460 nm

photons that were Raman scattered generate an asymptotic radiance field 300 m shallower than the 460 nm photons that were not Raman scattered.

4.3.3 580 nm

Where the radiance field for 520 nm was only slightly effected by Raman scattering, as shown in Chapter III, the Radiance field for 580 nm is almost entirely made up of Raman scattered photons, especially at depths greater than 50 m. Figure 18 shows the radiance versus polar angle graph for 580 nm light down to geometric depth 1000 m.

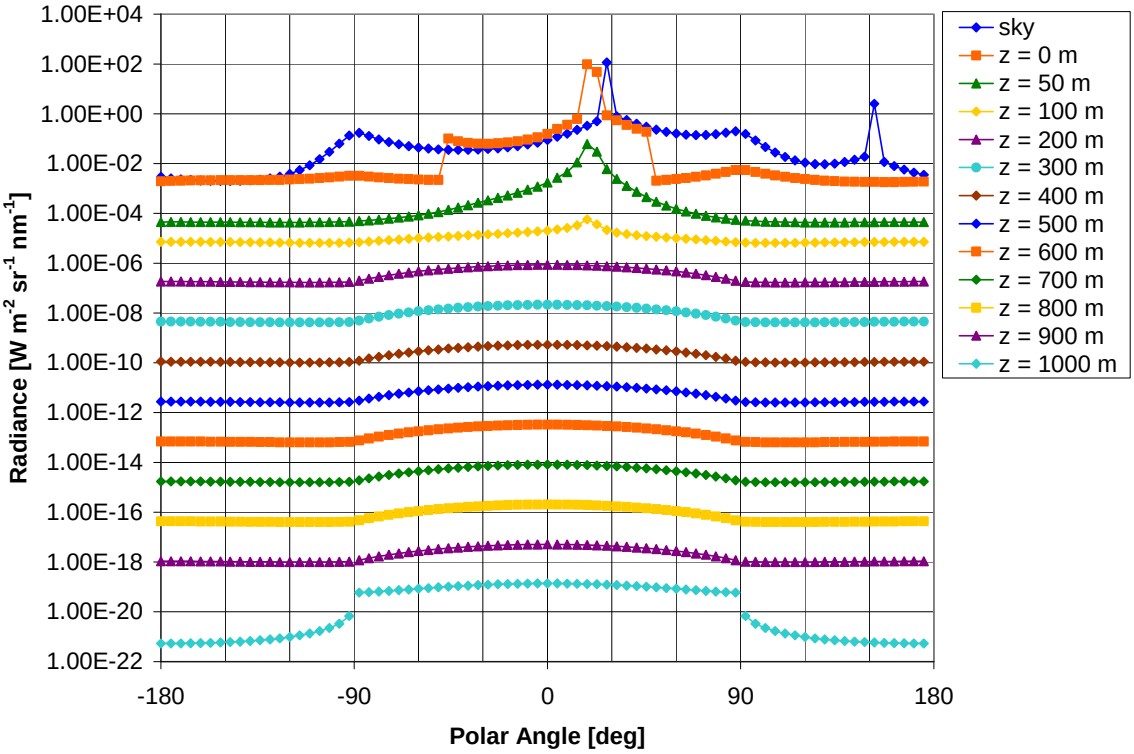

Figure 18 Logarithmic radiance versus polar angle for 580 nm light when Raman scattering is included, expanded radiance scale. Solar zenith angle 30 degrees. Wind speed, *w*, is 0 m/s. Chlorophyll Concentration 0.05 mg m^{-3}

The radiance field at 580 nm becomes symmetric about the vertical at or before geometric depth 300 m. However, the ratios of radiance for consecutive depths do not become constant until geometric depth 500 m. These ratios are no longer constant after geometric depth 900 m. So, the asymptotic region for 580 nm light is said to be from

500 m to 900 m below the ocean surface. The shape of the 580 nm radiance field within the asymptotic region is even flatter than that of the 520 nm radiance field.

4.4 Conclusions

It is not possible to achieve an asymptotic radiance field within a reasonable depth for water models that include only pure water. This is made clear for the one component, homogeneous water model. In that simulation, increasing the single scattering albedo caused the radiance field to be symmetric about the vertical at geometric depth 1562.50 m. However, it did not cause the radiance field to be truly asymptotic, not even at geometric depth 1875 m. It was also not possible to discover the asymptotic region using the two component water model, when the chlorophyll concentration was set to 0.0 mg m^{-3}.

It was possible to simulate the asymptotic radiance field using the two component water model with chlorophyll concentration 0.05 mg m^{-3}. Using this model, it was found that the asymptotic radiance field was flatter for wavelengths of light that were more effected by Raman scattering. It was also noted that the depth at which the asymptotic region was achieved for the 520 nm radiance field, had no co-relation to the depth at which the 460 nm radiance field reached the asymptotic region; even though the bulk of the photons in the 520 nm radiance distribution were Raman scattered to that wavelength from wavelengths near 460 nm.

CHAPTER V
THE EFFECT OF CHANGING THE MEAN SQUARE SLOPE

5.1 Introduction

In order to determine the properties of the radiance field just below the sea surface, an accurate model of the wind blown ocean surface must be developed. Where the specifics of each surface model can vary, in general each model must be developed in the same way. In *Light and Water* Curtis Mobley presents a general description of surface modeling.[5] When a numerical model is developed to treat the reflection and transmission of light between the sky and the ocean, through the ocean surface, each water wave is treated like a locally planar facet with a known slope. The surface is randomly generated with a mean slope of zero and water wave slope values normally distributed about the mean, with a variance corresponding to the wind speed. A directional beam of photons is added to the surface simulation and ray tracing is used to follow the beam as it interacts with individual facets of the sea surface. The known functions of geometric optics, Snell's Law and Fresnel's Formula, are used. Once many such simulations are performed, general directional reflection and transmission functions are determined through averaging. These general functions are then used to describe the wind blown surface in radiance transfer programs such as Hydrolight 4.1.

The variance, or mean square slope, of the simulated water waves is calculated by using the equation stated by Elfouhaily, et. al.[9]

$$\sigma^2 = \int_0^\infty k^2 S(k) dk \tag{2}$$

where the omnidirectional slope spectrum, $k^2S(k)dk$, must be integrated up to a maximum wave number, k, that represents an integration to infinity. The wave number, k, is for water waves. If the maximum wave number is too small, accuracy will be lost. A maximum wave number, k = 6283.185 rad m^{-1}, corresponding to cutoff wavelength λ = 0.001 m, was chosen to represent infinity. Then, three other maximum wave number

values were chosen to correspond to longer and longer cutoff wavelengths. The mean square slope was then calculated using the four *k* values. Table 1 shows each maximum wave number along with its corresponding wavelength and the calculated mean square slopes, σ^2, for wind speed 5 m/s.

Table 1 Integrated Mean Square Slope for wind speed 5 m/s up to the maximum wave number corresponding to each cut-off wavelength.

Wavelength λ [m]	Max Wave Number *k* [rad/m]	Mean Square Slope Wind = 5 m/s
0.001	6283.185	0.0293
0.040	157.080	0.0236
0.200	31.416	0.0191
0.800	7.854	0.0132

Then, the Cox and Munk[10] relation

$$\sigma^2 = 0.003 + 0.00512w \tag{3}$$

was used to calculate a corresponding wind speed, *w*, related to each mean square slope value. Table 2 shows the wind speed values that were used to run the Hydrolight 4.1 software and determine the effect of changing the variance, or mean square slope; although the program only allows wind speed values out to the hundredths place. We also ran Hydrolight 4.1 at wind speed 0 m/s to serve as a comparison.

Table 2 Corresponding wind speed to each integrated mean square slope.

Mean Square Slope Wind = 5 m/s	Corresponding Wind Speed [m/s]
0.0293	5.138
0.0236	4.015
0.0191	3.149
0.0132	1.993

The simulation was run for both the one component, homogeneous water model and the historical Case 1 water model.

5.2 One Component, Homogeneous Water Model

In order to determine the effect of changing the mean square slope on the radiance field, the Hydrolight 4.1 results for each of the four cutoff wavelengths were plotted together at each output depth. For this water model, since it is a single wavelength model, the radiance data was calculated for depths just above the sea surface as well as optical depths $\tau = 0$, 1, 2, 5, and 10. These optical depths correspond to geometric depths $z = 0$ m, 31.25 m, 62.50 m, 156.25 m, and 312.50 m.

The data corresponding to cutoff wavelength $\lambda = 0.001$ m was considered the ideal case. To measure the effect of changing the mean square slope, the percent difference was calculated between the radiance for the other cutoff wavelengths and that of the $\lambda = 0.001$ m case. Both the radiance plot and the percent difference plot are shown for each output depth. Figure 19 shows the radiance versus polar angle dependence, for each cutoff wavelength, above the sea surface. The curve for wind speed 0 m/s is also included for comparison. Figure 20 shows the percent difference to the $\lambda = 0.001$ case for each cutoff wavelength, above the sea surface.

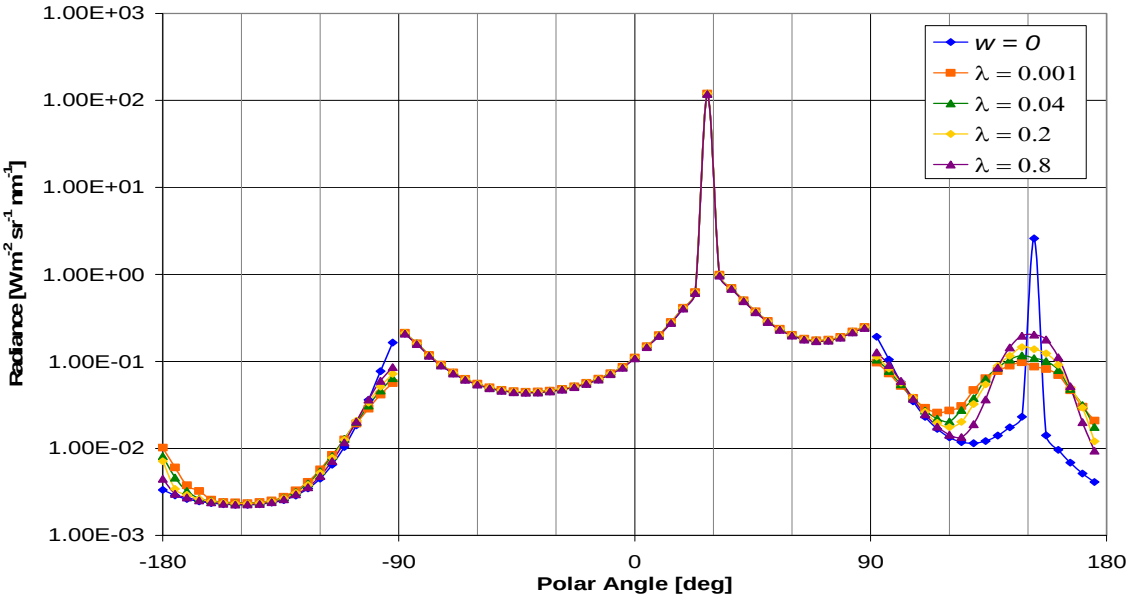

Figure 19 Logarithmic radiance versus polar angle for one component water at multiple K_{max} values, just above the surface. K_{max} values correspond to cut-off wavelengths 0.001, 0.04, 0.2, and 0.8 meters. Solar zenith angle 30 degrees. Wind speed, *w*, of 0 m/s is included as a comparison.

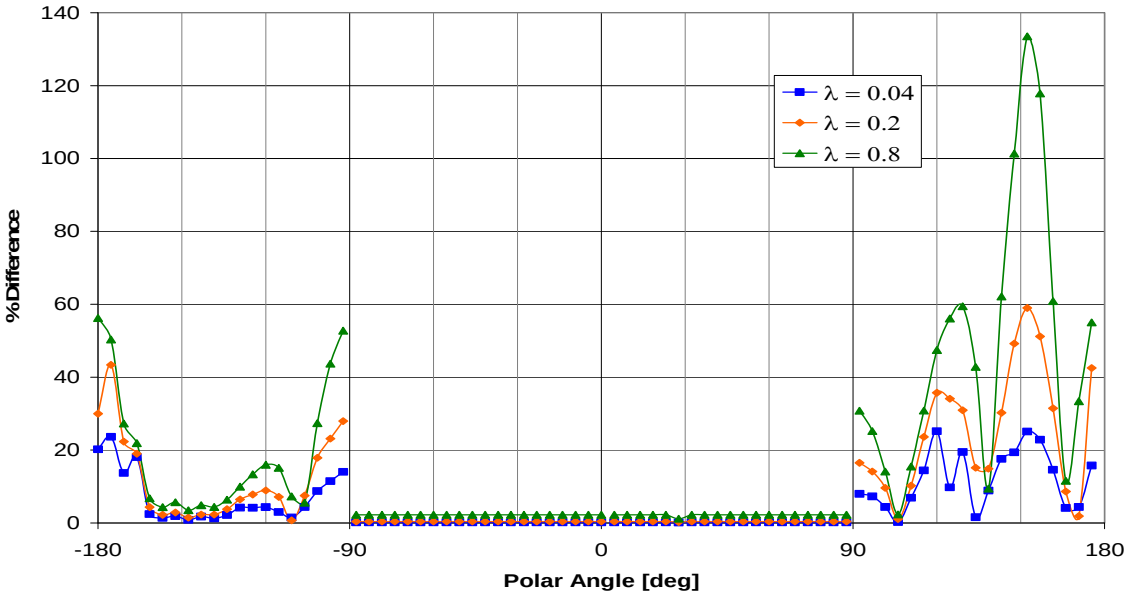

Figure 20 Percent difference versus polar angle for one component water, just above the sea surface. Percent difference is between the radiance of longer cut-off wavelengths and the λ = 0.001 case. Solar zenith angle 30 degrees.

From polar angles -90 degrees to 90 degrees there is no difference in radiance just above the sea surface with changing wind speed. This makes sense because polar angle zero degrees corresponds to downwelling radiation (the detector is directly upward) and Hydrolight does not consider the interaction between the ocean and the atmosphere. The downward detector orientations show greater percent difference with each longer cut-off wavelength, or smaller maximum wave number.

Figure 21 shows the radiance versus polar angle dependence, for each cutoff wavelength, just below the sea surface. The curve for wind speed 0 m/s is also included for comparison. Figure 22 shows the percent difference to the $\lambda = 0.001$ case for each cutoff wavelength, just below the sea surface.

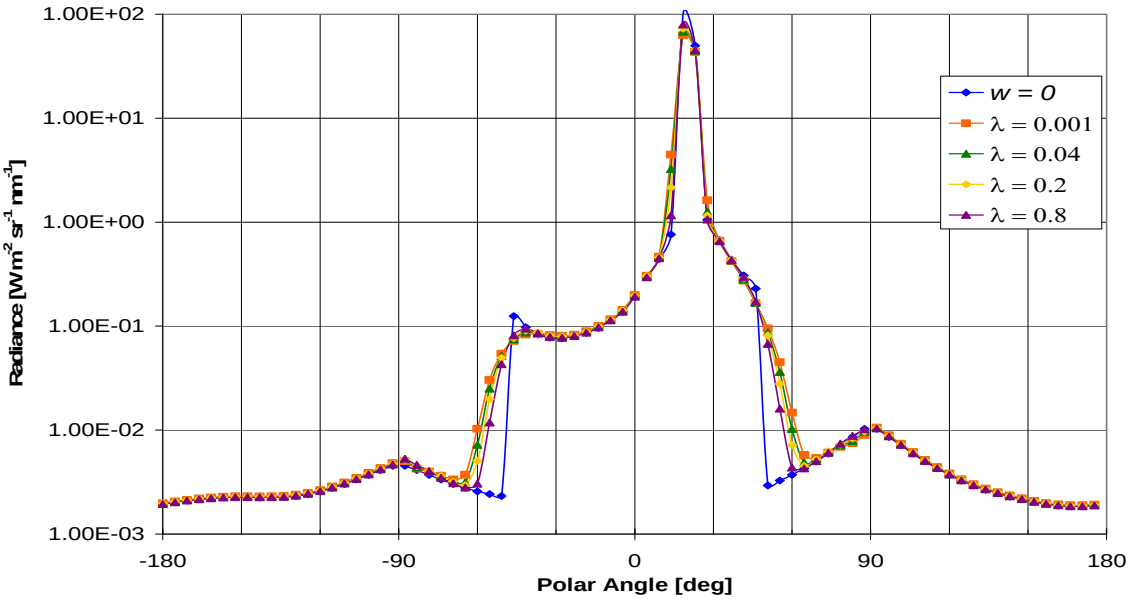

Figure 21 Logarithmic radiance versus polar angle for one component water at multiple K_{max} values, just below the surface. K_{max} values correspond to cut-off wavelengths 0.001, 0.04, 0.2, and 0.8 meters. Solar zenith angle 30 degrees. Wind speed, *w*, of 0 m/s is included as a comparison.

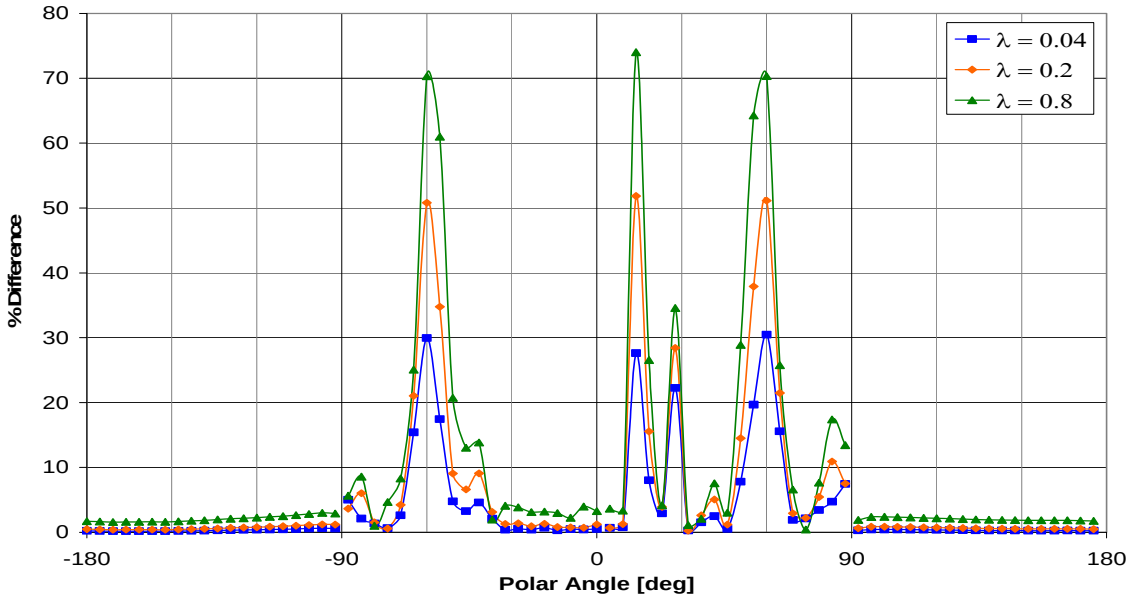

Figure 22 Percent difference versus polar angle for one component water, just below the sea surface. Percent difference is between the radiance of longer cut-off wavelengths and the λ = 0.001 case. Solar zenith angle 30 degrees.

The maximum percent difference is found around -48 degrees and 48 degrees, which is the critical angle for a flat sea surface. There is also a significant difference in the solar beam, located between polar angles 14 degrees and 30 degrees. As with the detectors above the sea surface, the data for longest cut-off wavelength also shows the largest percent difference to the value for the non-truncated spectrum.

Those relationships continue as detectors are placed at increasing depth. Figure 23 and Figure 24 show the radiance and percent difference relations at optical depth $\tau = 1$, which is a geometric depth of 31.25 meters.

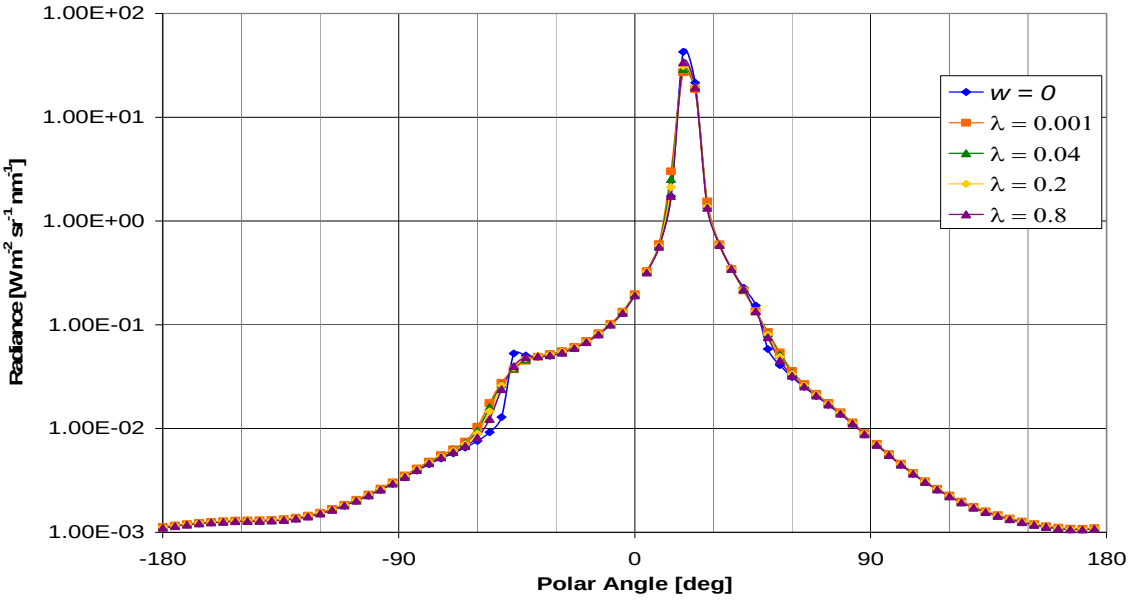

Figure 23 Logarithmic radiance versus polar angle for one component water at multiple K_{max} values, at optical depth $\tau = 1$. K_{max} values correspond to cut-off wavelengths 0.001, 0.04, 0.2, and 0.8 meters. Solar zenith angle 30 degrees. Wind speed, *w*, of 0 m/s is included as a comparison.

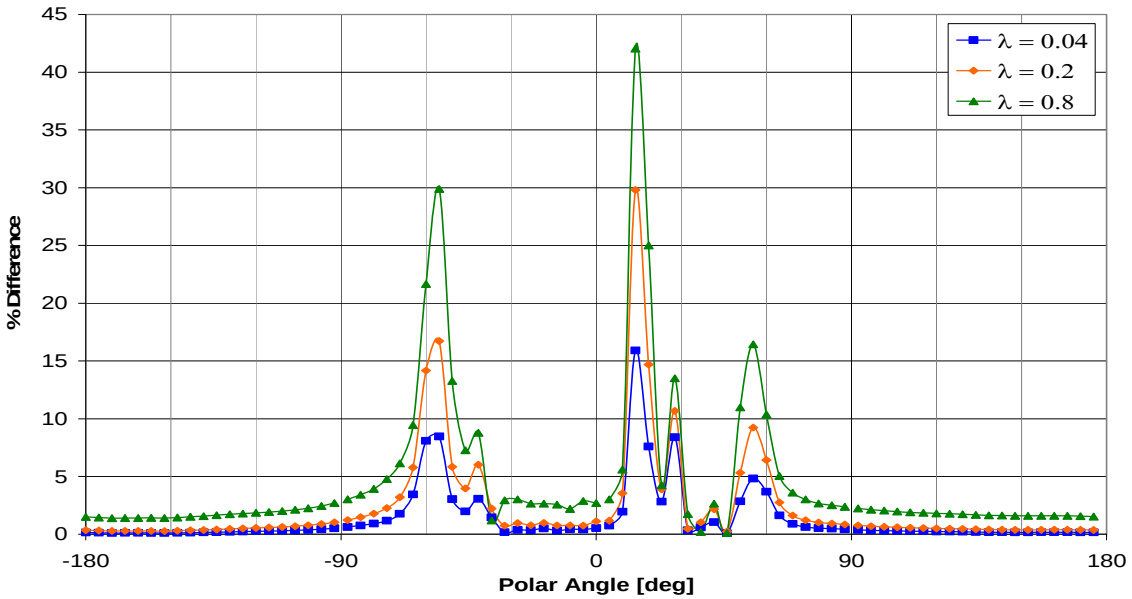

Figure 24 Percent difference versus polar angle for one component water, optical depth $\tau = 1$. Percent difference is between the radiance of longer cut-off wavelengths and the $\lambda = 0.001$ case. Solar zenith angle 30 degrees.

Unlike the percent difference plot just below the sea surface, at optical depth $\tau = 1$, the peaks in percent difference near the critical angle, around 48 degrees and -48 degrees, are not of equal value. In the subsequent depths, the peak percent differences near the critical angle continue to be unequal. Figure 25 and Figure 26 show the radiance and percent difference relationships at optical depth $\tau = 2$ below the surface, which is geometric depth z = 62.5 m. The solar zenith angle is 30 degrees.

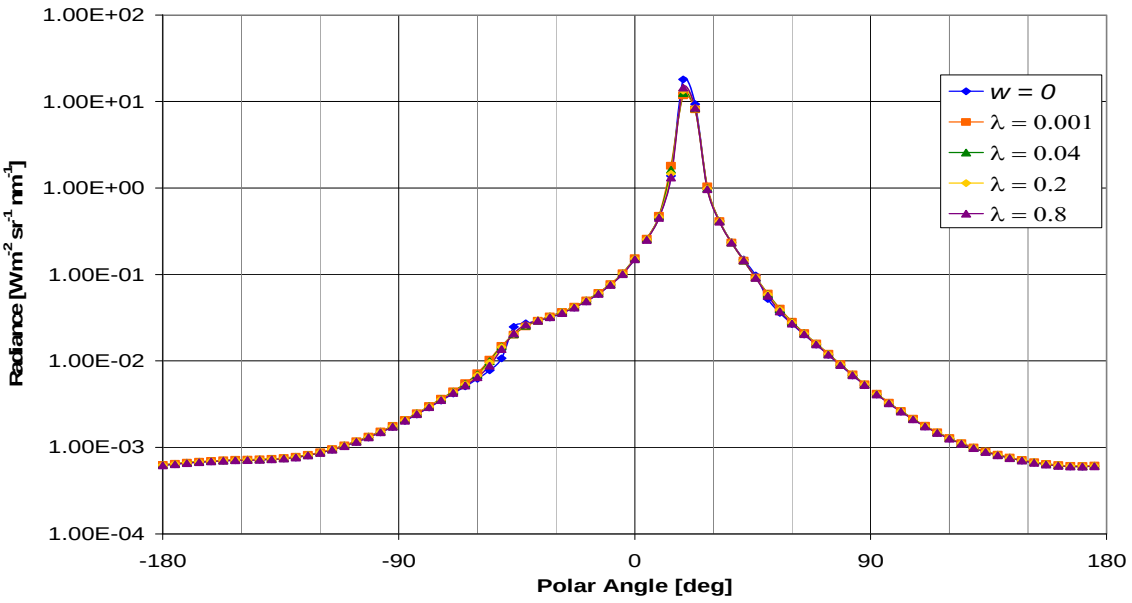

Figure 25 Logarithmic radiance versus polar angle for one component water at multiple K_{max} values, at optical depth $\tau = 2$. K_{max} values correspond to cut-off wavelengths 0.001, 0.04, 0.2, and 0.8 meters. Solar zenith angle 30 degrees. Wind speed, *w*, of 0 m/s is included as a comparison.

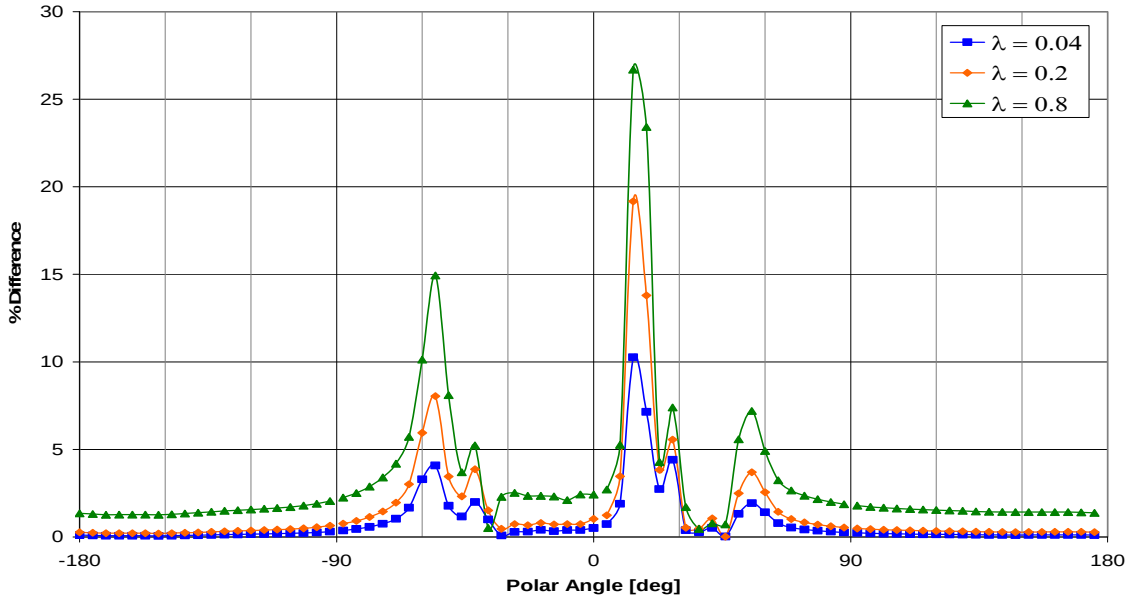

Figure 26 Percent difference versus polar angle for one component water, optical depth $\tau = 2$. Percent difference is between the radiance of longer cut-off wavelengths and the $\lambda = 0.001$ case. Solar zenith angle 30 degrees.

Figure 27 and Figure 28 show the radiance and percent difference relationships at optical depth $\tau = 5$ below the ocean surface, which is geometric depth z = 156.25 m.

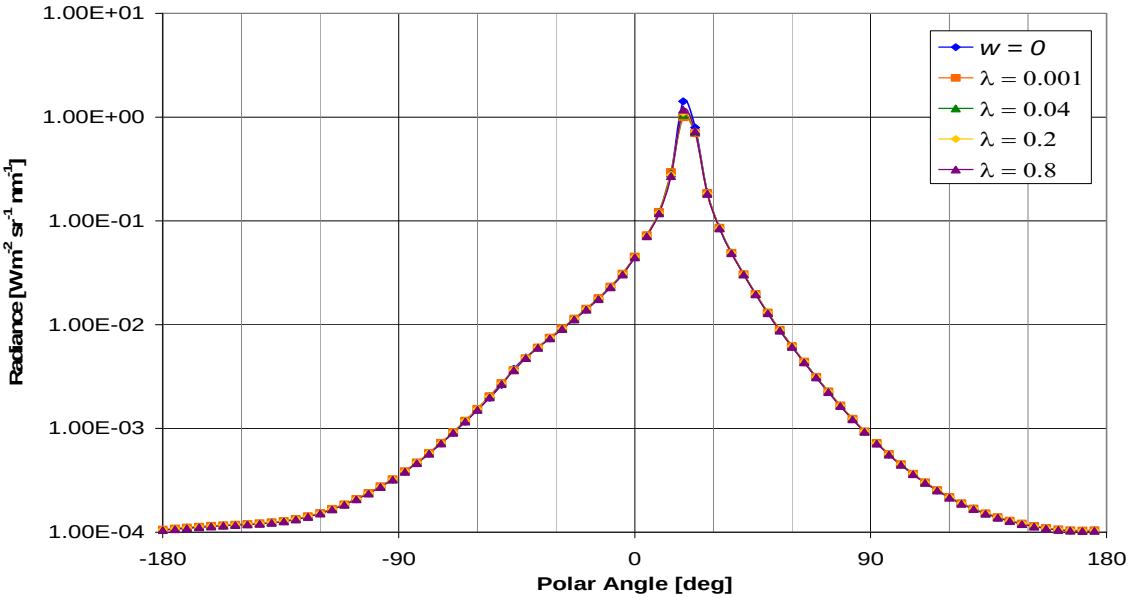

Figure 27 Logarithmic radiance versus polar angle for one component water at multiple K_{max} values, at optical depth $\tau = 5$. K_{max} values correspond to cut-off wavelengths 0.001, 0.04, 0.2, and 0.8 meters. Solar zenith angle 30 degrees. Wind speed, *w*, of 0 m/s is included as a comparison.

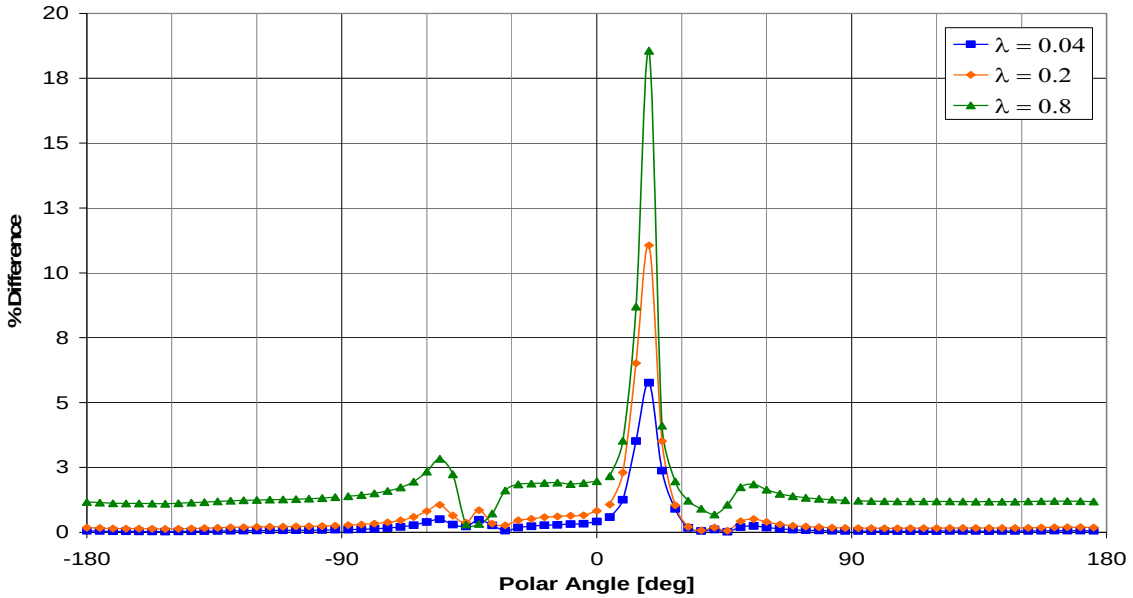

Figure 28 Percent difference versus polar angle for one component water, optical depth $\tau = 5$. Percent difference is between the radiance of longer cut-off wavelengths and the $\lambda = 0.001$ case. Solar zenith angle 30 degrees.

Figure 29 and Figure 30 show the radiance and percent difference relationships at optical depth $\tau = 10$ below the sea surface, which is geometric depth z = 312.50 m.

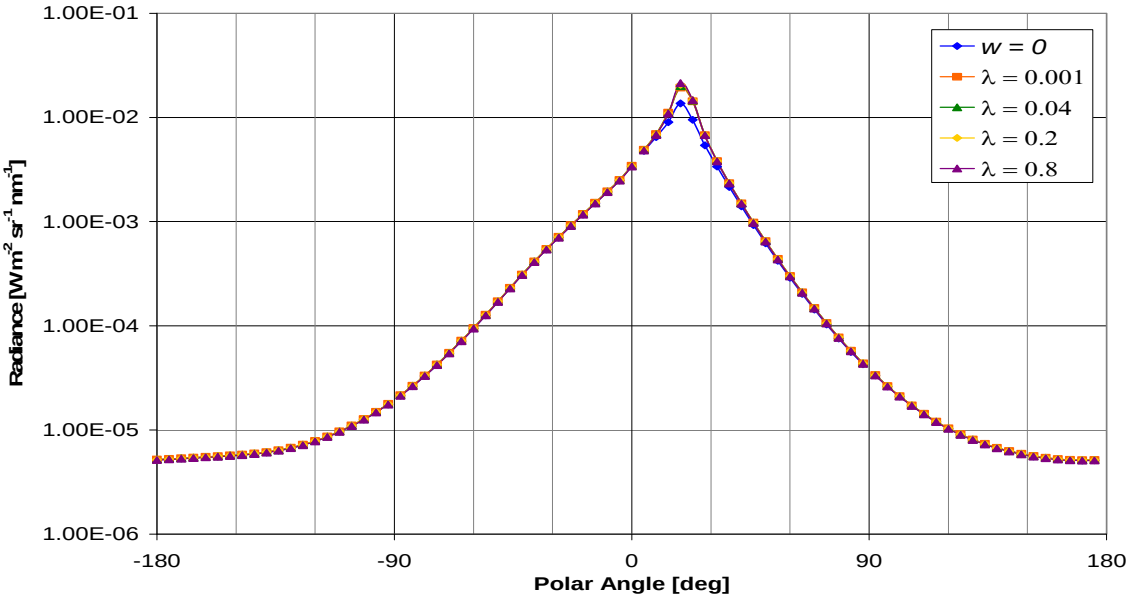

Figure 29 Logarithmic radiance versus polar angle for one component water at multiple K_{max} values, at optical depth $\tau = 10$. K_{max} values correspond to cut-off wavelengths 0.001, 0.04, 0.2, and 0.8 meters. Solar zenith angle 30 degrees. Wind speed, *w*, of 0 m/s is included as a comparison.

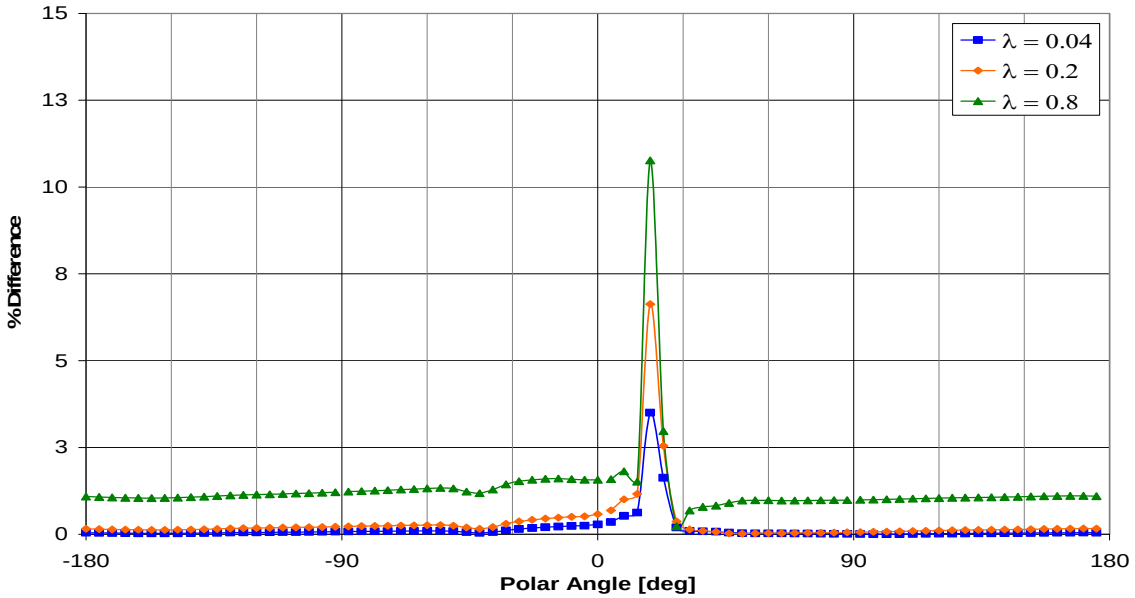

Figure 30 Percent difference versus polar angle for one component water, optical depth $\tau = 10$. Percent difference is between the radiance of longer cut-off wavelengths and the $\lambda = 0.001$ case. Solar zenith angle 30 degrees.

For shallow optical depths, there is a large percent difference in radiance in both the diffuse and beam regions. Initially, the peaks in percent differences are all nearly the same magnitude. As depth is increased, the peaks near the critical angle decrease more quickly than the peak in the solar beam region. Overall, as depth is increased, the percent difference to the ideal case decreases. In general, changing the mean square slope by removing the shorter wavelengths from the integral calculation, by integrating to a smaller maximum wave number, has a definite effect on the outcome of the radiance simulation. This effect is less at greater depths.

4.3 Historical Case 1 Water Model

The simulation that was performed for the one component homogeneous water model, was run again, only this time using the Case 1 water model with chlorophyll concentration 0.05 mg m^{-3}. Raman scattering was also included. Because the Case 1 water model simulation was able to produce an asymptotic radiance field for multiple wavelengths, the effect of changing mean square slope is determined for four distinct regions within the water column. The first region is near the surface, at geometric

depths z = 0 m, 10 m, 30 m, and 50 m. The second region is the intermediate region, located between geometric depth z =100 m and the beginning of the asymptotic region. The third region is the asymptotic region. The fourth and last region is below the asymptotic region. The location of each region is different for each of the three wavelengths considered, so each wavelength is presented individually.

4.3.1 460 nm

As shown in Chapter IV, the asymptotic region for the 460 nm radiance field lies between geometric depths 800 m and 1000 m. Figure 31 and Figure 32 show the radiance and percent difference relationships at geometric depths z = 0 m for the 460 nm radiance field.

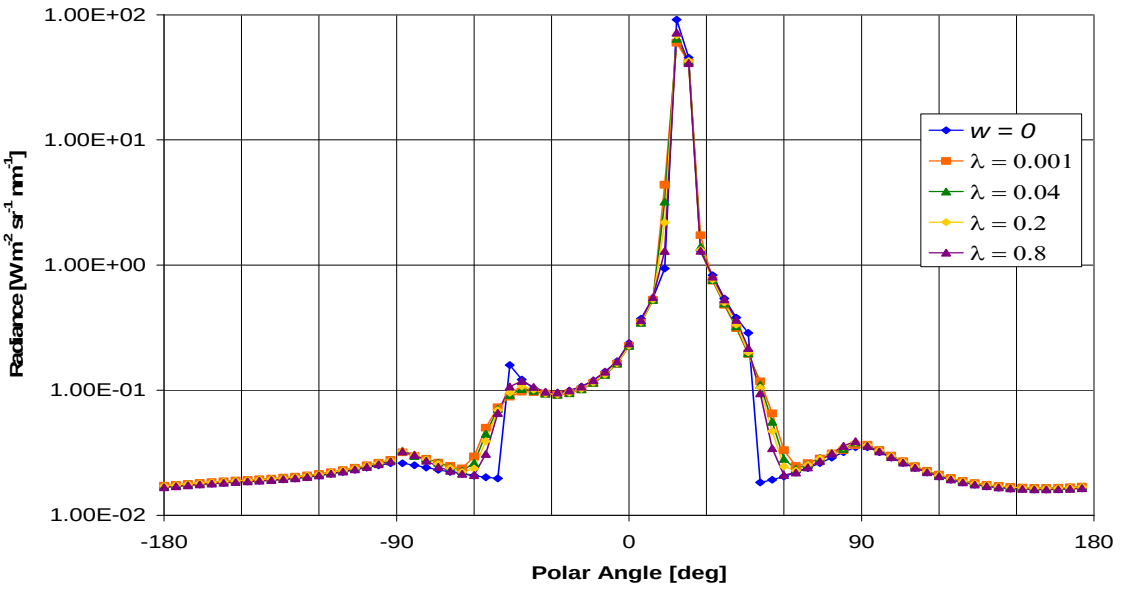

Figure 31 Logarithmic radiance versus polar angle for 460 nm light at multiple K_{max} values, geometric depth z = 0 m. K_{max} values correspond to cut-off wavelengths 0.001, 0.04, 0.2, and 0.8 meters. Solar zenith angle 30 degrees. Wind speed, *w*, of 0 m/s is included as a comparison.

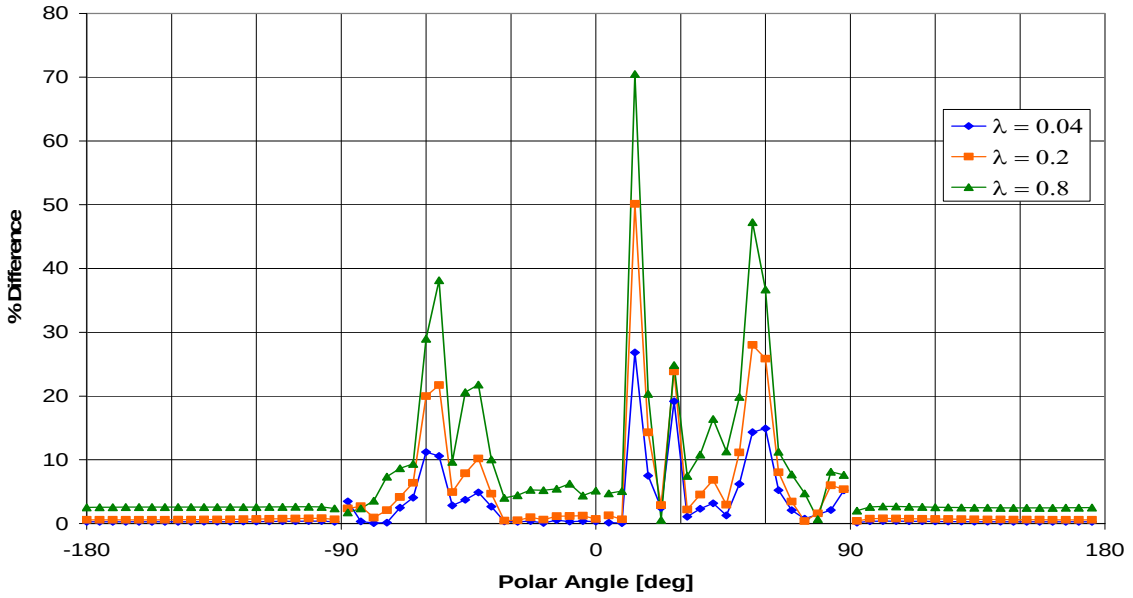

Figure 32 Percent difference versus polar angle for 460 nm light detectors at geometric depth z = 0 m. Percent difference is between longer cut-off wavelengths and the λ = 0.001 case. Solar zenith angle 30 degrees.

Figure 33 and Figure 34 show the radiance and percent difference relationships at geometric depths z = 10 m for the 460 nm radiance field.

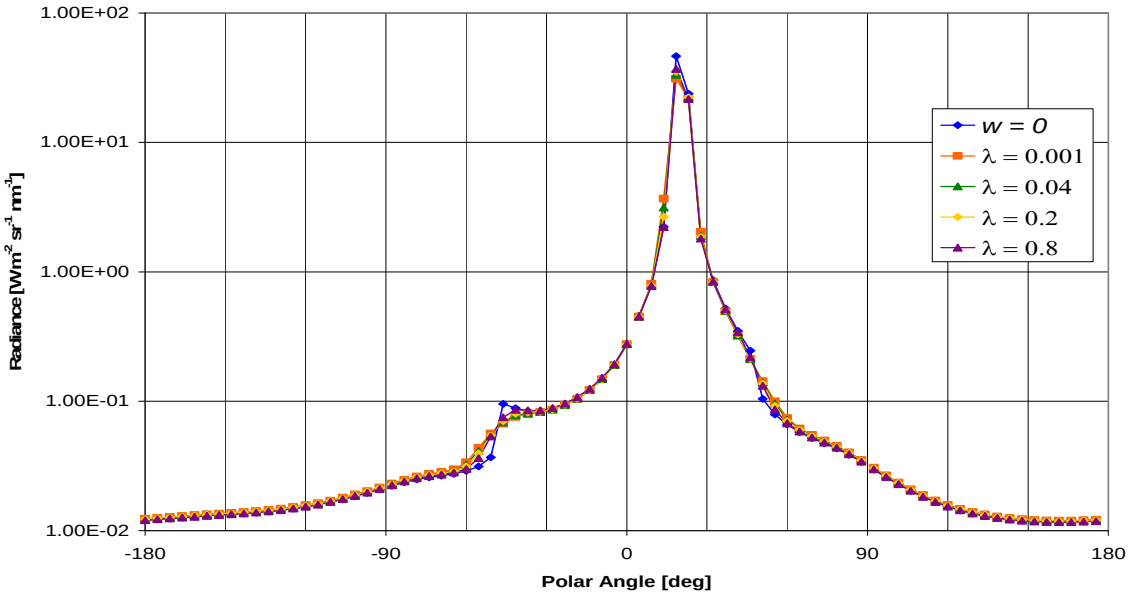

Figure 33 Logarithmic radiance versus polar angle for 460 nm light at multiple K_{max} values, geometric depth z = 10 m. K_{max} values correspond to cut-off wavelengths 0.001, 0.04, 0.2, and 0.8 meters. Solar zenith angle 30 degrees. Wind speed, *w*, of 0 m/s is included as a comparison..

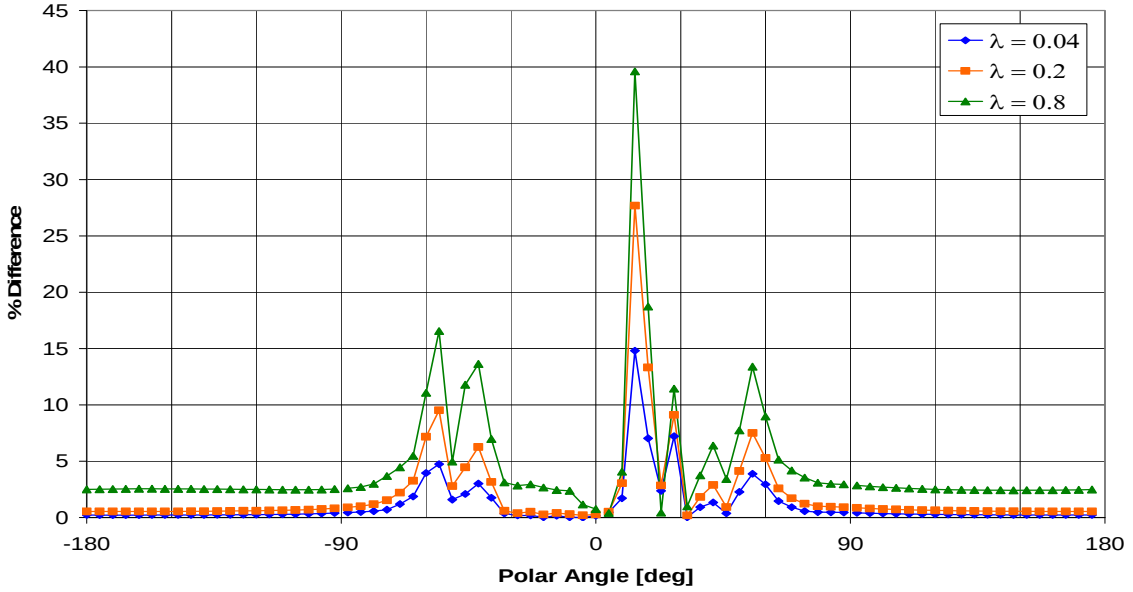

Figure 34 Percent difference versus polar angle for 460 nm light detectors at geometric depth z = 10 m. Percent difference is between longer cut-off wavelengths and the λ = 0.001 case. Solar zenith angle 30 degrees.

Figure 35 and Figure 36 show the radiance and percent difference relationships at geometric depths z = 30 m for the 460 nm radiance field.

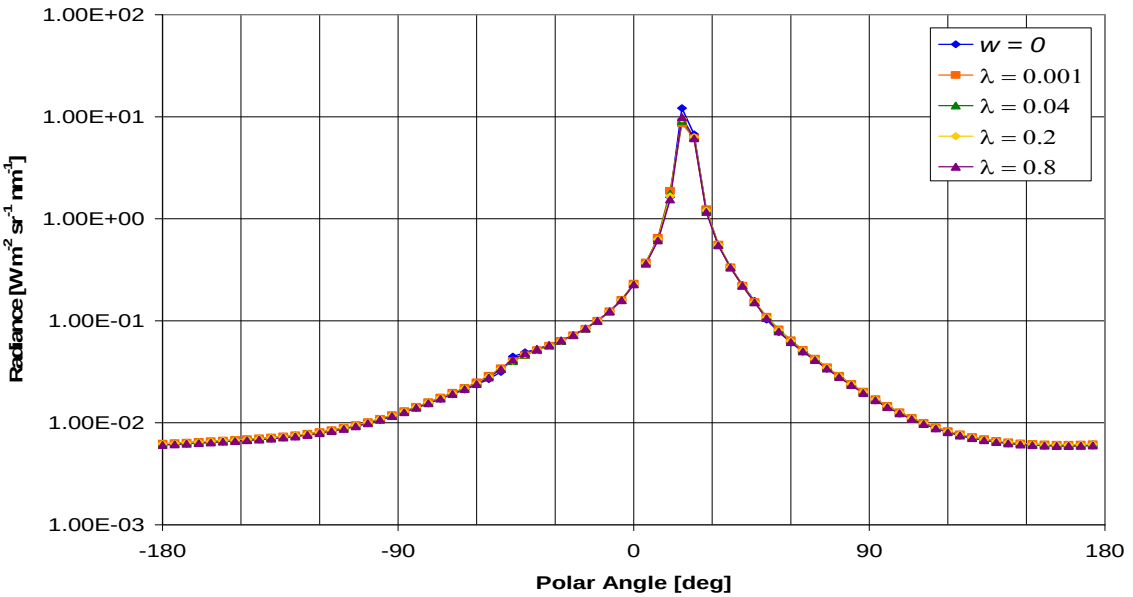

Figure 35 Logarithmic radiance versus polar angle for 460 nm light at multiple K_{max} values, geometric depth z = 30 m. K_{max} values correspond to cut-off wavelengths 0.001, 0.04, 0.2, and 0.8 meters. Solar zenith angle 30 degrees. Wind speed, *w*, of 0 m/s is included as a comparison.

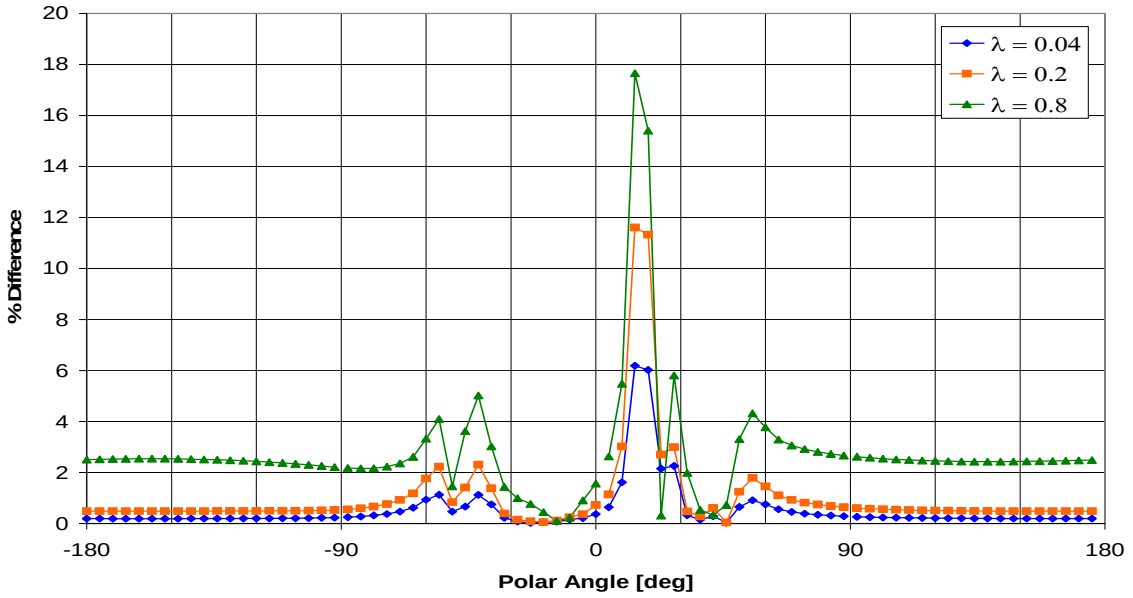

Figure 36 Percent difference versus polar angle for 460 nm light detectors at geometric depth z = 30 m. Percent difference is between longer cut-off wavelengths and the λ = 0.001 case. Solar zenith angle 30 degrees.

Figure 37 and Figure 38 show the radiance and percent difference relationships at geometric depths z = 50 m for the 460 nm radiance field.

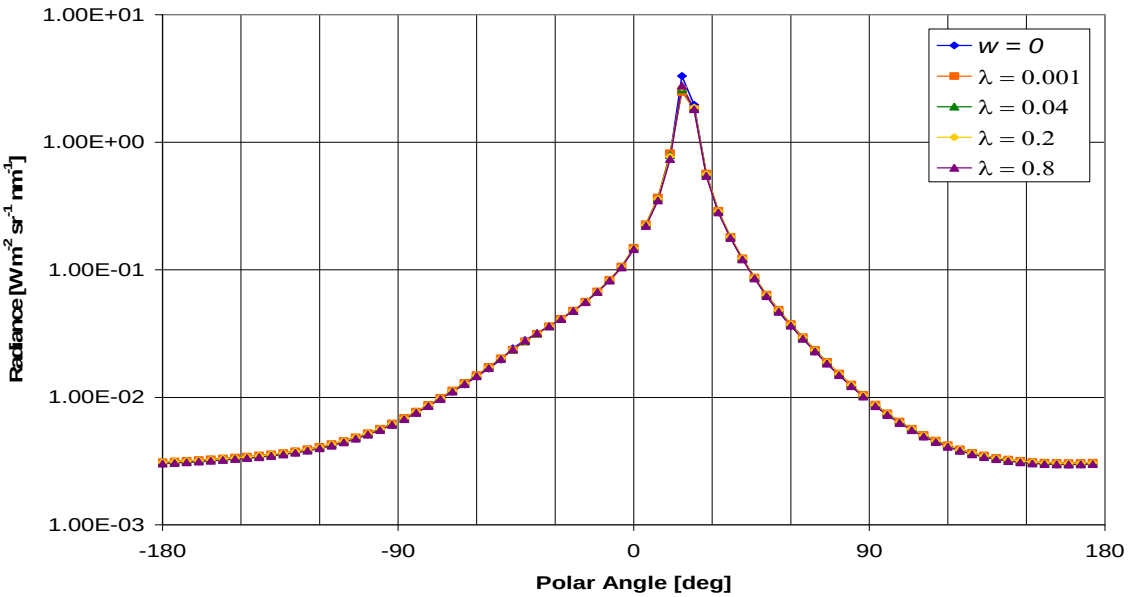

Figure 37 Logarithmic radiance versus polar angle for 460 nm light at multiple K_{max} values, geometric depth z = 50 m. K_{max} values correspond to cut-off wavelengths 0.001, 0.04, 0.2, and 0.8 meters. Solar zenith angle 30 degrees. Wind speed, *w*, of 0 m/s is included as a comparison.

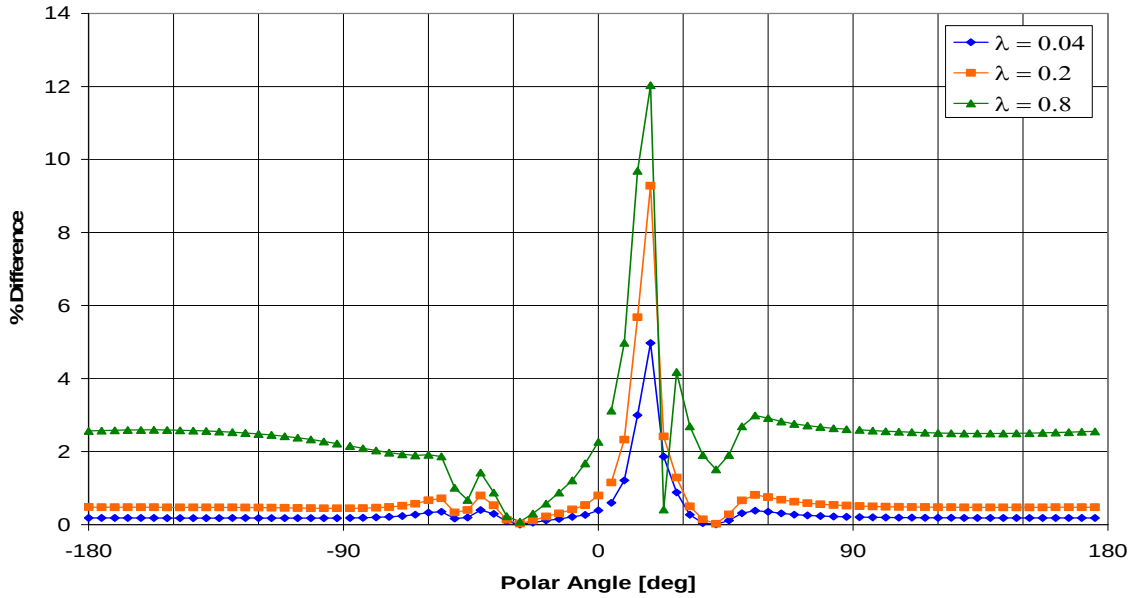

Figure 38 Percent difference versus polar angle for 460 nm light detectors at geometric depth z = 50 m. Percent difference is between longer cut-off wavelengths and the λ = 0.001 case. Solar zenith angle 30 degrees.

Near the sea surface, from geometric depth z = 0 m to z = 50 m, for 460 nm there are peaks in percent difference in the solar beam, around 18 degrees, and also near the critical angle, around 48 degrees and -48 degrees. This pattern is similar to that of the one component water model, however, for the 460 nm case, the peaks near the critical angle are never equal to the peak percent difference in the solar beam. Also, the magnitude of the peaks decreases much more quickly for the 460 nm case, than for the one component water model. For the 460 nm case, by geometric depth z = 50 m, the maximum peak in the solar beam is only 12% and there are no noticeable peaks near the critical angle, whereas for the one component model, the beam peak did not decrease to a maximum of 12% until a geometric depth greater than 300 m.

Figure 39 and Figure 40 show the radiance and percent difference relationships at geometric depths z = 100 m for the 460 nm radiance field. Geometric depth z = 100 m is the first depth of the intermediate region.

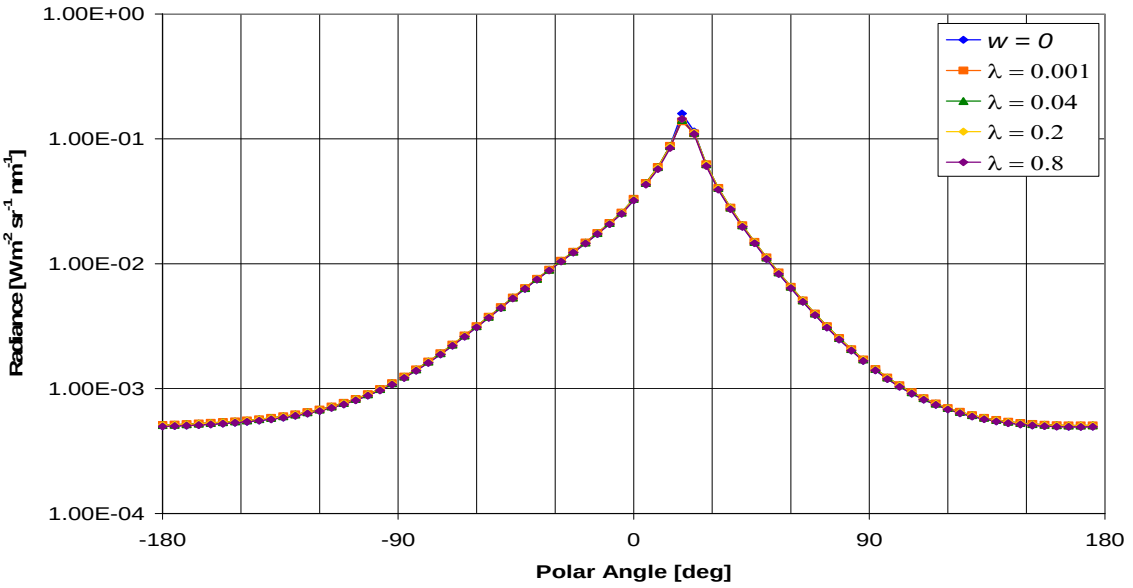

Figure 39 Logarithmic radiance versus polar angle for 460 nm light at multiple K_{max} values, geometric depth z = 100 m. K_{max} values correspond to cut-off wavelengths 0.001, 0.04, 0.2, and 0.8 meters. Solar zenith angle 30 degrees. Wind speed, *w*, of 0 m/s is included as a comparison.

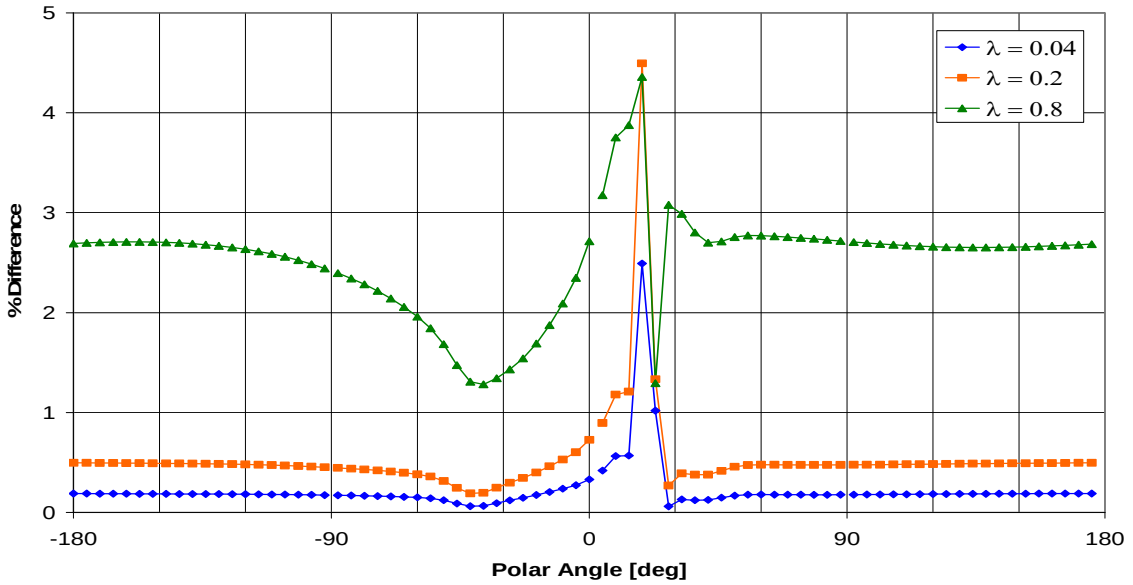

Figure 40 Percent difference versus polar angle for 460 nm light detectors at geometric depth z = 100 m. Percent difference is between longer cut-off wavelengths and the λ = 0.001 case. Solar zenith angle 30 degrees.

Figure 41 and Figure 42 show the radiance and percent difference relationships at geometric depths z = 400 m for the 460 nm radiance field.

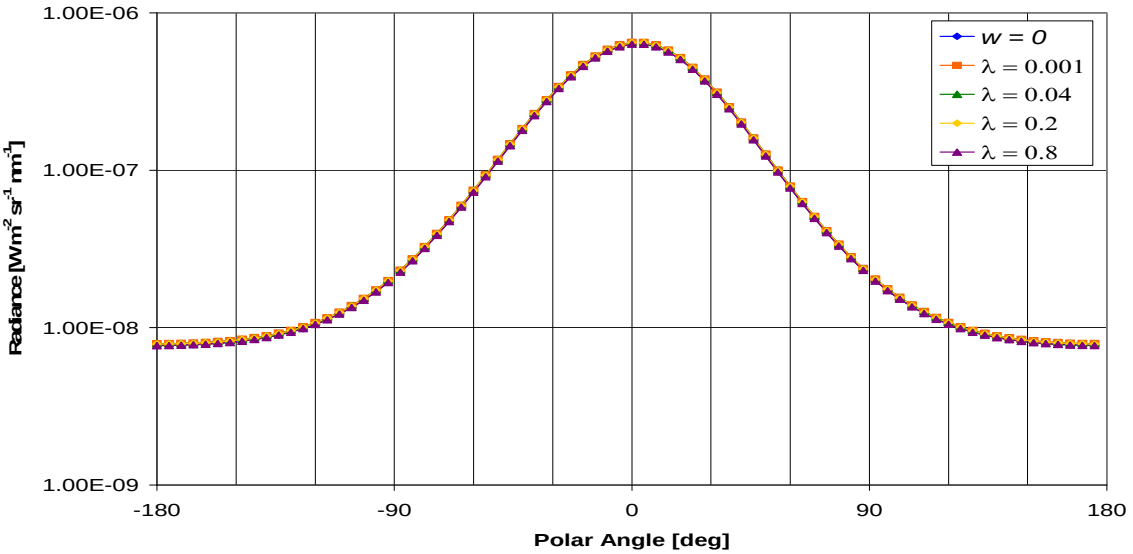

Figure 41 Logarithmic radiance versus polar angle for 460 nm light at multiple K_{max} values, geometric depth z =400 m. K_{max} values correspond to cut-off wavelengths 0.001, 0.04, 0.2, and 0.8 meters. Solar zenith angle 30 degrees. Wind speed, *w*, of 0 m/s is included as a comparison.

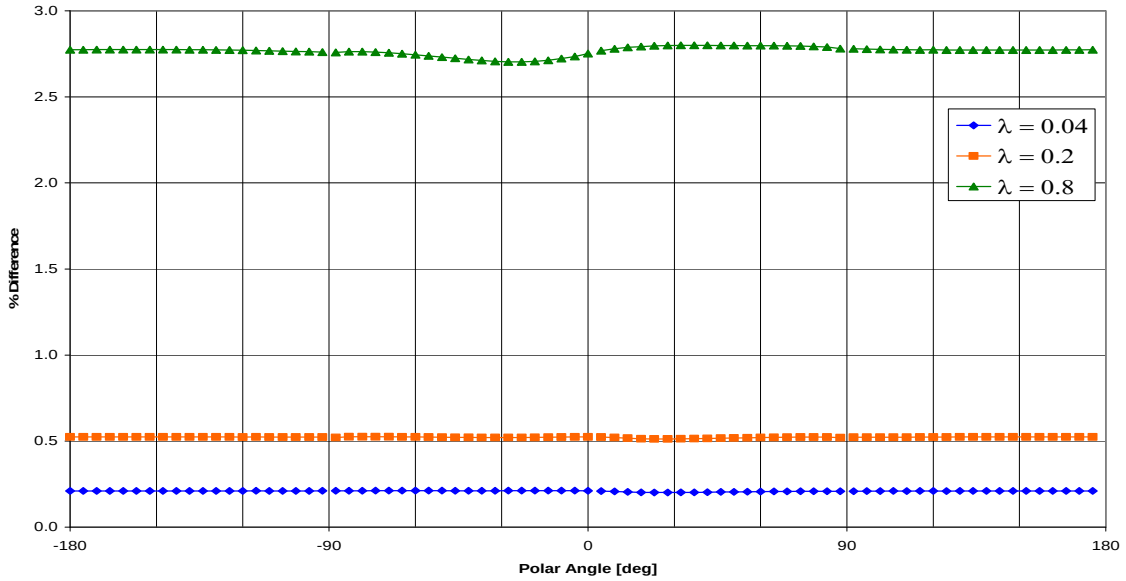

Figure 42 Percent difference versus polar angle for 460 nm light detectors at geometric depth z = 400 m. Percent difference is between longer cut-off wavelengths and the λ = 0.001 case. Solar zenith angle 30 degrees.

Figure 43 and Figure 44 show the radiance and percent difference relationships at geometric depths z = 700 m for the 460 nm radiance field.

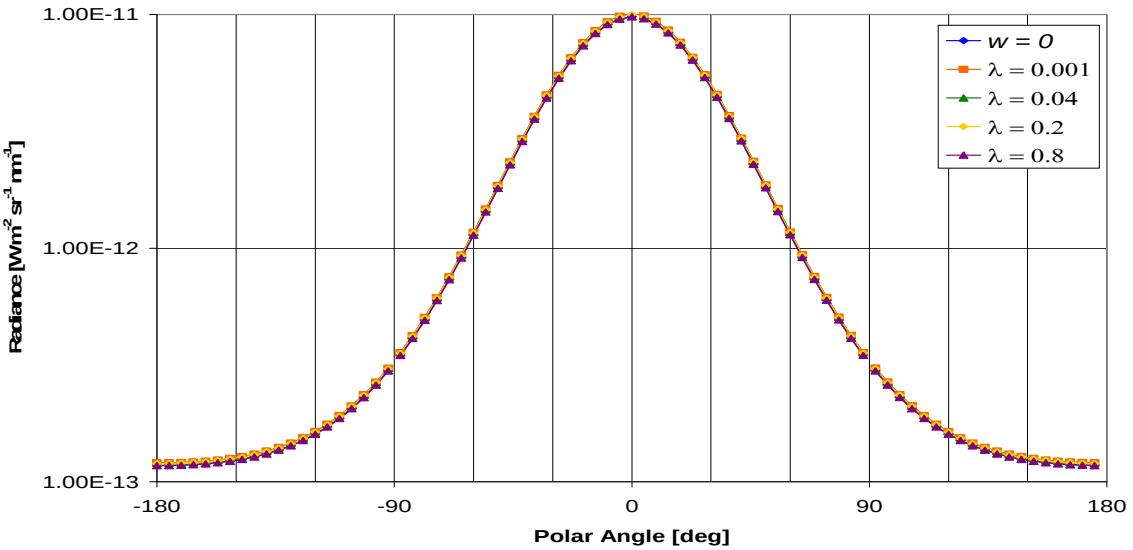

Figure 43 Logarithmic radiance versus polar angle for 460 nm light at multiple K_{max} values, geometric depth z = 700 m. K_{max} values correspond to cut-off wavelengths 0.001, 0.04, 0.2, and 0.8 meters. Solar zenith angle 30 degrees. Wind speed, *w*, of 0 m/s is included as a comparison.

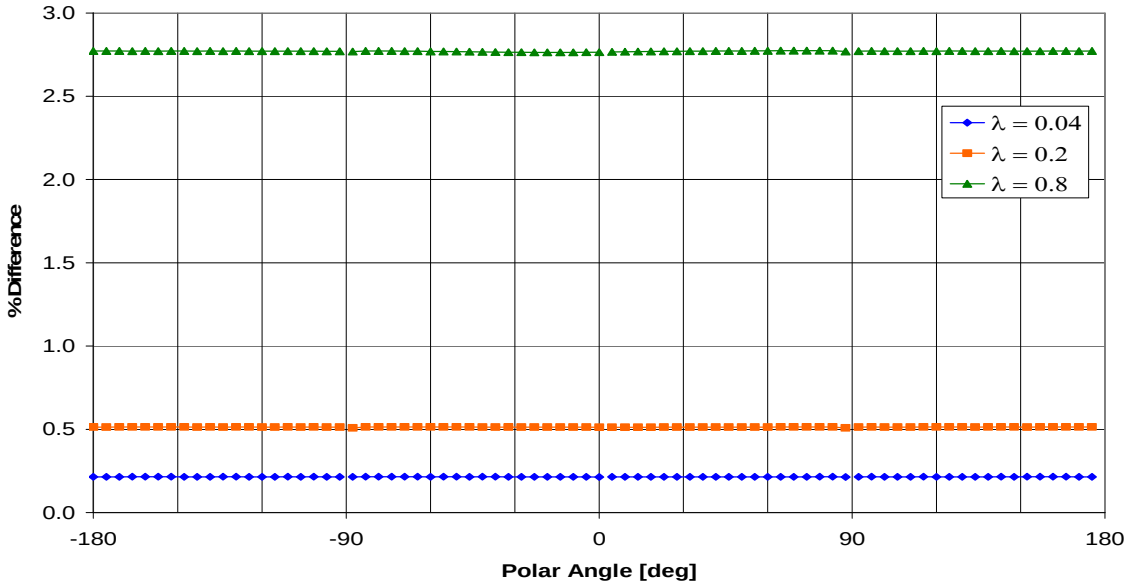

Figure 44 Percent Percent difference versus polar angle for 460 nm light detectors at geometric depth z = 700 m. Percent difference is between longer cut-off wavelengths and the λ = 0.001 case. Solar zenith angle 30 degrees.

In the intermediate region, for the 460 nm radiance field, the peak in percent difference decreases rapidly and then disappears all together. At geometric depth z = 700 nm, the percent difference curves are nearly constant for each cutoff wavelength. Although cutoff wavelength λ = 0.2 m is five time greater than cutoff wavelength λ = 0.04 m, the percent difference for λ = 0.2 m is only marginally larger than that of λ = 0.04 m. However, cutoff wavelength λ = 0.8 is four times greater than cutoff wavelength λ = 0.2 m, and the percent difference for λ = 0.8 is more than five times greater than that of cutoff wavelength λ = 0.2 m.

Figure 45 and Figure 46 show the radiance and percent difference relationships at geometric depths z = 800 m for the 460 nm radiance field. Geometric depth z = 800 m is the first depth in the asymptotic region.

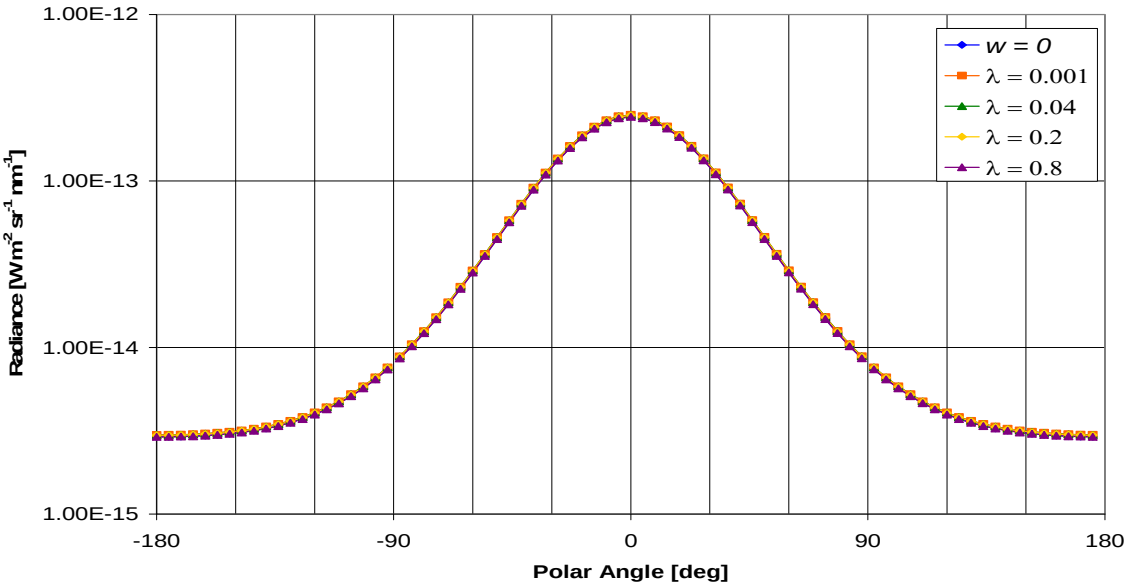

Figure 45 Logarithmic radiance versus polar angle for 460 nm light at multiple K_{max} values, geometric depth z =800 m. K_{max} values correspond to cut-off wavelengths 0.001, 0.04, 0.2, and 0.8 meters. Solar zenith angle 30 degrees. Wind speed, *w*, of 0 m/s is included as a comparison.

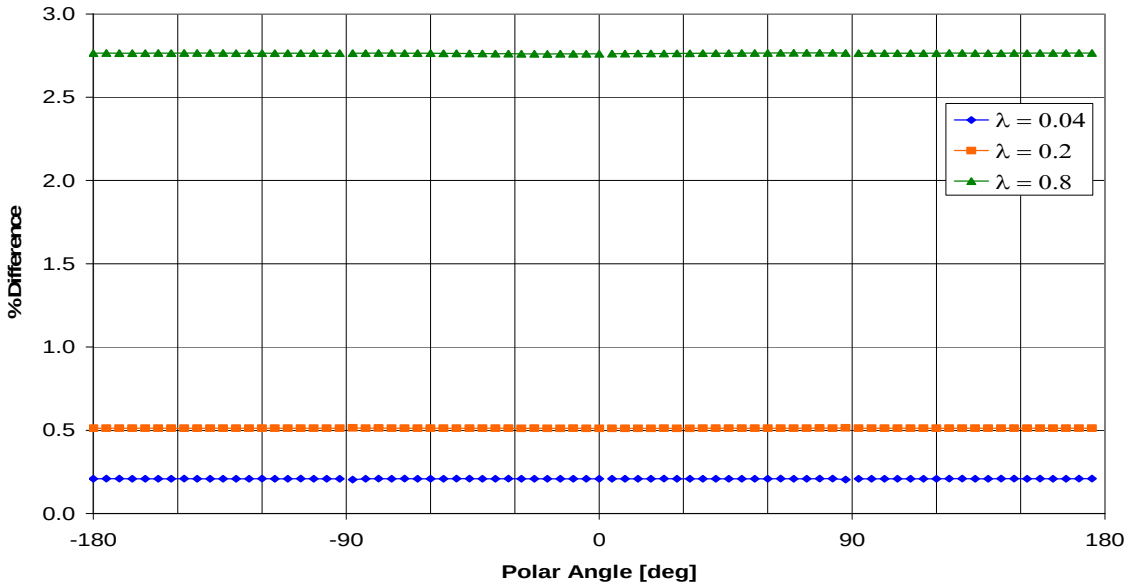

Figure 46 Percent difference versus polar angle for 460 nm light detectors at geometric depth z = 800 m. Percent difference is between longer cut-off wavelengths and the λ = 0.001 case. Solar zenith angle 30 degrees.

Figure 47 and Figure 48 show the radiance and percent difference relationships at geometric depths z = 900 m for the 460 nm radiance field.

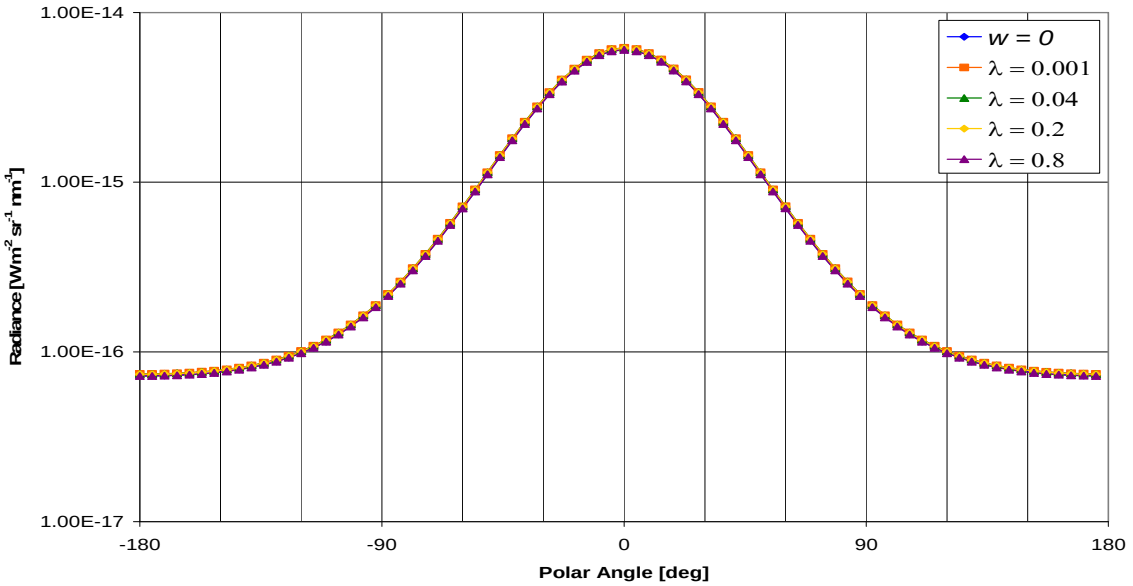

Figure 47 Logarithmic radiance versus polar angle for 460 nm light at multiple K_{max} values, geometric depth z = 900 m. K_{max} values correspond to cut-off wavelengths 0.001, 0.04, 0.2, and 0.8 meters. Solar zenith angle 30 degrees. Wind speed, *w*, of 0 m/s is included as a comparison.

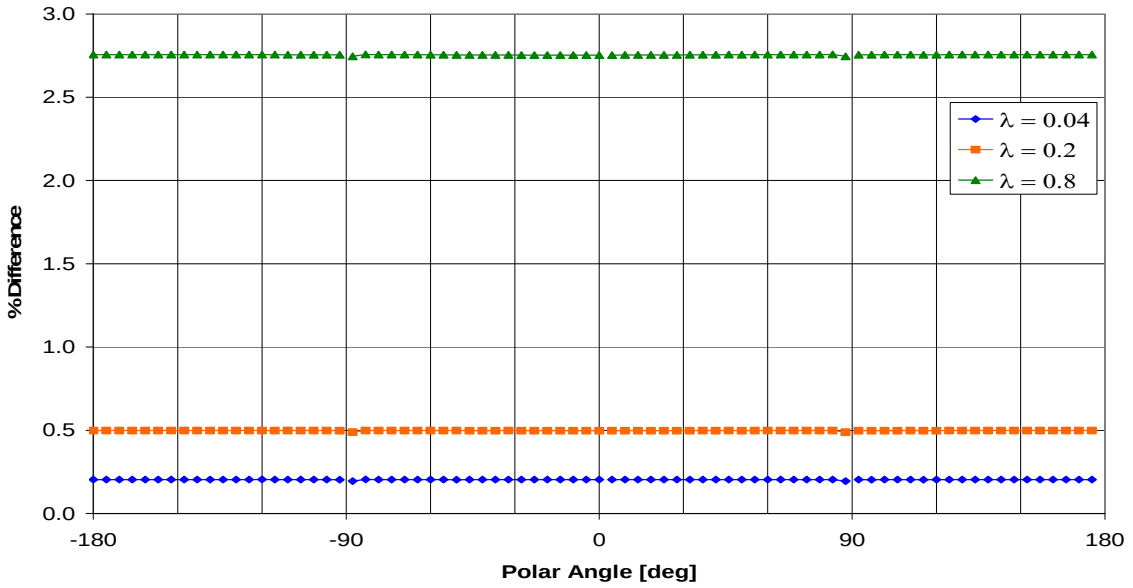

Figure 48 Percent difference versus polar angle for 460 nm light detectors at geometric depth z = 900 m. Percent difference is between longer cut-off wavelengths and the λ = 0.001 case. Solar zenith angle 30 degrees.

In the asymptotic region, the percent difference curves for the 460 nm radiance field continue to be constant. Overall, for the 460 nm radiance field, the effect of changing the mean square slope is large just below the surface. The effect decrease rapidly through geometric depth z = 50, below which, in the intermediate region, the effect gradually moves to a constant percent difference for each of the cutoff wavelengths. Once in the asymptotic region, the effect of changing the mean square slope remains constant for all polar angle values, and with increasing depth. Since the simulation stopped at maximum geometric depth z = 1000 m, there is no data below the asymptotic region.

5.3.2 520 nm

As with the 460 nm radiance field, the effect of changing the mean square slope will be determined near the surface, in the intermediate region, in the asymptotic region and below the asymptotic region. For wavelength 520 nm, the asymptotic region lies between geometric depths z = 500 m and z = 800 m. Figure 49 and Figure 50 show the

radiance and percent difference relationships at geometric depths z = 0 m for the 520 nm radiance field.

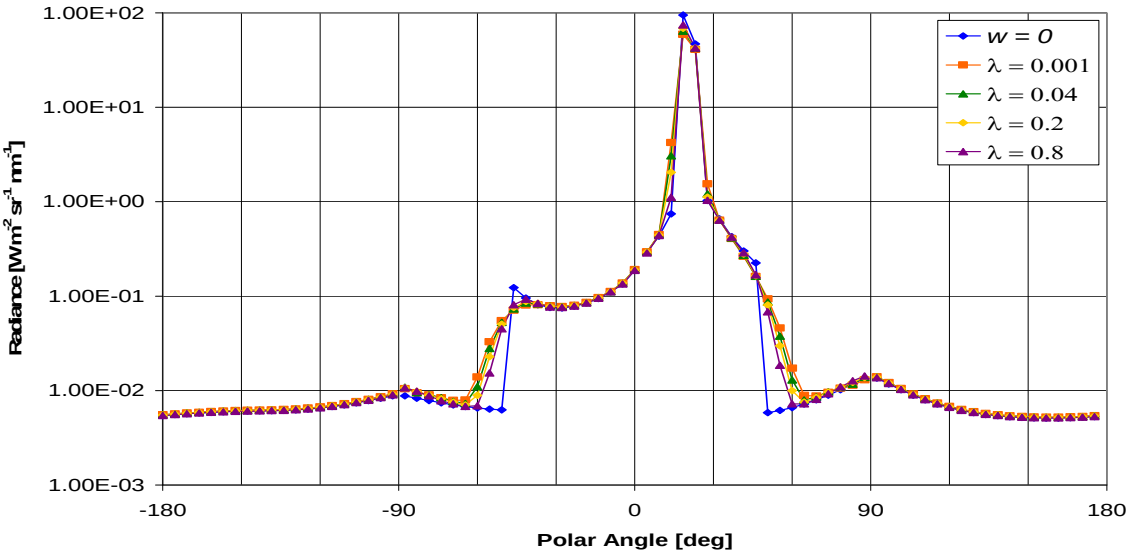

Figure 49 Logarithmic radiance versus polar angle for 520 nm light at multiple K_{max} values, geometric depth z = 0 m. K_{max} values correspond to cut-off wavelengths 0.001, 0.04, 0.2, and 0.8 meters. Solar zenith angle 30 degrees. Wind speed, *w*, of 0 m/s is included as a comparison.

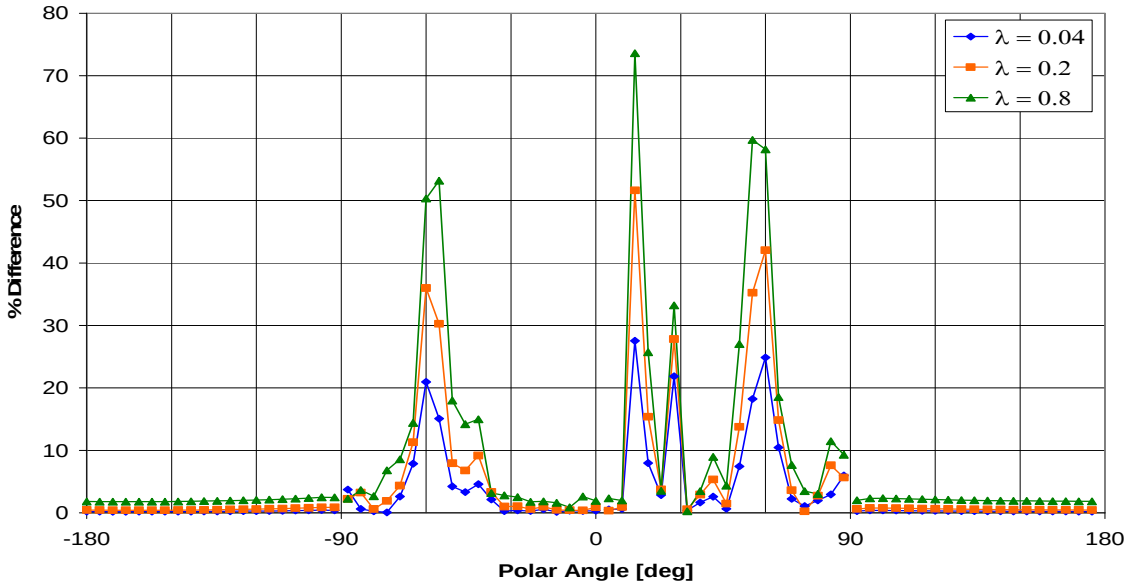

Figure 50 Percent difference versus polar angle for 520 nm light detectors at geometric depth z = 0 m. Percent difference is between longer cut-off wavelengths and the λ = 0.001 case. Solar zenith angle 30 degrees.

Figure 51 and Figure 52 show the radiance and percent difference relationships at geometric depths z = 10 m for the 520 nm radiance field.

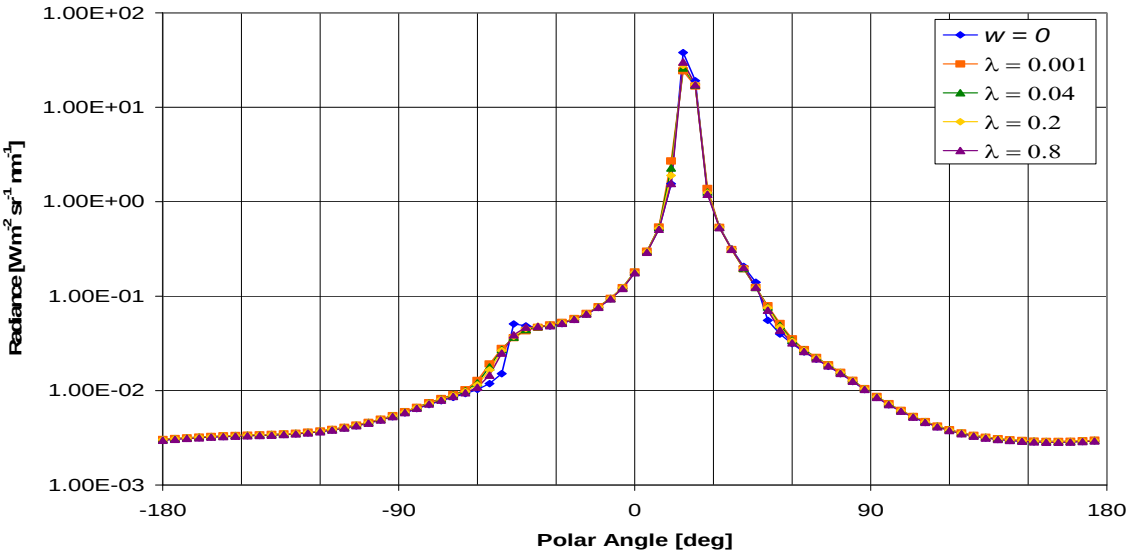

Figure 51 Logarithmic radiance versus polar angle for 520 nm light at multiple K_{max} values, geometric depth z = 10 m. K_{max} values correspond to cut-off wavelengths 0.001, 0.04, 0.2, and 0.8 meters. Solar zenith angle 30 degrees. Wind speed, *w*, of 0 m/s is included as a comparison.

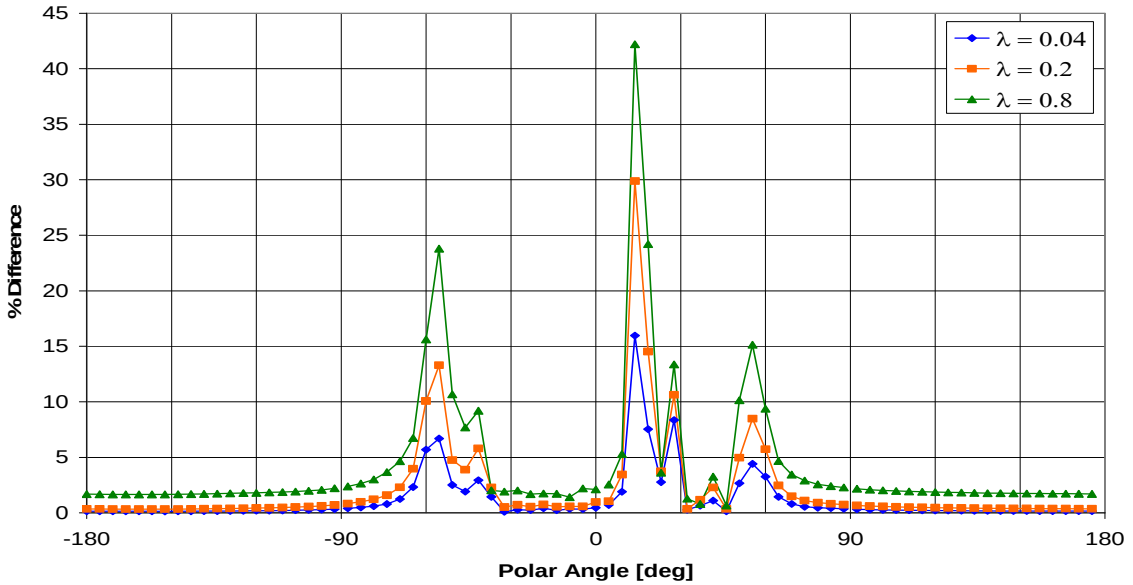

Figure 52 Percent difference versus polar angle for 520 nm light detectors at geometric depth z = 10 m. Percent difference is between longer cut-off wavelengths and the λ = 0.001 case. Solar zenith angle 30 degrees.

Figure 53 and Figure 54 show the radiance and percent difference relationships at geometric depths z = 30 m for the 520 nm radiance field.

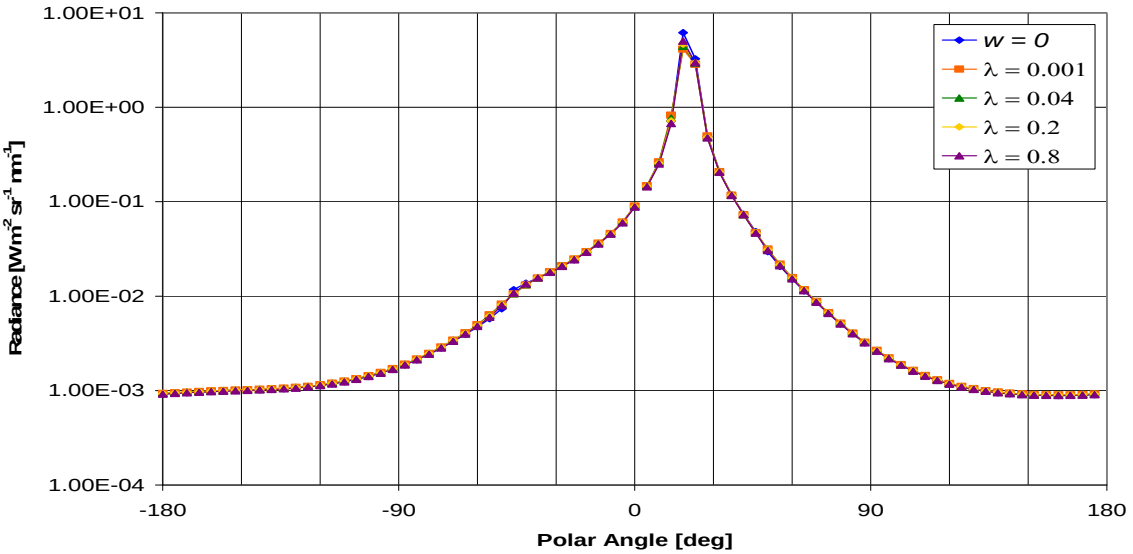

Figure 53 Logarithmic radiance versus polar angle for 520 nm light at multiple K_{max} values, geometric depth z = 30 m. K_{max} values correspond to cut-off wavelengths 0.001, 0.04, 0.2, and 0.8 meters. Solar zenith angle 30 degrees. Wind speed, *w*, of 0 m/s is included as a comparison

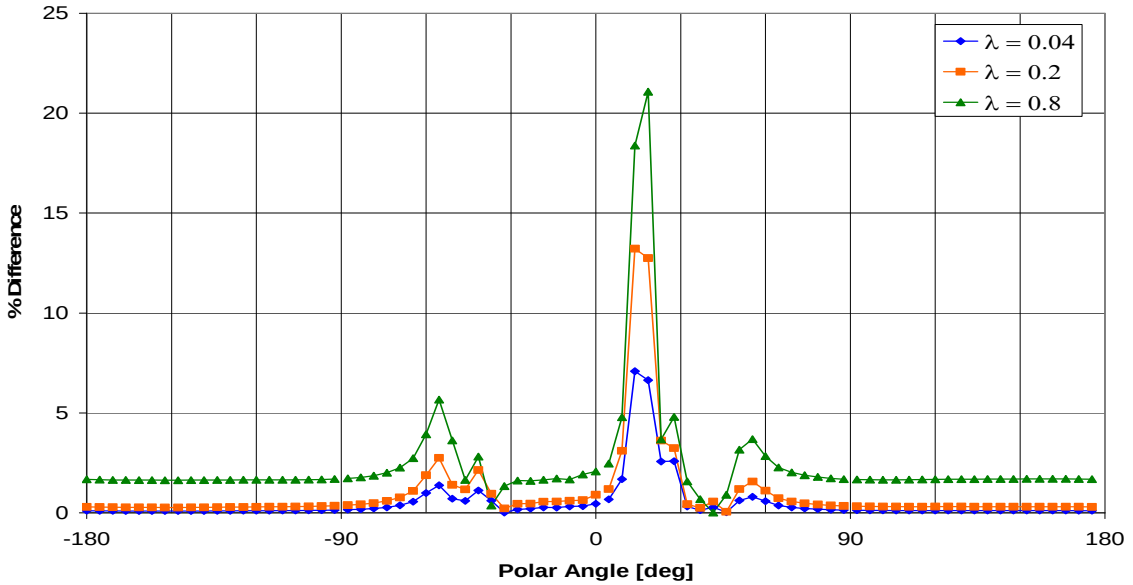

Figure 54 Percent difference versus polar angle for 520 nm light detectors at geometric depth z = 30 m. Percent difference is between longer cut-off wavelengths and the λ = 0.001 case. Solar zenith angle 30 degrees.

Figure 55 and Figure 56 show the radiance and percent difference relationships at geometric depths z = 50 m for the 520 nm radiance field.

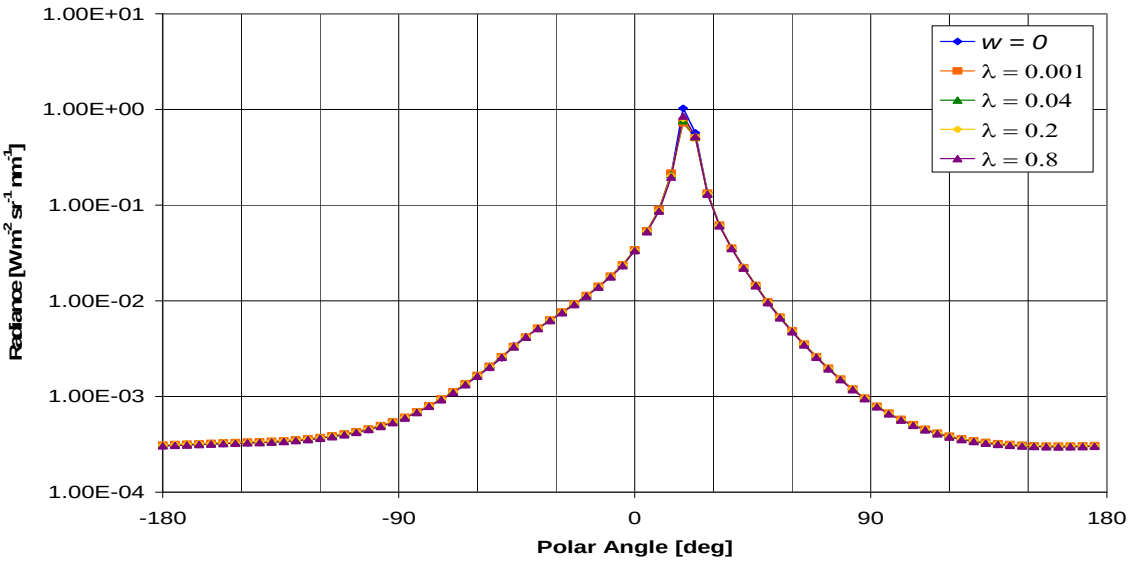

Figure 55 Logarithmic radiance versus polar angle for 520 nm light at multiple K_{max} values, geometric depth z = 50 m. K_{max} values correspond to cut-off wavelengths 0.001, 0.04, 0.2, and 0.8 meters. Solar zenith angle 30 degrees. Wind speed, *w*, of 0 m/s is included as a comparison

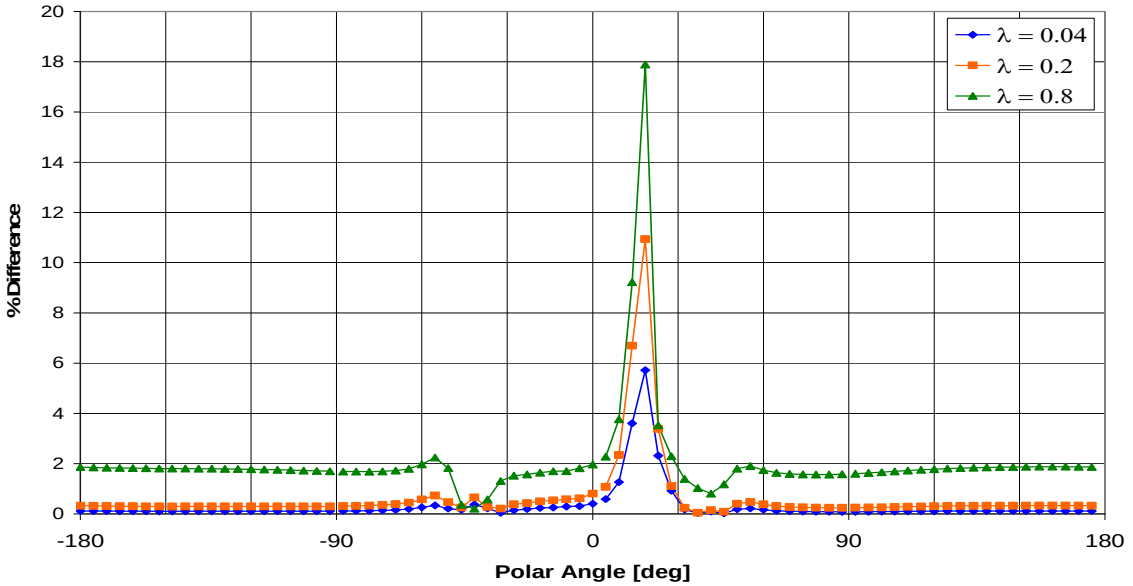

Figure 56 Percent difference versus polar angle for 520 nm light detectors at geometric depth z = 50 m. Percent difference is between longer cut-off wavelengths and the λ = 0.001 case. Solar zenith angle 30 degrees.

For the 520 nm case, as with the 460 nm radiance field, the peaks in percent difference just below the sea surface are located in the solar beam and also near the critical angle. Also, as in the 460 nm case, the three peaks are not of equal magnitude. Through the relatively short distance of 50 m, the peaks in percent difference decrease significantly, and the peaks near the critical angle nearly disappear.

Figure 57 and Figure 58 show the radiance and percent difference relationships at geometric depths z = 100 m for the 520 nm radiance field. Geometric depth z = 100 m is the beginning of the intermediate region.

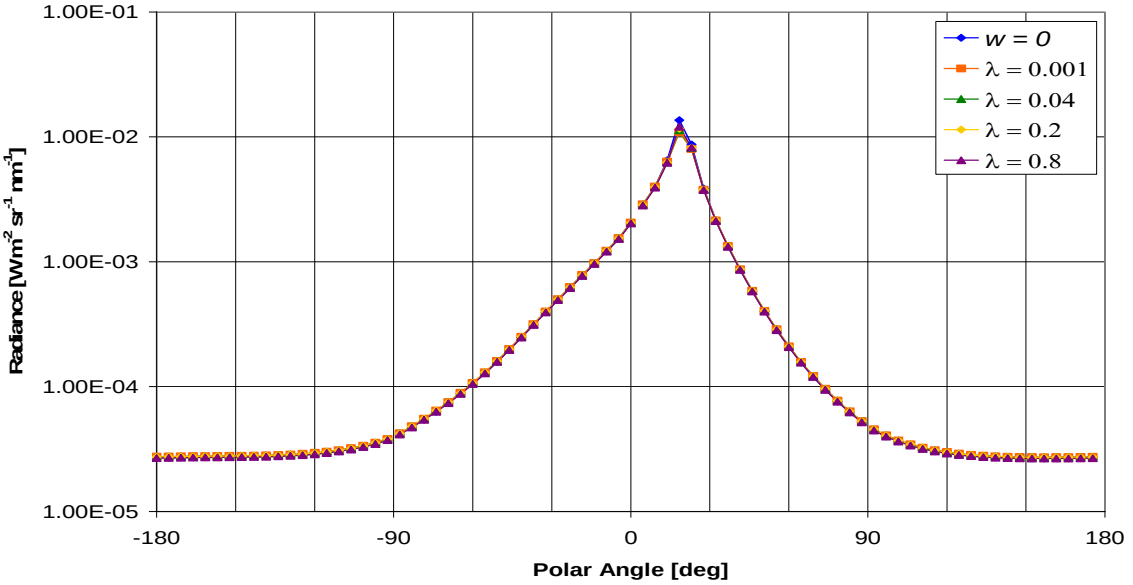

Figure 57 Logarithmic radiance versus polar angle for 520 nm light at multiple K_{max} values, geometric depth z = 100 m. K_{max} values correspond to cut-off wavelengths 0.001, 0.04, 0.2, and 0.8 meters. Solar zenith angle 30 degrees. Wind speed, *w*, of 0 m/s is included as a comparison

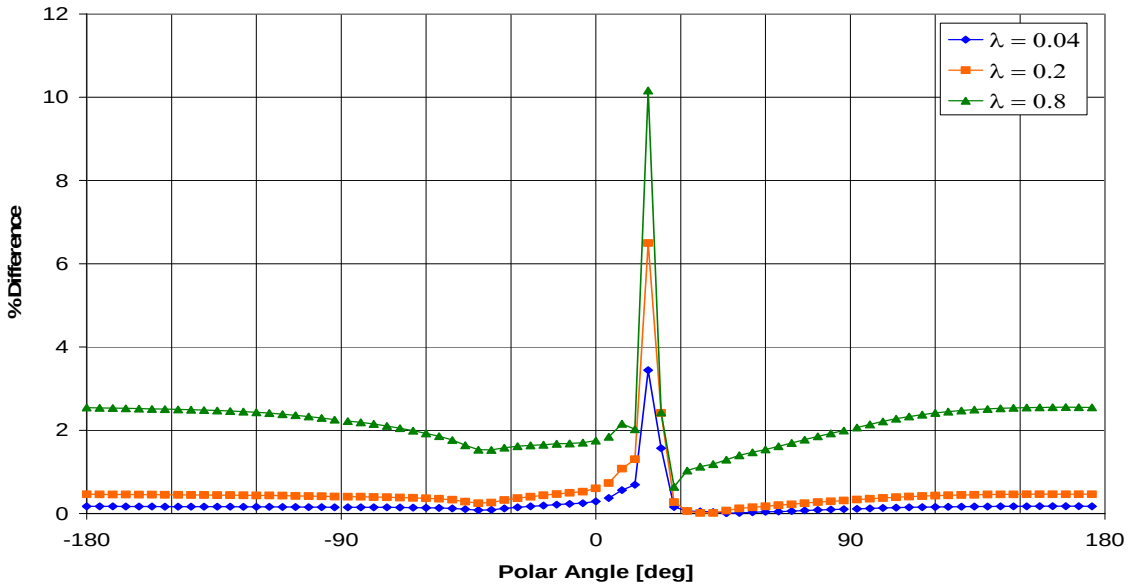

Figure 58 Percent difference versus polar angle for 520 nm light detectors at geometric depth z = 100 m. Percent difference is between longer cut-off wavelengths and the λ = 0.001 case. Solar zenith angle 30 degrees.

Figure 59 and Figure 60 show the radiance and percent difference relationships at geometric depths z = 300 m for the 520 nm radiance field.

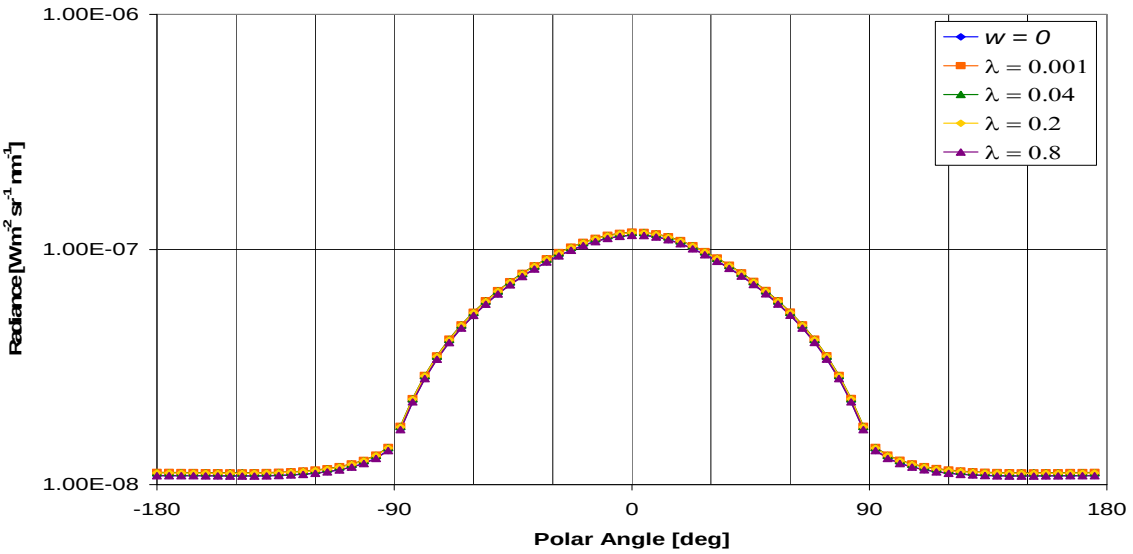

Figure 59 Logarithmic radiance versus polar angle for 520 nm light at multiple K_{max} values, geometric depth z = 300 m. K_{max} values correspond to cut-off wavelengths 0.001, 0.04, 0.2, and 0.8 meters. Solar zenith angle 30 degrees. Wind speed, *w*, of 0 m/s is included as a comparison

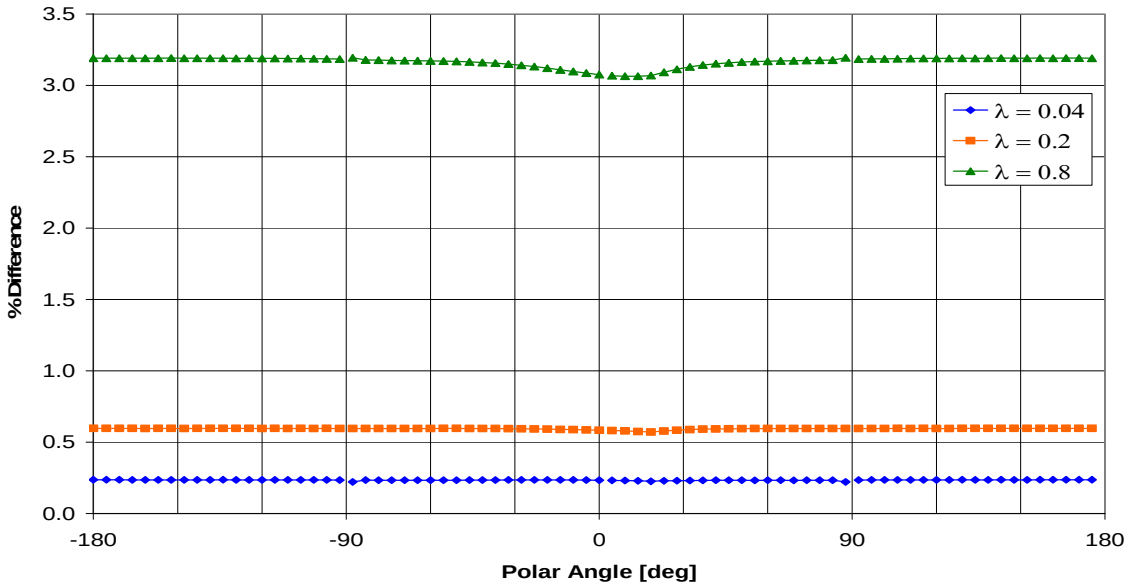

Figure 60 Percent difference versus polar angle for 520 nm light detectors at geometric depth z = 300 m. Percent difference is between longer cut-off wavelengths and the λ = 0.001 case. Solar zenith angle 30 degrees.

In the intermediate region, as with the 460 nm radiance field, the peaks in percent difference disappear gradually, until the percent difference curves are nearly constant. The values of the percent difference curves are slightly greater in magnitude for the 520 nm radiance field than for the 460 nm radiance field.

Figure 61 and Figure 62 show the radiance and percent difference relationships at geometric depths z = 500 m for the 520 nm radiance field. Geometric depth z = 500 m is the beginning of the asymptotic region.

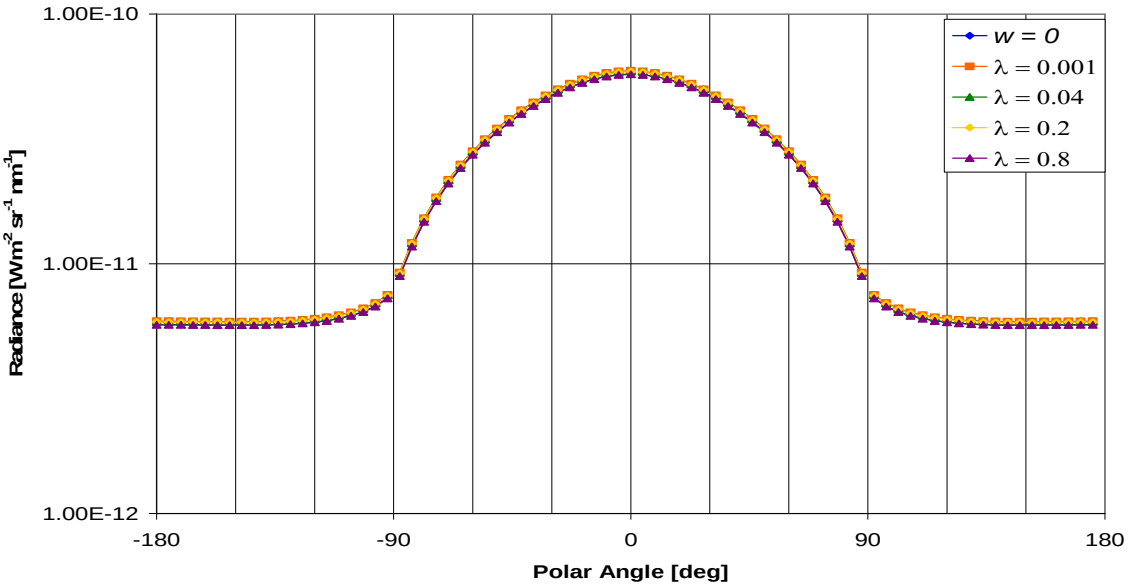

Figure 61 Logarithmic radiance versus polar angle for 520 nm light at multiple K_{max} values, geometric depth z = 500 m. K_{max} values correspond to cut-off wavelengths 0.001, 0.04, 0.2, and 0.8 meters. Solar zenith angle 30 degrees. Wind speed, *w*, of 0 m/s is included as a comparison

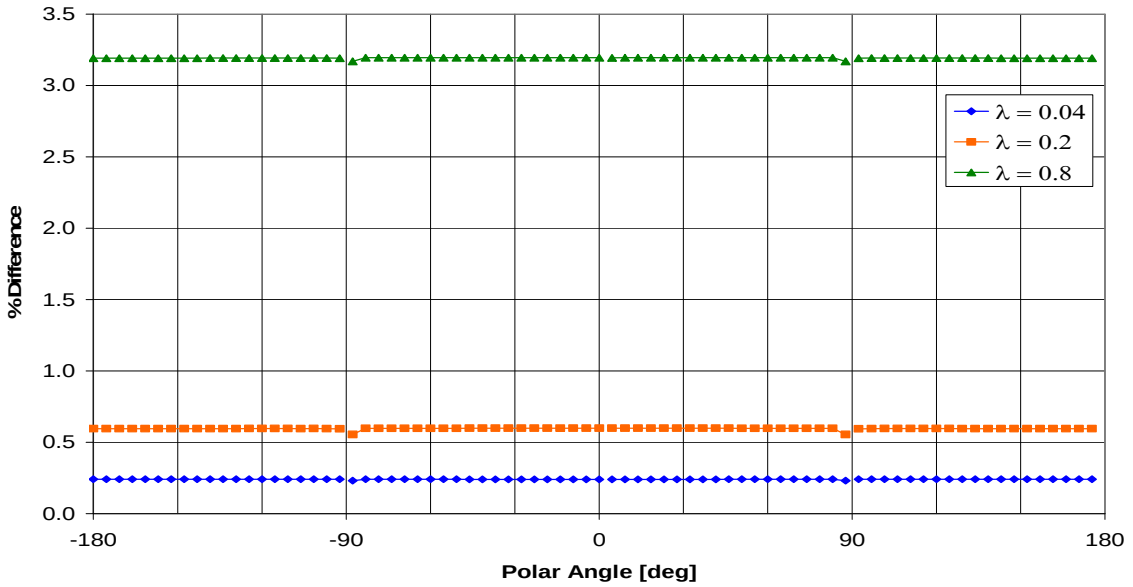

Figure 62 Percent difference versus polar angle for 520 nm light detectors at geometric depth z = 500 m. Percent difference is between longer cut-off wavelengths and the λ = 0.001 case. Solar zenith angle 30 degrees.

Figure 63 and Figure 64 show the radiance and percent difference relationships at geometric depths z = 700 m for the 520 nm radiance field.

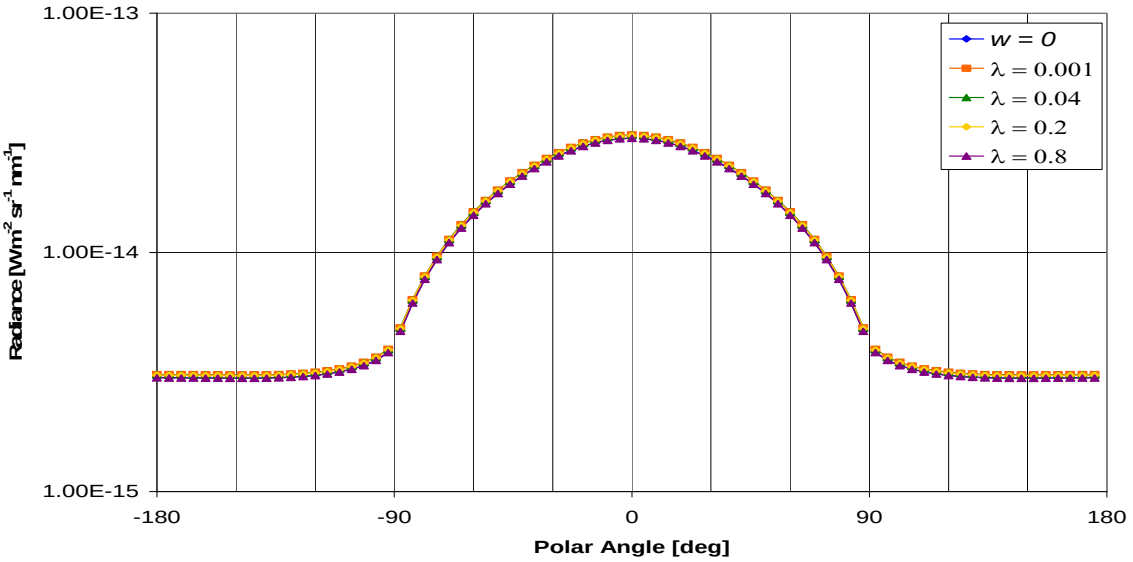

Figure 63 Logarithmic radiance versus polar angle for 520 nm light at multiple K_{max} values, geometric depth z = 700 m. K_{max} values correspond to cut-off wavelengths 0.001, 0.04, 0.2, and 0.8 meters. Solar zenith angle 30 degrees. Wind speed, *w*, of 0 m/s is included as a comparison

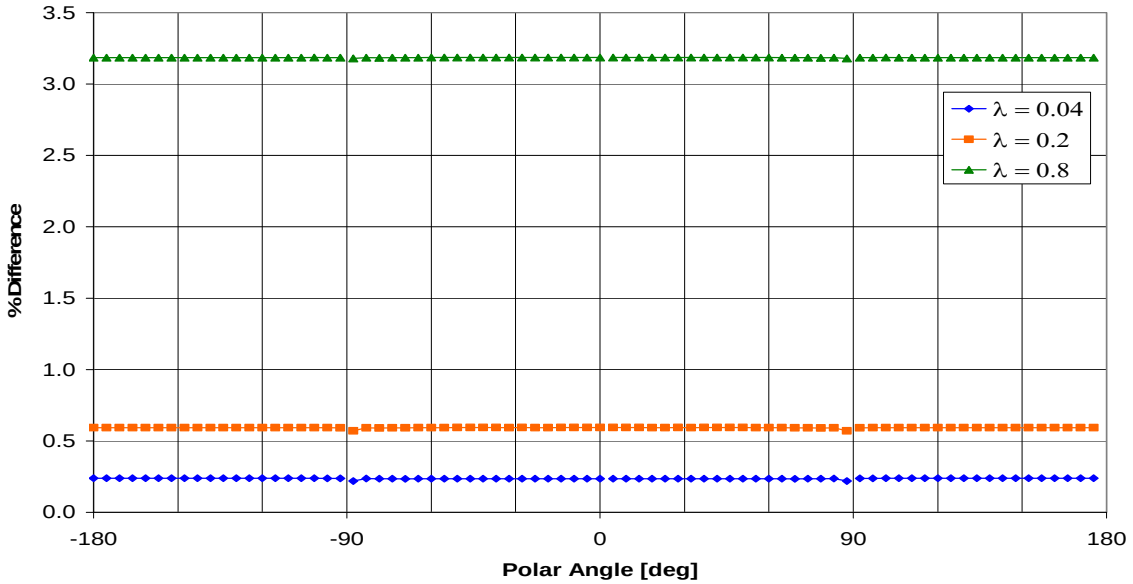

Figure 64 Percent difference versus polar angle for 520 nm light detectors at geometric depth z =700 m. Percent difference is between longer cut-off wavelengths and the λ = 0.001 case. Solar zenith angle 30 degrees.

In the asymptotic region, the percent difference curves are constants for all polar angle values for each of the cutoff wavelengths. It is also interesting to note the difference in shape of the radiance curves in the asymptotic region between the 460 nm case and the 520 nm case. This shape difference was discussed in Chapter III, but it is shown much more clearly in this section.

Figure 65 and Figure 66 show the radiance and percent difference relationships at geometric depths z = 900 m for the 520 nm radiance field. Geometric depth z = 900 m is below the asymptotic region.

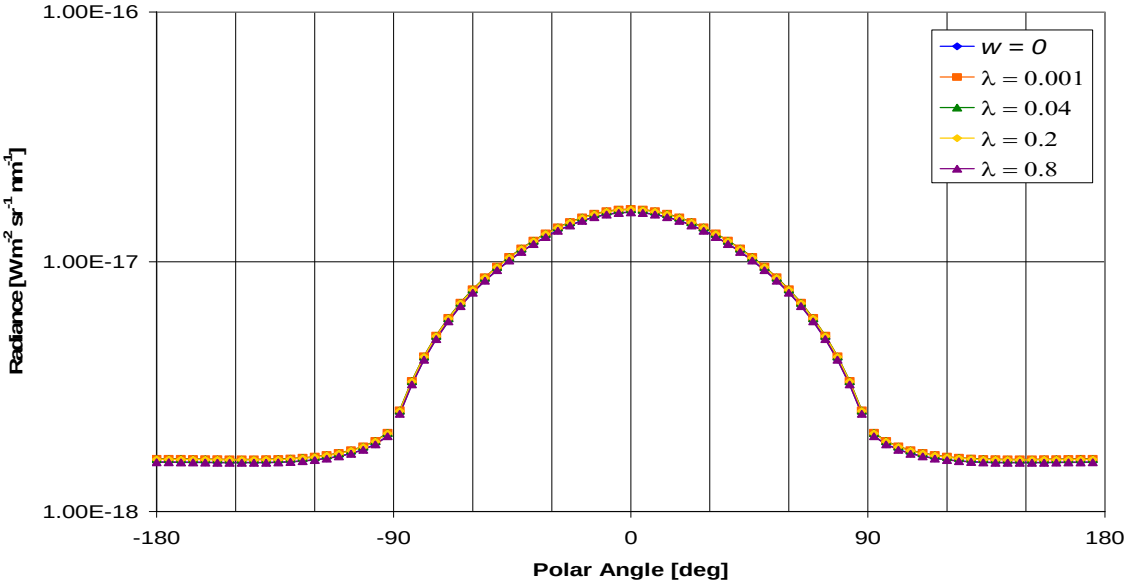

Figure 65 Logarithmic radiance versus polar angle for 520 nm light at multiple K_{max} values, geometric depth z = 900 m. K_{max} values correspond to cut-off wavelengths 0.001, 0.04, 0.2, and 0.8 meters. Solar zenith angle 30 degrees. Wind speed, *w*, of 0 m/s is included as a comparison

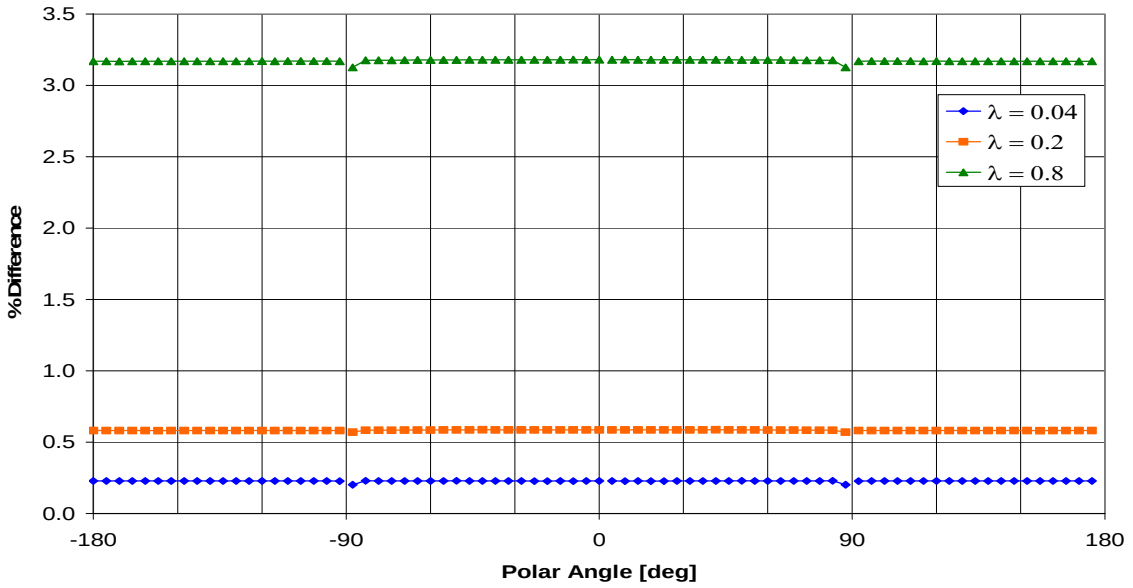

Figure 66 Percent difference versus polar angle for 520 nm light detectors at geometric depth z = 900 m. Percent difference is between longer cut-off wavelengths and the λ = 0.001 case. Solar zenith angle 30 degrees.

Just below the asymptotic region, the radiance curves and percent difference curves do not differ noticeably from those of the asymptotic region. Overall, the trend shown by the 460 nm radiance field is repeated here with the 520 nm radiance field. The effect of changing the mean square slope is greatest at shallower depths, near the surface, and for polar angles within the solar beam and also near the critical angle. The effect of changing the mean square slope decreases with increasing depth. Also, the effect decreases faster near the critical angle than in the solar beam region. Once the radiance field reaches the asymptotic region, the percent difference curves remain constant for all polar angle values, even with increasing depth.

5.3.3 580 nm

The asymptotic region for the 580 nm radiance field, with Raman scattering included, is from geometric depths z = 500 m to z = 900 m. Figure 67 and Figure 68 show the radiance and percent difference relationships at geometric depths z = 0 m for the 580 nm radiance field.

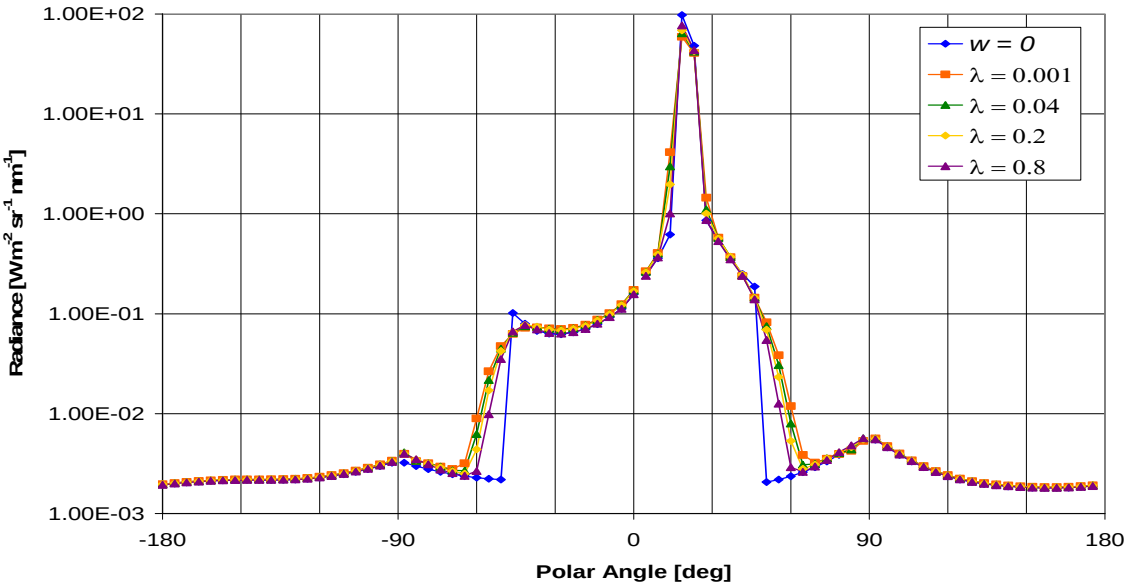

Figure 67 Logarithmic radiance versus polar angle for 580 nm light at multiple K_{max} values, geometric depth z = 0 m. K_{max} values correspond to cut-off wavelengths 0.001, 0.04, 0.2, and 0.8 meters. Solar zenith angle 30 degrees. Wind speed, *w*, of 0 m/s is included as a comparison

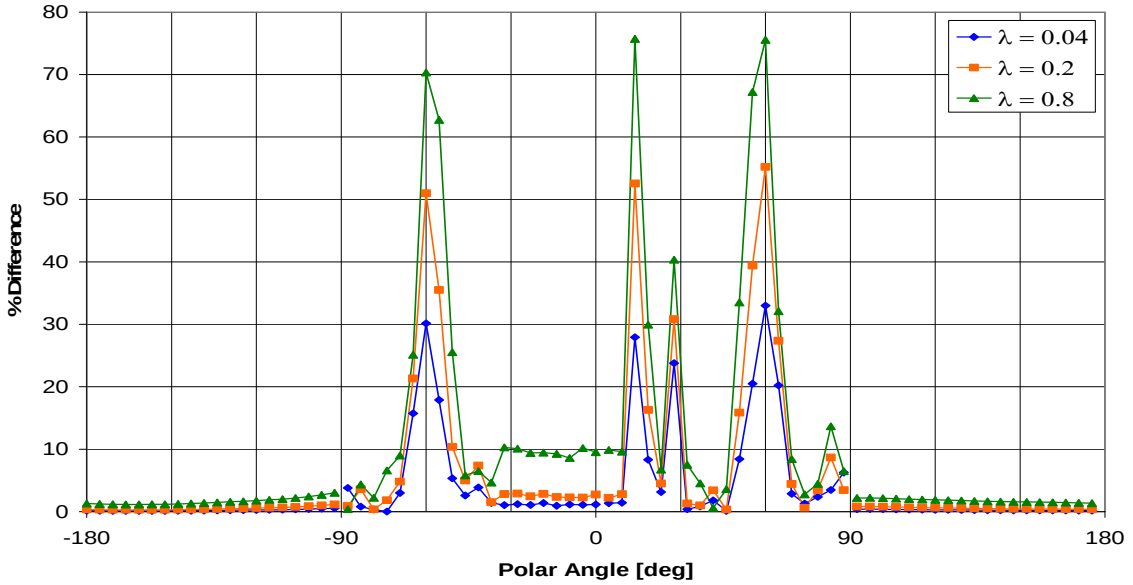

Figure 68 Percent difference versus polar angle for 580 nm light detectors at geometric depth z = 0 m. Percent difference is between longer cut-off wavelengths and the λ = 0.001 case. Solar zenith angle 30 degrees.

Figure 69 and Figure 70 show the radiance and percent difference relationships at geometric depths z = 10 m for the 580 nm radiance field.

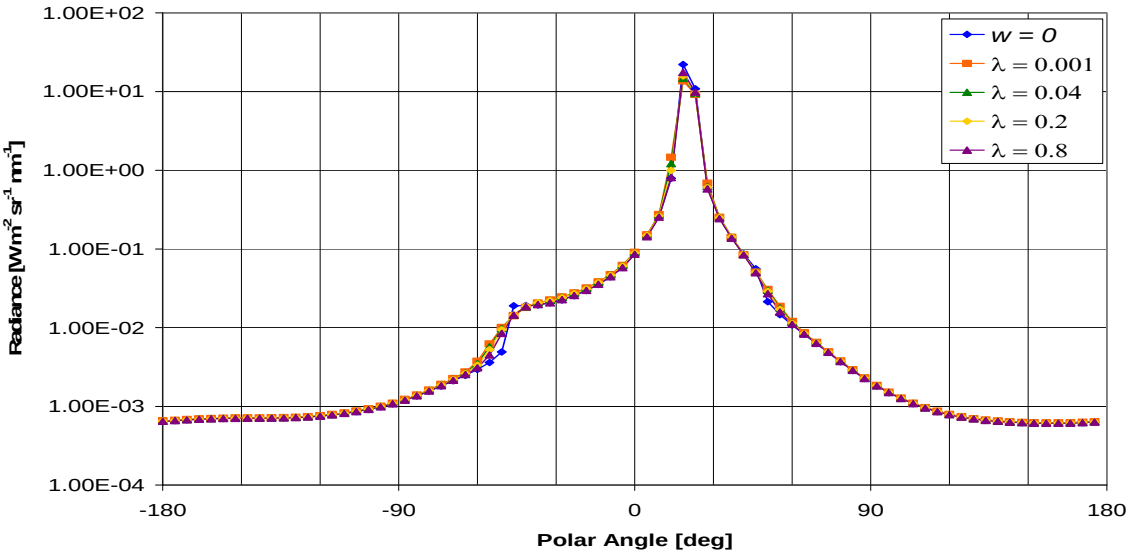

Figure 69 Logarithmic radiance versus polar angle for 580 nm light at multiple K_{max} values, geometric depth z = 10 m. K_{max} values correspond to cut-off wavelengths 0.001, 0.04, 0.2, and 0.8 meters. Solar zenith angle 30 degrees. Wind speed, *w*, of 0 m/s is included as a comparison

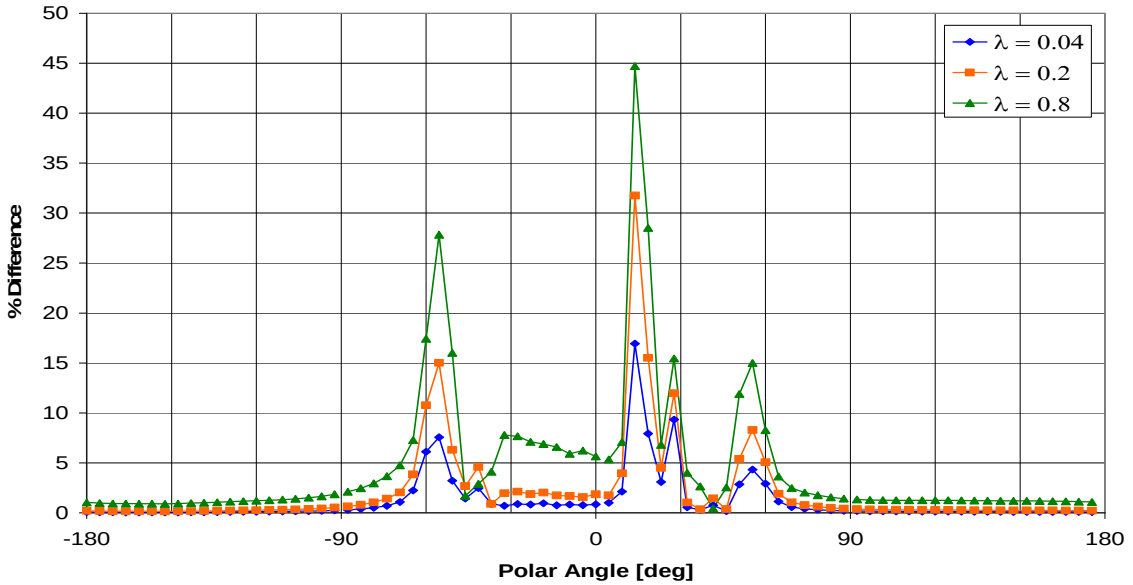

Figure 70 Percent difference versus polar angle for 580 nm light detectors at geometric depth z = 10 m. Percent difference is between longer cut-off wavelengths and the λ = 0.001 case. Solar zenith angle 30 degrees.

Figure 71 and Figure 72 show the radiance and percent difference relationships at geometric depths z = 30 m for the 580 nm radiance field.

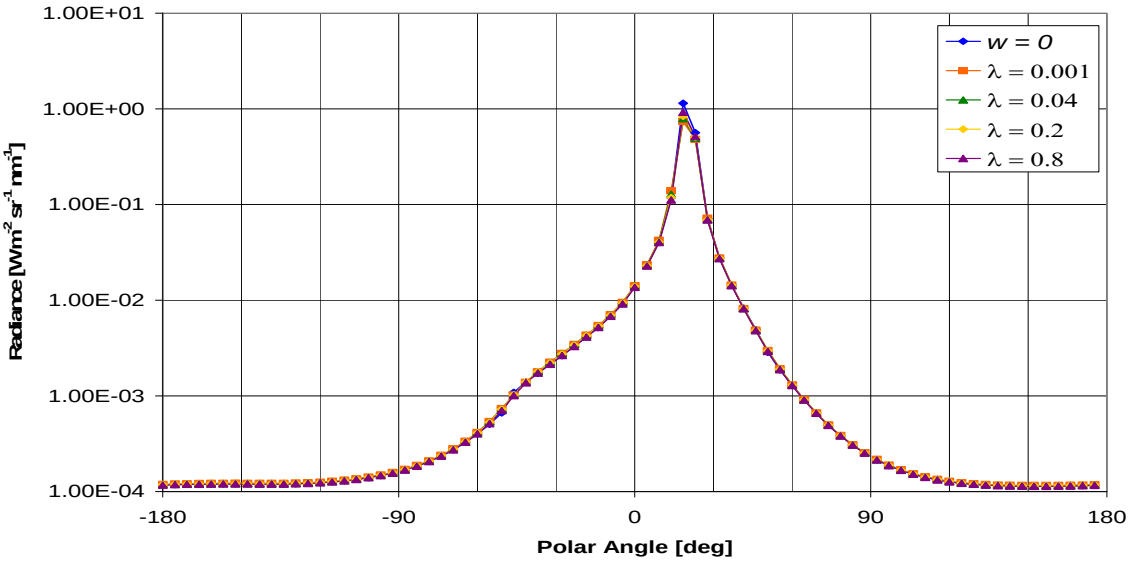

Figure 71 Logarithmic radiance versus polar angle for 580 nm light at multiple K_{max} values, geometric depth z = 30 m. K_{max} values correspond to cut-off wavelengths 0.001, 0.04, 0.2, and 0.8 meters. Solar zenith angle 30 degrees. Wind speed, *w*, of 0 m/s is included as a comparison

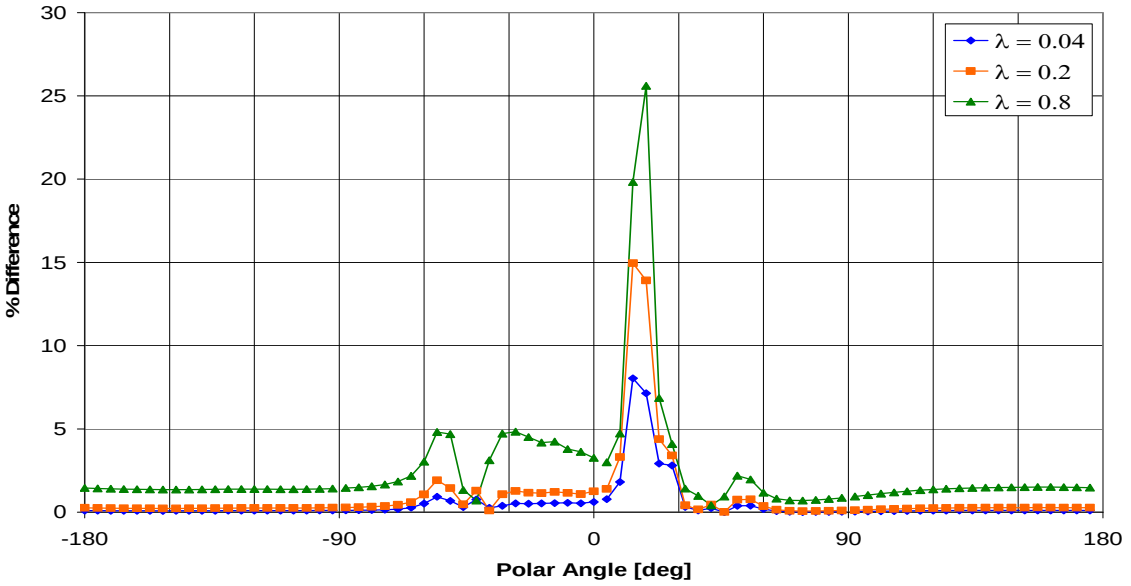

Figure 72 Percent difference versus polar angle for 580 nm light detectors at geometric depth z = 30 m. Percent difference is between longer cut-off wavelengths and the λ = 0.001 case. Solar zenith angle 30 degrees.

Figure 73 and Figure 74 show the radiance and percent difference relationships at geometric depths z = 50 m for the 580 nm radiance field.

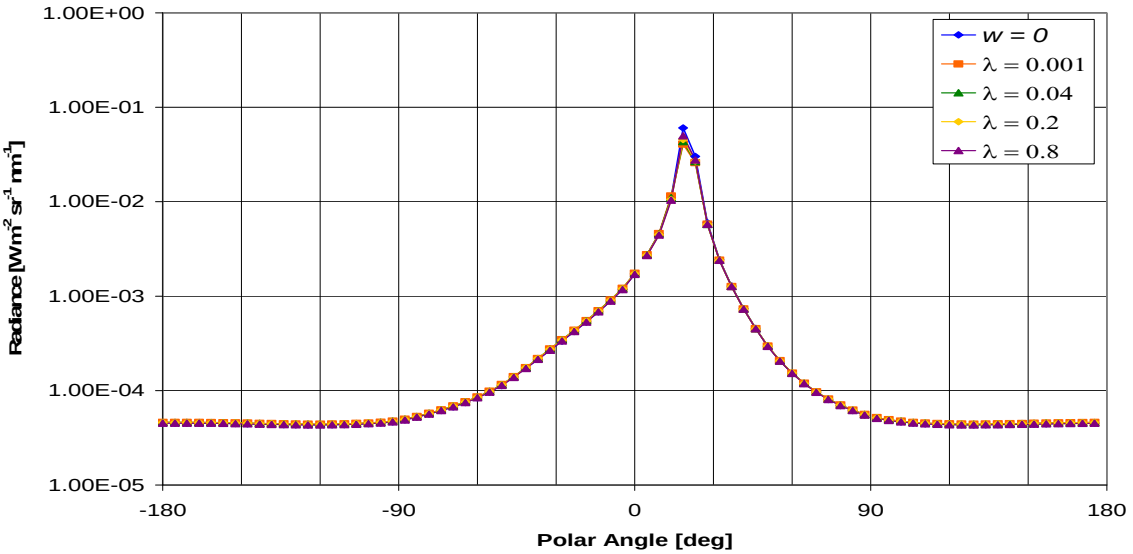

Figure 73 Logarithmic radiance versus polar angle for 580 nm light at multiple K_{max} values, geometric depth z =50 m. K_{max} values correspond to cut-off wavelengths 0.001, 0.04, 0.2, and 0.8 meters. Solar zenith angle 30 degrees. Wind speed, *w*, of 0 m/s is included as a comparison

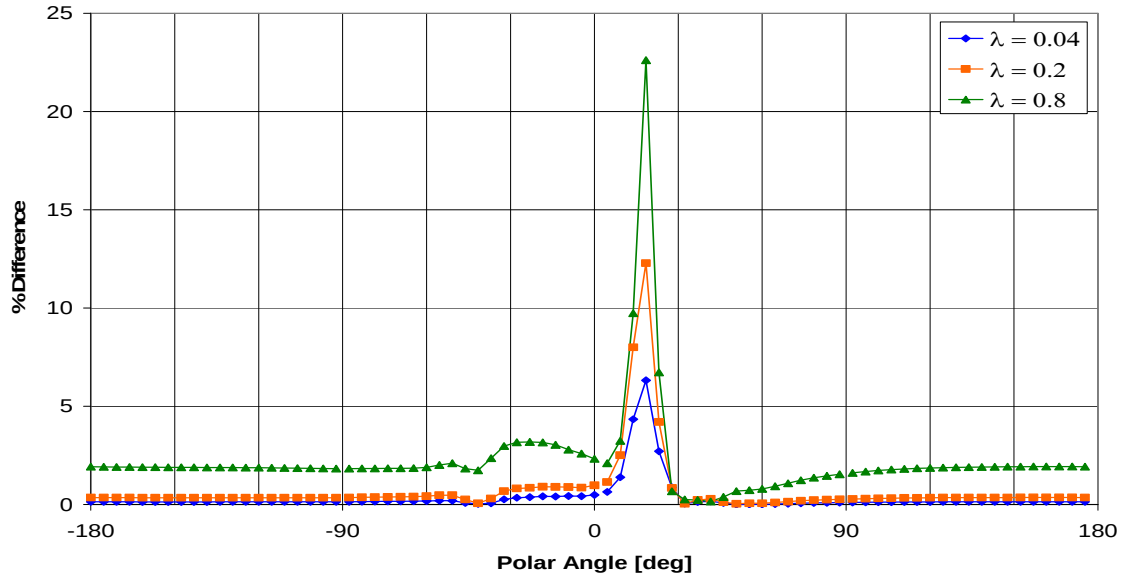

Figure 74 Percent difference versus polar angle for 580 nm light detectors at geometric depth z = 50 m. Percent difference is between longer cut-off wavelengths and the λ = 0.001 case. Solar zenith angle 30 degrees.

The trend observed with the previous two wavelengths holds true for the 580 nm radiance field as well. Near the surface, the peaks in percent difference lie in the solar beam and near the critical angle. As depth increases, the peaks in percent difference decrease until those near the critical angle are nearly eliminated.

Figure 75 and Figure 76 show the radiance and percent difference relationships at geometric depths z = 100 m for the 580 nm radiance field. Geometric depth z = 100 m is the beginning of the intermediate region.

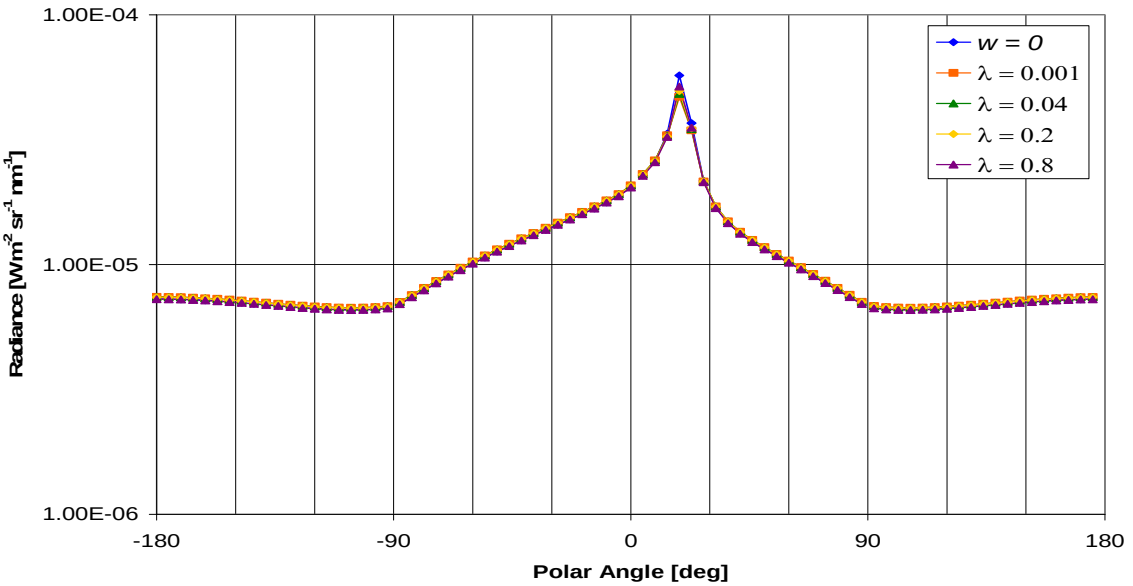

Figure 75 Logarithmic radiance versus polar angle for 580 nm light at multiple K_{max} values, geometric depth z = 100 m. K_{max} values correspond to cut-off wavelengths 0.001, 0.04, 0.2, and 0.8 meters. Solar zenith angle 30 degrees. Wind speed, *w*, of 0 m/s is included as a comparison

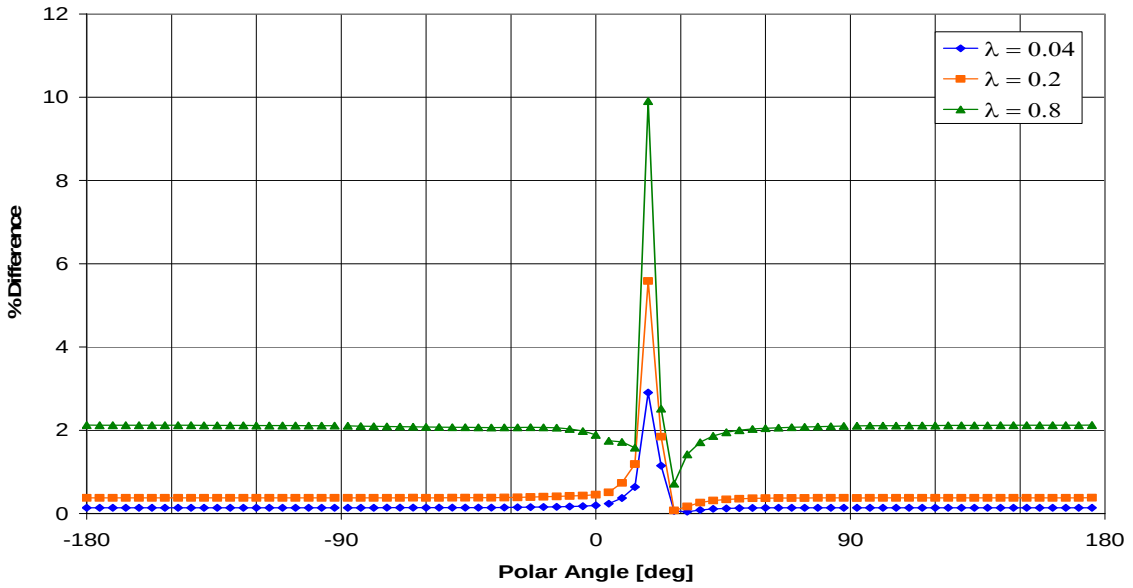

Figure 76 Percent difference versus polar angle for 580 nm light detectors at geometric depth z = 100 m. Percent difference is between longer cut-off wavelengths and the λ = 0.001 case. Solar zenith angle 30 degrees..

Figure 77 and Figure 78 show the radiance and percent difference relationships at geometric depths z = 300 m for the 580 nm radiance field.

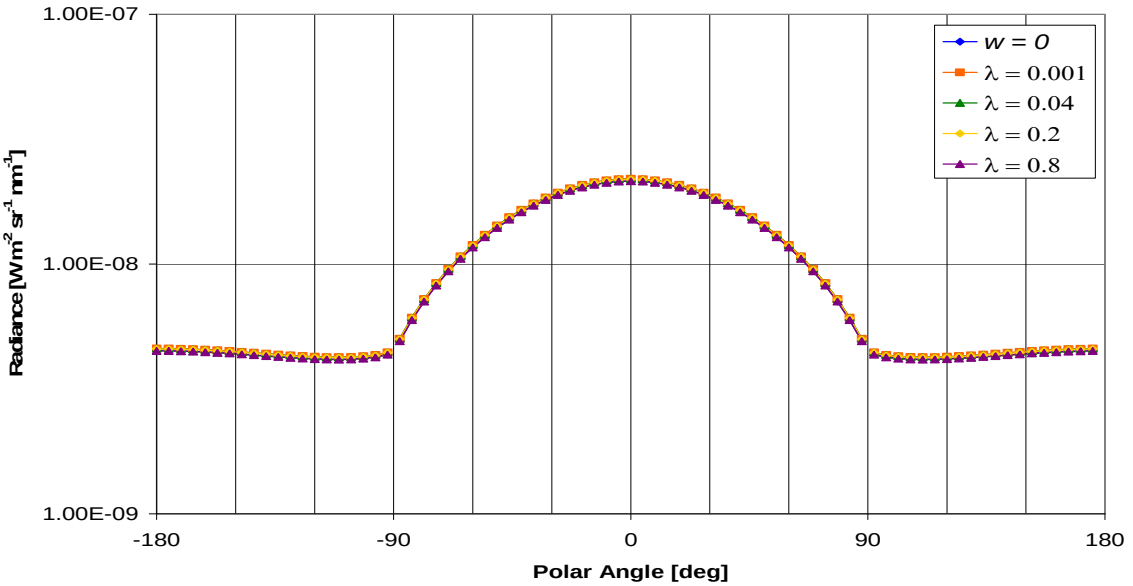

Figure 77 Logarithmic radiance versus polar angle for 580 nm light at multiple K_{max} values, geometric depth z = 300 m. K_{max} values correspond to cut-off wavelengths 0.001, 0.04, 0.2, and 0.8 meters. Solar zenith angle 30 degrees. Wind speed, *w*, of 0 m/s is included as a comparison

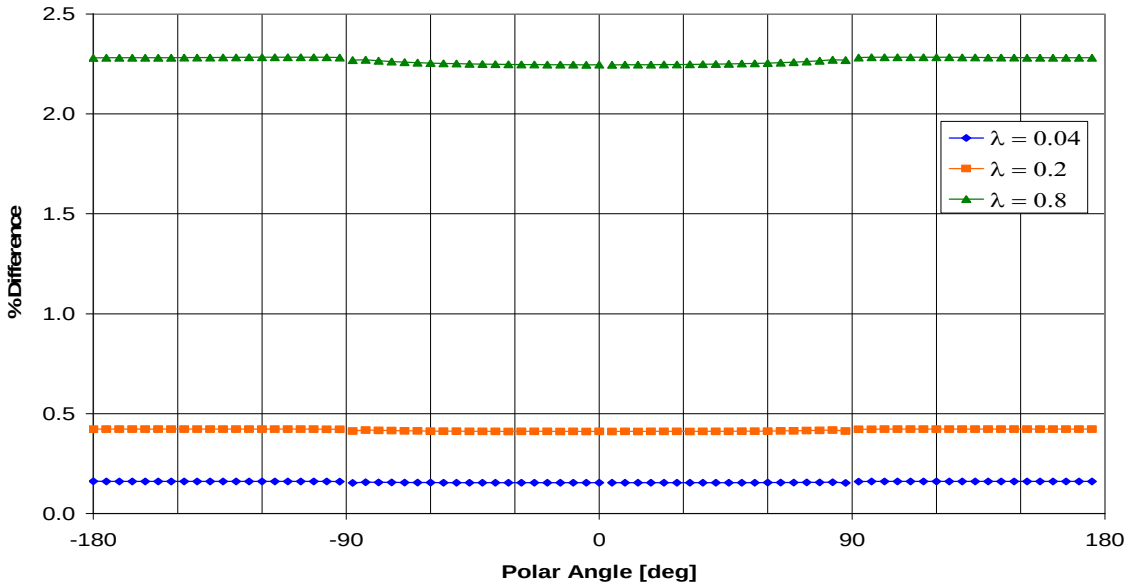

Figure 78 Percent difference versus polar angle for 580 nm light detectors at geometric depth z = 300 m. Percent difference is between longer cut-off wavelengths and the λ = 0.001 case. Solar zenith angle 30 degrees.

The trends seen in the 460 nm and 520 nm radiance fields continue to be seen in the 580 nm radiance field. In the intermediate region, the peaks in percent difference decrease gradually until the percent difference curves are nearly constant.

Figure 79 and Figure 80 show the radiance and percent difference relationships at geometric depths z = 500 m for the 580 nm radiance field. Geometric depth z = 500 m is the beginning of the asymptotic region.

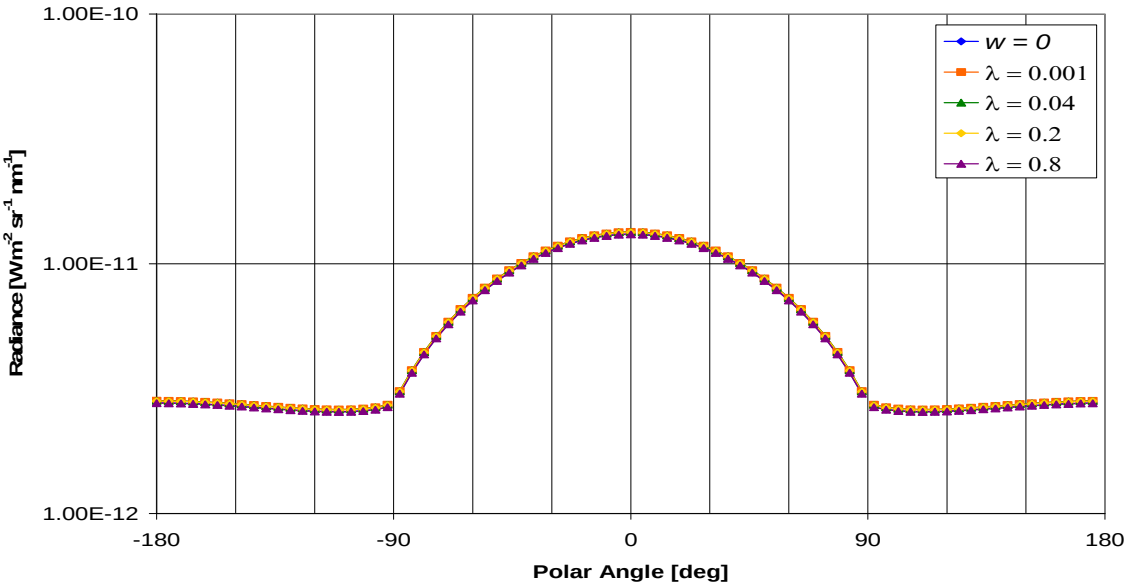

Figure 79 Logarithmic radiance versus polar angle for 580 nm light at multiple K_{max} values, geometric depth z = 500 m. K_{max} values correspond to cut-off wavelengths 0.001, 0.04, 0.2, and 0.8 meters. Solar zenith angle 30 degrees. Wind speed, *w*, of 0 m/s is included as a comparison

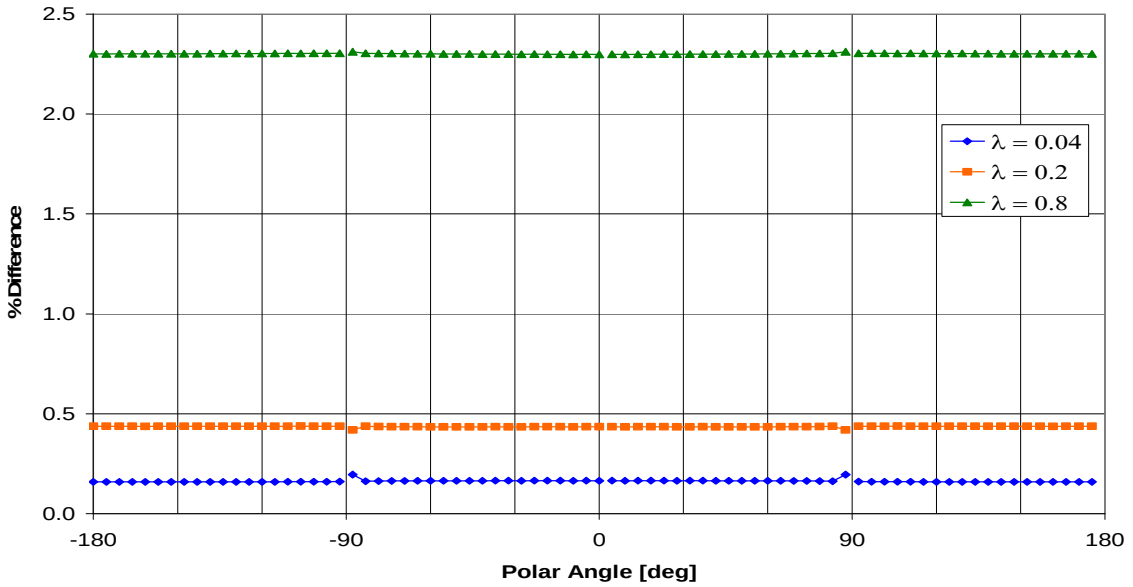

Figure 80 Percent difference versus polar angle for 580 nm light detectors at geometric depth z = 500 m. Percent difference is between longer cut-off wavelengths and the λ = 0.001 case. Solar zenith angle 30 degrees.

Figure 81 and Figure 82 show the radiance and percent difference relationships at geometric depths z = 700 m for the 580 nm radiance field.

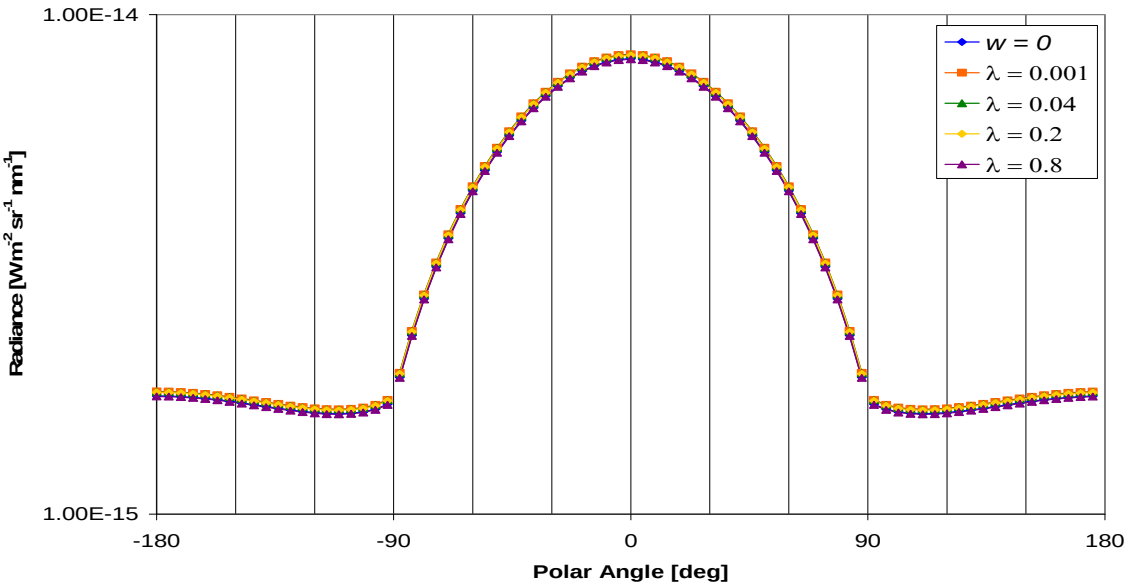

Figure 81 Logarithmic radiance versus polar angle for 580 nm light at multiple K_{max} values, geometric depth z = 700 m. K_{max} values correspond to cut-off wavelengths 0.001, 0.04, 0.2, and 0.8 meters. Solar zenith angle 30 degrees. Wind speed, *w*, of 0 m/s is included as a comparison

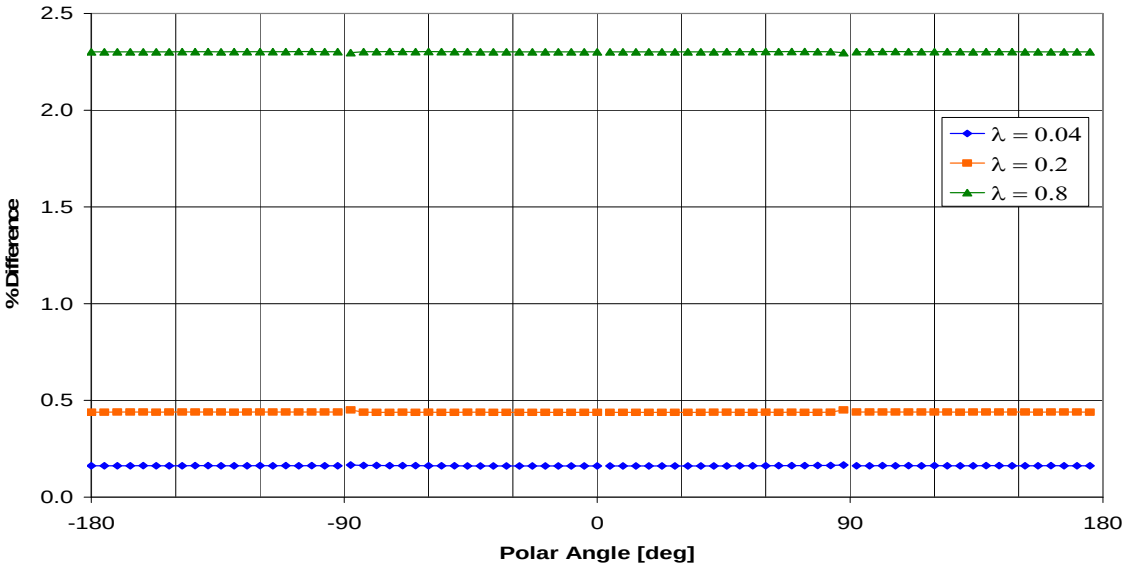

Figure 82 Percent difference versus polar angle for 580 nm light detectors at geometric depth z = 700 m. Percent difference is between longer cut-off wavelengths and the λ = 0.001 case. Solar zenith angle 30 degrees.

Again, as shown in the 460 nm and 520 nm cases, the effect of changing the mean square slope is greatest near the sea surface, in the solar beam and near the critical angle. The effect decreases with increasing depth, with the effect near the critical angle decreasing faster than the effect on the radiance field in the solar beam. Once the asymptotic region is reached, the effect of changing the mean square slope is constant for all polar angle values and remains constant with increasing depth.

5.4 Conclusions

The effect on the radiance field of changing the mean square slope is large at shallow depths, near the ocean surface. For all water models and wavelengths, there are three peaks in percent difference to the radiance for the ideal case mean square slope. These three peaks are in the direction of the solar beam and near the critical angle, around 48 degrees and -48 degrees. In every case, and at ever depth, the greatest percent difference to the ideal case came from the radiance field corresponding to the most truncated maximum wave number. In general, when a lower the maximum wave number is used to solve the mean square slope integral equation, a larger percent difference is seen between the ideal radiance field and that of the truncated integral.

The asymptotic region could not be reached with the one component water model, however, the effect of changing the mean square slope on the asymptotic radiance field for the Case 1 water model was determined. For all three representative wavelengths of the Case 1 model, for depths in the asymptotic region, the percent difference curves were constant for all polar angles. Even in the asymptotic region the radiance corresponding to a larger cutoff wavelength, or lower maximum wave number, had a greater percent difference to the ideal spectrum.

CHAPTER VI
CONCLUSIONS

This investigation had three major sections. The first task was to determine the effect of Raman scattering on the radiance field of multiple wavelengths of light in water. The second task was to find the location of the asymptotic region in each of the water models. Finally, the third and greatest task was to determine the effect of changing the mean square slope on the radiance field of each of the water models down through the asymptotic region.

It was found that Raman scattering has little or no effect on the radiance field for wavelengths less than 500 nm. This result agrees with what is expected. Solar incident light of wavelengths greater than 550 nm does not penetrate very deep into the ocean, so the radiance field for those wavelengths will be dominated by Raman scattering. At 500 nm, the effect of Raman scattering is only slight. However, this effect increases with increasing wavelength. Also, within a single wavelength, the effect of Raman scattering increases with increase in depth.

Second, it was found that a clear water column does not generate an asymptotic radiance field within a reasonable, measurable depth. Also, the location of the asymptotic region is not a constant for all wavelengths in a two component water model. Rather, the size and location of the asymptotic region varies from wavelength to wavelength. One surprising result is that a radiance field which is dominated by Raman scattered photons does not exhibit the characteristics of the radiance field from which those photons originated, particularly the location of the asymptotic region.

In the third investigation it was found that changing the mean square slope has a large effect on the radiance field near the surface, for all water models. This effect is greatest when the maximum wave number used in the mean square slope integral is smallest. In

general, the peaks in the percent difference between the radiance for the truncated mean square slope and that of the ideal case were found in the direction of the solar beam, and also near the critical angle, about 48 degrees and -48 degrees. The peaks near the critical angle decrease with increase in depth much faster than the peak in the solar beam. However, in the asymptotic region, the peaks disappear fully, and the percent difference curves are constant for all polar angle values. Even in the asymptotic region, the percent difference is greater for the radiance field corresponding to the most truncated mean square slope integral.

REFERENCES

1. R. B. Forward, Jr, K. W. Horch, and T. H. Waterman, "Visual orientation at the water sufreace by the teleost *zenarchopterus*," Biol. Bull., **143,** 112-126 (1972).

2. H. R. Gordon and X. Xu, "Marine asymptotic daylight field: effects of inelastic processes," Appl. Opt., **35**, 4194-4205 (1996).

3. C. D. Mobley and L. K. Sundman, *Hydrolight 4.1 users' guide*. (Sequoia Scientific, Inc., Redmond, WA, 2000).

4. R. C. Smith and K. S. Baker, "Optical properties of the clearest natural waters (200-800 nm)," Appl. Opt. **20**, 177-184 (1981).

5. C. D. Mobley, *Light and water: Radiative transfer in natural waters.* (Academic Press, San Diego, 1994)

6. B. R. Marshall and R. C. Smith, "Raman scattering and in-water ocean optical properties," Appl. Opt. **29**, 71-84 (1990).

7. R. M. Pope and E. S. Fry, "Absorption spectrum (380-700 nm) of pure water. II. Integrating cavity measurements," Appl. Opt. **36**, 8710-8723 (1997).

8. J. Berwald, D. Stramski, C. D. Mobley and D. A. Kiefer, "Effect of Raman scattering on the average cosine and diffuse attenuation coefficient of irradiance in the ocean," Limnol. Oceanogr. **43**, 564-576 (1998).

9. T. Elfouhaily, B. Chapron, K. Katsaros, and D. Vandemark, "A unified directional spectrum for long and short wind-driven waves," J. Geophys. Res. **102**, 15,781-15,796 (1997).

10. C. Cox and W. Munk, "Measurement of the roughness of the sea surface from photographs of the Sun's glitter," Journal of the Optical Society of America **44**, 838-850 (1954).

Additional Resources

J.T. Adams, E. Aas, N.K. Højerslev, B. Lundgren, "Comparison of radiance and polarization values observed in the Mediterranean Sea and simulated in a Monte Carlo model," Appl. Opt. **41**, 2724-2733 (2002).

S. Chandrasekhar, *Radiative transfer*. (Dover Publications Inc., New York, 1960)

G.W. Faris and R.A. Copeland, "Wavelength dependence of the Raman cross section for liquid water," Appl. Opt. **36**, 2686-2688 (1997).

W.W. Gregg and K.L. Carder, "A simple spectral solar irradiance model for cloudless maritime atmospheres," Limnol. Oceanogr., **35**, 1657-1675 (1990).

V.I. Haltrin and G.W. Kattawar, "Self-consistent solutions to the equation of transfer with elastic and inelastic scattering in oceanic optics: I. Model," Appl. Opt. **32**, 5356-5367 (1993).

G.W. Kattawar and X. Xu, "Filling in of Fraunhofer lines in the ocean by Raman scattering," Appl. Opt. **31**, 6491-6500 (1992).

B. Lungren and N.K. Højerslev, "Daylight measurements in the Sargasso Sea. Results from the 'Dana' expedition, January-April 1966," Kobernhavns Univ. Inst. For Fysisk Oceanografi – Report N. 14 (1971).

B.R. Marshall and R.C. Smith, "Raman scattering and in-water ocean optical properties," Appl. Opt. **29**, 71-84 (1990).

C.D. Mobley, et. al., "Comparison of numerical models for computing underwater light fields," Appl. Opt. **32**, 7484-7504 (1993).

T.J. Petzold, *Volume scattering functions for selected ocean waters*. (Scripps Institute of Oceanography, San Diego, 1973)

R.H. Stavn and A.D. Weidermann, "Optical modeling of clear ocean light fields: Raman scattering effects," Appl. Opt. **27**, 4002-4011 (1988).

T.H. Waterman, "Reviving a neglected celestial underwater polarization compass for aquatic animals," Biol. Rev., **81**, 111-115 (2006).

VITA

Name:	Julie Marie Slanker
Address:	4220 TAMU College Station, TX 77843-4220
Email Address:	jslanker@tamu.edu
Education:	B.S. Physics, Florida Institute of Technology, 2005
	B.S. Space Science: Astrophysics Option, Florida Institute of Technology, 2005
	M.S. Physics, Texas A&M University, 2007